ROLE OF COSOLUTES ON LYSOZYME DIFFUSIOPHORESIS AND CONDENSATION IN AQUEOUS MIXTURES

by

AISHA FAHIM

M.Sc. Chemistry, 2009
The Islamia University of Bahawalpur, Pakistan

M.Phil. Physical Chemistry, 2011
The Islamia University of Bahawalpur, Pakistan

Submitted to the Graduate Faculty of the
College of Science and Engineering
Texas Christian University
in partial fulfillment of the requirements
for the degree of

Doctor of Philosophy

December 2020

Acknowledgments

I am grateful to my advisor, Dr. Onofrio Annunziata, for his constant support and guidance throughout the years of my Ph.D. Your patience, invaluable guidance, insightful suggestions, constructive criticism, and encouragement to work independently helped me to grow and polish my abilities as a researcher. Thank you very much for helping me to improve my English and scientific writing abilities.

I am indebted to my committee members, Dr. Jeffery L. Coffer, Dr. Sergei V. Dzyuba, and Dr. Youngha Ryu for their guidance and help at each step of my Ph.D. I also extend my gratitude to Dr. Benjamin G. Janesko for his help and support in the official matters. Many thanks to Dr. Viviana Costa for her indispensable help and for answering the many, many questions regarding the use of instruments. Thank you, Page Kimbrell, for your help in administrative matters. I am truly grateful to Gerry Katchinska for his help and availability to fix the instruments in my lab.

I want to say thank you to my lab mates Lara and Eli for their support and the great moments that we shared in the lab. I would also like to say thank you to my friends Marlius, Vishal, Akop, Nguyen, and Andrea. A big thank you to my friend Dr. Stephani Jones for being always available during my Ph.D. I am extremely grateful for my family, my mother, my brothers, sister, and my husband who supported me throughout this journey.

Finally, I am thankful to the TCU College of Science and Engineering and the Department of Chemistry & Biochemistry for the generous funding and support.

I dedicate this dissertation to my late father who always believed in me and encouraged me to pursue my dreams, but couldn't wait to see me as a doctor.

Contents

List of Figures

List of Tables

Chapter 1

Introduction

1.1 Motivation

With the advent of recombinant-DNA techniques,[1, 2] the number of available proteins and their applications as drugs (*e.g.* antibodies, insulin),[3] biocatalysts[4] and biomaterials[5] have significantly increased. Understanding thermodynamic, phase separation and transport properties of protein aqueous solutions is important for developing high-throughput methods for the purification and characterization of these biomacromolecules and their successful employment in pharmaceutical and biotechnological applications.[6, 7] This dissertation investigates two distinct aspects of proteins in aqueous mixtures, namely protein diffusiophoresis and protein condensation. Hen egg-white lysozyme is employed not only because it is regarded as a model protein for biophysical-chemistry studies but also for its employment in protein-based materials.[8-10] This protein is available at high purity as well as being one of the best characterized proteins.[11, 12] Lysozyme diffusiophoresis is introduced in section 1.1.1 while lysozyme condensation is introduced in section 1.1.2. In the remaining sections of this chapter, lysozyme and its properties in solution with emphasis to acid-base properties are reviewed.

1.1.1 Salt-induced Protein Diffusiophoresis

Proteins in aqueous mixtures are subject to a broad range of mass-transfer processes such as centrifugation,[13] dialysis,[14] crystallization,[15] adsorption onto surfaces,[16] mixing in microfluidics,[17]

controlled release,[18, 19] transport inside living systems,[20] enzymatic kinetics,[21] and pattern formation[21, 22]. Since these processes occur in the presence of concentration gradients, diffusion coefficients are important for modeling, predicting, and designing related applications.[23-28] Diffusion represents the net transport of solute molecules from a region of high concentration to the region of low concentration induced by the concentration gradient of a solute within a liquid mixture without the application of any outside force.[29] It is one of the most fundamental transport phenomena in chemistry and material sciences.[30, 31] The flux of solute particles onset by the concentration gradient is characterized by the diffusion coefficient which represents the mean-squared displacement of a particle in the given time through a medium.[27, 28] Diffusion coefficient provides the quantitative measurements of the rate at which a diffusion process occurs.[32]

Since proteins are charged,[33] salts are ubiquitously employed as a supporting electrolyte.[6, 34, 35] By varying solution ionic strength, salts can modulate protein-protein interactions, protein conformational stability and related biological functions. Recently, it has been shown that a diffusive transport process, distinct from protein Brownian diffusion, emerges in the presence of salt concentration gradients.[36] Specifically, a salt concentration gradients can induce protein migration in aqueous mixtures. This transport process is classified as *Diffusiophoresis*.[29] From a theoretical point of view, the migration of colloidal particles or macromolecules such as proteins is induced by a gradient of the *chemical potential* of cosolutes such as salts. The phenomenon of diffusiophoresis can be compared to the another well-known transport phenomenon termed as electrophoresis which describes the net transport of macromolecules induced by a gradient of electrical potential.[37] Salt-induced diffusiophoresis of charged particles at relatively low salt concentration has been successfully described by electrokinetic models similar to those applied in the field of electrophoresis.[29, 38, 39] This association with electrophoresis originates from the fact that a salt concentration gradient in diffusiophoresis creates an internal electric field directly

proportional to the difference in mobility between salt counterion and coion.[36] Therefore, we hypothesize that changing the salt type will significantly impact the diffusiophoresis of protein. For proteins, their aqueous mixtures consist of buffers, added salts or other macromolecules, hence are invariably multicomponent in nature.[29]

Diffusiophoresis has been previously investigated for multicomponent systems of relatively large colloidal particles flowing inside microfluidic devices. These studies revealed strong coupling effects and indicated that salt concentration gradients with tunable amplitude and direction may be used to boost particle migration as associated phenomena such as mixing, spreading and adsorption, *etc*.[40] [29] Another recent study of neutral polyethylene glycol (PEG) diffusiophoresis was carried out with the goal of a better understanding of the effects of salting-out strength and diffusiophoresis.[41] This study showed that gradients of strong salting-out agents such as Na_2SO_4 can produce large enhancements and depletions of PEG concentration which can be exploited to promote the condensation of macromolecules near interfaces. Hence, this transport mechanism can be examined for proteins in order to develop new methods in which salt concentration gradients lead to protein separation, self-assembly, and adsorption-based biosensing.[40-48]

In the first part of this dissertation, we examine lysozyme diffusiophoresis in the presence of three salts: NaCl, KCl, and $MgCl_2$ at pH 4.5 and 25 °C. These three salt cases are especially interesting for understanding how changing the magnitude of the internal electric field produced by the salt gradient affects protein diffusiophoresis. These salts are selected based on the difference in the ionic mobilities of their constituent ions. In the KCl case, the two ions have similar mobilities[49, 50] and the electrophoretic mechanism is expected to be small compared to other mechanisms contributing to diffusiophoresis such as macromolecule preferential hydration. In the

NaCl case, the electrophoretic mechanism is significantly more important, while the contribution of other mechanisms to diffusiophoresis is expected to be practically the same as in the KCl case. Finally, the main goal of our study is the examination of protein diffusiophoresis in the presence of $MgCl_2$. This salt is expected to be relatively more complex due to the divalent nature of salt[51] and Mg^{2+} interactions with proteins.[52, 53] This case is also predicted to be more appealing for potential diffusiophoresis applications due to the large difference in mobilities[50, 54] between Cl^- and Mg^{2+} and an intensified thermodynamic driving force caused by strong thermodynamic nonideality.[54-56]

In the first part of this dissertation, we first show the experimental behavior of lysozyme diffusiophoresis coefficients as a function of salt concentrations at 25 °C and pH 4.5 for NaCl, KCl, and $MgCl_2$. These transport data allowed us to identify lysozyme diffusiophoresis is the largest in the presence of $MgCl_2$. We then theoretically described a diffusion-based transport process in which lysozyme was subjected to a concentration gradient of the $MgCl_2$ and assessed the magnitude of diffusiophoresis. In the final step, we examined the role of protein charge on its diffusiophoresis. Through the characterization of hydrogen-ion titrations, the effects of $MgCl_2$ on lysozyme charge were compared to those of NaCl and KCl. Experimental procedures and instrumentation used for all of these studies are described in Chapter 3 of this dissertation while Chapter 4 to Chapter 6 provides the results of this investigation.

1.1.2 Protein Condensation in Aqueous Solutions

Physical stability and aggregation properties of proteins in aqueous solutions are crucial for understanding cell compartmentalization,[57, 58] protein-aggregation diseases,[59, 60] protein-based drug formulations,[61, 62] enzyme-based materials,[63] and characterizing protein structure and function from high-quality protein crystals.[64, 65]

Liquid-liquid phase separation (LLPS) represents the reversible formation of two separate coexisting liquid phases of an initially homogeneous solutions of macromolecules (proteins, polymers) or colloidal particles (e.g. polymer nanoparticles), onset by the change in conditions such as temperature, solvent, ionic strength and pH etc. The separated liquid phases consist of a macromolecular-rich and macromolecular-depleted layer. It is known[66] that aqueous solutions of proteins may undergo reversible LLPS under a well-defined temperature called LLPS temperature, T_{ph}. One interesting feature of LLPS is the formation of oil-like protein-rich nano- and micro-droplets. Since the average distance between protein molecules inside the droplets is small, protein-rich droplets can be regarded as reversible aggregates or condensates. Correspondingly, the formation of protein-rich droplets is denoted as *protein condensation*. Protein condensates have been observed and/or implicated in several biological processes and related pathologies.[67, 68] For example, several membraneless cytoplasmic compartments such as promyelocytic leukaemia bodies, stress granules, germ granules, P-bodies, Cajal bodies and paraspeckles have been observed to behave as semifluid spheres.[67-70] Many of these compartments are fundamental for concentrating certain molecules and facilitating spatiotemporal regulation of cellular functions[71, 72] such as signaling complexes, synaptic transmission, the cytoskeleton, DNA compaction, and are also implicated in several types of cancer and neurodegenerative diseases.[68, 72-74] LLPS of protein solutions is important for the following reasons. First, protein-rich droplets are known to be metastable intermediates for other processes. Specifically, LLPS is a metastable phase transition and protein-rich droplets may be an intermediate state toward the formation of protein crystals or the formation of irreversible protein aggregates supported by naturally or artificially occurring chemical crosslinking.[64, 65, 75] This is important for the obtainment of protein crystals for crystallographic studies and understanding protein-aggregation diseases such as cataracts, sickle cell anemia and Alzheimer's disease.[57, 59] In addition, the protein-rich droplets are highly viscous

and have gel-like characteristics and the addition of chemical crosslinkers in these droplet containing mixtures results the formation of covalent bonds between macromolecules. This technology can be opted for the production of protein-based materials such as crosslinked enzyme aggregates.[63] Second, measurements of LLPS temperature, T_{ph}, provide a criterion to characterize the thermodynamic stability of protein formulations (e.g. antibodies).[61] Third, it has been hypothesized that the formation of protein-rich droplets provides the driving force for the formation of micro-compartments inside living cells.[57, 58]

There have been several thermodynamic studies on LLPS involving proteins, nanoparticles and materials like dendrimers. However, the related kinetic studies characterizing the LLPS rate remain relatively scarce. In relation to the kinetic mechanism, it is not clear how the fate of protein-rich droplets and related mesoscopic clusters depends on the composition of the surrounding fluid. In the second part of this dissertation, we explored how the fate of lysozyme-rich droplets is affected by the chemical nature of additives. Our results show that it is possible to introduce two additives, one to drive the formation of protein-rich droplets, and a second additive to change their kinetic evolution into another protein-rich phase.

We specifically show that insertion of 2-[4-(2-hydroxyethyl)piperazin-1-yl]ethanesulfonic acid (HEPES) in lysozyme-NaCl-water system triggers the formation of protein micro-particles from protein-rich droplets. The temperature-concentration phase diagram of this system was characterized to assess the thermodynamic stability of macroparticles compared to LLPS and observed rod-shaped crystals. The morphologies and sizes of microparticles were analyzed using light microscopy. Molecular interactions were further characterized by using dynamic light scattering, HEPES depletion in the supernatant, and isothermal titration calorimetry. The experimental procedures adopted for these studies are provided in Chapter 8, while Chapter 9

details the findings of these studies. To explore the chemical basis responsible for the complex LLPS of lysozyme-HEPES system, these studies were extended to include other commercially available additives that structurally resemble HEPES. The results of these studies are provided in the last chapter of this dissertation.

1.2 Acid-Base Chemistry of Proteins

The study of acid-base properties of proteins is fundamental to understand their mass transport in aqueous solutions, mainly because these properties control the protein protonation state and ultimately protein charge. Furthermore, the interactions of proteins with ions and small molecules are influenced by the net charge on protein in aqueous solutions imparted by the protonation-deprotonation of prototropic groups in protein.[76] These prototropic groups include only the side chains of the amino acids which are solvent accessible and ionizable with pH (except for the N- and C- termini of the chain) and does not include those amino acids which form the peptide bond and are the part of polypeptide chain. Among these groups, negative charges are imparted by the conjugate bases of carboxylic, phenolic, and thiol groups and positive charges by the protonated secondary amines. If protein interactions with small ions can be neglected, the average net charge, Z_P, on protein is the sum of positively and negatively prototropic groups and is the function of solution pH. The pH at which the protein has zero net charge is called the isoelectric point. The protonation-deprotonation of amino acids and the interaction of protein with ions and small molecules can be described by following generalized multiple equilibria model.

Given a protein P containing *n* prototropic groups, the stepwise addition of proton H^+ can be given as:[77]

$$\begin{aligned} P + H &\overset{K_1}{\rightleftharpoons} PH \\ PH + H &\overset{K_2}{\rightleftharpoons} PH_2 \\ PH_{n-1} + H &\overset{K_n}{\rightleftharpoons} PH_n \end{aligned}$$

The charge sign "+" on proton is omitted for clarity. For the generic step *i*, the corresponding equilibrium-constant can be expressed as:

$$K_i^{-1} = \frac{[PH_i]}{[PH_{i-1}][H]} \tag{1.1}$$

where K_i is the stepwise dissociation constant and the quantities $[PH_i]$, $[PH_{i-1}]$ and [H] refer to molar concentration of protein species and proton respectively. The cumulative association constant, β_i, can be introduced by considering the following generic reaction:

$$P + iH \rightleftharpoons PHi$$

The related law of mass-action is:

$$\beta_i = \frac{[PH_i]}{[P][H]^i} \tag{1.2}$$

where $\beta_i = \prod_{j=1}^{i} K_j^{-1}$. The average number of protons bound per protein is given by:

$$n_H = \frac{[PH_1] + 2[PH_2] + \cdots + n[PH_n]}{[P] + [PH_1] + [PH_2] + \cdots + [PH_n]} \tag{1.3}$$

Applying Eq. 1.2 systematically:

$$\mathrm{n_H} = \frac{\beta_1[\mathrm{H}] + 2\beta_2[\mathrm{H}]^2 + \cdots + n\beta_n[\mathrm{H}]^n}{1 + \beta_1[\mathrm{H}] + \beta_2[\mathrm{H}]^2 + \cdots + \beta_n[\mathrm{H}]^n} = \frac{\sum_{i=1}^{n} i\beta_i[\mathrm{H}]^i}{1 + \sum_{i=1}^{n} \beta_i[\mathrm{H}]^i} \tag{1.4}$$

We now consider a hypothetical limiting case is in which all protonation sites are assumed to have same affinity for the proton (equivalent sites) and the affinity of any site is independent of other sites (independent sites). In other words, it is assumed that all binding sites have same acid constant, K_a, independent of the protonation state of protein. In this case, β_i, can be written as:

$$\beta_i = \frac{n!}{(n-i)!i!} K_a^{-i} \tag{1.5}$$

Where the binomial coefficient, $n!/(n-i)!i!$, takes into account all the combinations that can generate [PH_i]. For instance, a hypothetical protein with 4 total number of sites (n = 4) will have $4!/(4-2)!2! = 6$ [PH_2] species. Combining Eq. 1.4 and Eq. 1.5:

$$\mathrm{n_H} = \frac{\sum_{i=1}^{n} i \frac{n!}{(n-i)!i!} \left([\mathrm{H}]/K_a\right)^i}{1 + \sum_{i=1}^{n} \frac{n!}{(n-i)!i!} \left([\mathrm{H}]/K_a\right)^i} \tag{1.6}$$

Eq. 1.6 can be simplified using the binomial theorem, $(1+x)^n = \sum_{i=0}^{n} \frac{n!}{(n-i)!i!} x^i$, as:

$$\begin{aligned} \mathrm{n_H} &= \frac{n\left([\mathrm{H}]/K_a\right) \sum_{i-1=0}^{n} \frac{(n-1)!}{(n-i)!(i-1)!} \left([\mathrm{H}]/K_a\right)^{i-1}}{\sum_{i=0}^{n} \frac{n!}{(n-i)!i!} \left([\mathrm{H}]/K_a\right)^i} \\ &= \frac{n[\mathrm{H}]\left(K_a + [\mathrm{H}]\right)^{n-1}/K_a^n}{\left(K_a + [\mathrm{H}]\right)^n/K_a^n} = \frac{n[\mathrm{H}]}{K_a + [\mathrm{H}]} \end{aligned} \tag{1.7}$$

It is important to remark that the hypothetical model used to derive Eq. 1.7 have several limitations. Firstly, for a real protein molecule, all the protonation sites are not equivalent (*i.e.,* the sites are not identical) and each amino acid have different intrinsic acid dissociation constant. Secondly, due to the assumption of independent sites, this model does not take into account the electrostatic interactions between prototropic groups on protein imparted by the steric interferences, charges enhanced by the bound ions and conformational changes induced by the interactions with protons or other ions. However, this model is important as it shows that the protonation state of a protein is the function of solution pH. Specifically, Eq. 1.7 shows that the protonation state of protein increases with a decrease in pH which correspondingly leads to the increase of the protein net charge, Z_P. For example, if a protein is negatively charged at higher pH, it may become positively charged at lower pH after passing through the isoelectric point (pH value corresponding to $Z_P = 0$) at any intermediate pH.

1.3 Lysozyme

Hen egg-white lysozyme (HEWL) is a single-polypeptide chain protein containing 129 amino acids. It is found in all major taxa of living organisms and is part of their innate immune system.[78] Lysozyme damages the bacterial cell walls by catalyzing the hydrolysis of 1,4-β-linkages between N-acetylmuramic acid and N-acetyl-D-glucosamine residues in peptidoglycan, and between N-acetyl-D-glucosamine residues in chitodextrins.[79] It is efficient in lysing the cell walls of both bacteria and fungi which are critical for their resistance to osmotic stress.[80] This protein is employed in protein engineering techniques to determine the mode of substrate binding, mechanism of catalysis and folding behavior of enzymes.[81-83] As previously mentioned, lysozyme is also an important model protein in physiochemical studies including those on thermodynamic

and transport properties.[66, 84-88] The thermodynamic background on LLPS of lysozyme aqueous mixtures will be discussed in Chapter 7.

Recently, theranostic applications of lysozyme in protein-based materials have emerged due to the antimicrobial properties of this protein.[8, 10, 89-91] It has been used in biomineralization to make various nanoparticles including Au, Ag, Pt, Fe, Ti, and Cu.[10, 92] These various applications of lysozyme are not only related to its role as a stabilizing agent but also to its role as a template or capping agent to prepare these materials.[10] Lysozyme based nanoparticles have several applications including anti-microbial, drug delivery, wound healing, and catalytic activity, *etc*.[10] Lysozyme-based silver nanoparticles inhibit DNA replication, inactivate cellular protein in bacteria, and introduce the structural changes in the bacterial cell membrane.[93] Moreover, drug-coated nanoparticles have been used as drug carriers in relation to diseases such as glaucoma.[92] Finally, lysozyme-based nanogels have been used for imaging applications and to deliver the antitumor agent doxorubicin and psychoactive drugs, obromine and theophylline.[10, 94]

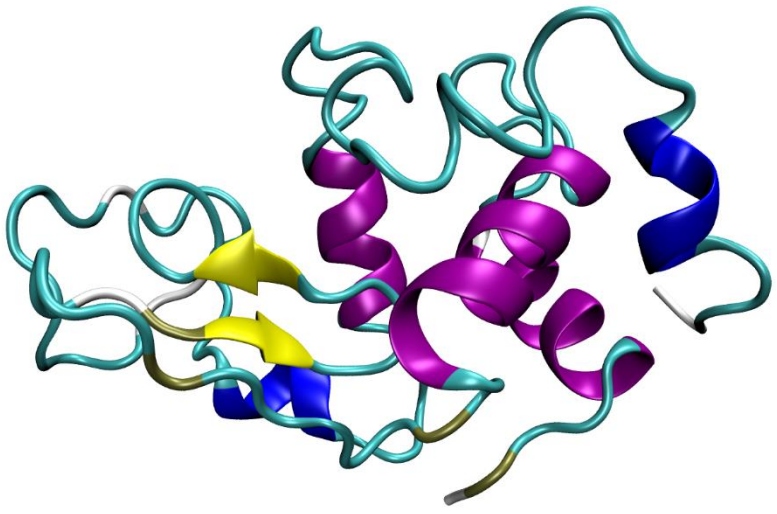

Figure 1.1 Tertiary structure of hen egg-white lysozyme protein determined by high resolution (0.65Å) diffraction data using synchrotron radiations at 100K temperature. Structure is obtained from protein databank (PDB ID: 2VB1) and ribbons are colored according to secondary structure.

Lysozyme has an approximate shape of prolate ellipsoid with size of 4.5 × 3.0 × 3.0 nm (without bound water).[95] In comparison to proteins like myoglobin and hemoglobin, lysozyme has fairly small proportion of helix and reasonably long stretches of chain with irregular conformation. Several parts of these chain have extended conformation which closely resembles to the β sheets in fibrous proteins. The lysozyme molecule has a deep cleft on one side which divides the molecule roughly into two lobes. The first consists of the two ends of the chain (residues 1-39 and 85- 129), while the second (residues 40-84) is like a sheet and consists of residues either in the outer surface or lining the cleft. Most of the hydrophobic amino acids side chains are located inside molecule but exposed solvent-accessible surface area of lysozyme also contains some of hydrophobic residues. These residues include Val-2, Phe-3, Leu-17, Phe-34, Leu-75, Trp-123, Pro-70, Pro-79, Trp-62, Trp-63, Ile-98, Trp-108, and Val-109. The substantial proportions of the exposed solvent-accessible surface are constituted by the polar groups. However, Asp-66, Asp-52, Tyr-53, His-15, and Glu-35 are the least-exposed prototropic groups in the molecule. Lysozyme is thermally stable with a melting point of 72 °C at pH 5.0.[96] Its molecular weight is 14,307g.mol^{-1} and isoelectric point is 11.35.[97] Figure 1.1 shows the ternary structure of lysozyme obtained from using high resolution (0.65Å) synchrotron diffraction data at 100K of temperature (PDB ID: 2VB1).[98] The description of secondary structure and amino acids sequence are given in Fig. 1.2. The structure contains four disulfide bridges (Cys6–Cys127, Cys30–Cys115, Cys64–Cys80, Cys76–Cys94), shown using dotted lines in Fig. 1.2, that crosslink the polypeptide and stabilize its natural conformation. These disulfide bridges are not only essential in making lysozyme a globular protein but also stabilizes the molecule against reversible thermal unfolding.[99] The first two pairs of these

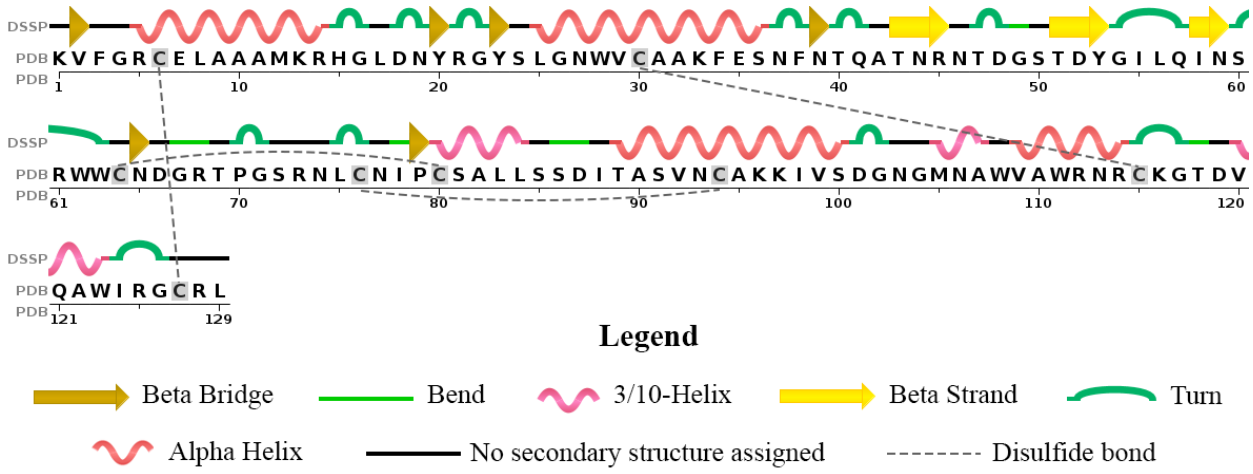

Figure 1.2 Secondary structure of hen egg-white lysozyme protein drawn using DSSP style of display along with amino acids sequence.

bridges have negative torsion angles while last two pairs have positive angles. All angles are in the range of 100° ± 10°.[95]

Sequence analysis using DSSP method[100] shows that the polypeptide chain consists of 40% helical (7 helices; 52 residues) and 10% beta sheet (9 strands; 14 residues). The HEWL has 32 ionizable/prototropic groups including the N-terminal α-amino and C-terminal α-carboxyl groups. The hydrogen ion titrations curves of lysozyme have been studied[101-103] and most of the state-of-the-art physiochemical models developed to quantify the inter- and intra- molecular electrostatic interactions between macromolecules and electrolytes are based on these titration curves.[104-107] It is based on the fact that the native conformation of lysozyme is more stable toward pH changes at room temperature than that of most other proteins, so that the entire titration curve can be taken to be that of the protein in a single conformation. This conformational stability also ensures that the locations of titratable groups on the native molecule in solution are the same as in the crystalline state. Table 1.1 lists the intrinsic p*K*a values of titratable groups in lysozyme calculated using the electrostatic model and adopted from Table 1 of Ref. [[101]]. Among these listed groups, the basic

Table 1.1 Experimental p*K*a values[101] for titratable groups in Hen egg-white lysozyme

Residue	**Type**	**p*K*a**	**Residue**	**Type**	**p*K*a**
N-term (Lys)	Basic	7.9	Lys-116	Basic	10.4
Lys-1	Basic	10.8	Arg-125	Basic	12.8
Arg-5	Basic	12.8	Arg-128	Basic	12.8
Lys-13	Basic	10.5	Glu-7	Acidic	2.6
Arg-14	Basic	12.8	Asp-18	Acidic	2.0
His-15	Basic	5.8	Tyr-20	Acidic	10.3
Arg-21	Basic	12.8	Tyr-23	Acidic	9.8
Lys-33	Basic	10.6	Glu-35	Acidic	6.1
Arg-45	Basic	12.8	Asp-48	Acidic	4.3
Arg-60	Basic	12.8	Asp-52	Acidic	3.4
Arg-68	Basic	12.8	Tyr-53	Acidic	12.1
Arg-73	Basic	12.8	Asp-66	Acidic	1.6
Lys-96	Basic	10.8	Asp-87	Acidic	2.1
Lys-97	Basic	10.3	Asp-101	Acidic	4.5
Arg-112	Basic	12.8	Asp-119	Acidic	2.5
Arg-114	Basic	12.8	C-term (Leu)	Acidic	3.1

amino acids are positively charged for a pH lower than their p*K*a and are neutral for the pH values higher than their p*K*a. Similarly, the acidic amino acids are neutral for the pH lower than their p*K*a or correspondingly are negatively charged if pH is higher than their p*K*a. These intrinsic p*K*a values, allow to estimate the protonation state and corresponding charge on lysozyme at a given pH if half contribution are considered from those groups which have p*K*a values equal to the given pH. For instance, at pH 4.5, the groups Lys-1, 13, 33, 96, 97, 116; Arg-5, 14, 21, 45, 60, 68, 73, 112, 114, 125, 128; Hys-15 and terminal $-NH_3^+$ group of Lys-1 are protonated and contribute a positive charge of 19. The groups, Glu-7, Asp-18, 52, 65, 87, 119 and the terminal $-COO^-$ group of Leu-129 are deprotonated and contribute a negative charge of 7. Each of the groups, Asp-48

and Asp-101 provide half contribution to the negative charge due to their p*K*a being in the vicinity of given pH of 4.5. All of these groups in combine impart a net charge of +11 to lysozyme at pH 4.5. Similarly, at pH 7.4, His-15 is neutral therefore the positive charge contribution from positively charged groups is reduced to 18. However, at this pH, Asp-48 and Asp-101 are fully deprotonated and Glu-35 is also deprotonated. Therefore, negative charge contribution from negatively charged groups will be enhanced to 10. Hence at pH 7.4, the net charge on lysozyme will be +8. In the context of understanding the effects of salts concentrations and type, our experimental determination of charges on lysozyme at pH range between 4.5 and 7.4 in the presence of salts are discussed in Chapter 3.

1.4 Buffers

LLPS studies of proteins involve high protein concentrations and the process of condensation may potentially occur with large variations in acid-base chemistry of proteins. Therefore, phase separation studies are carried out at a constant pH to ensure the thermodynamic and conformational stability of proteins in solution. The pH of protein solution for the phase separation studies can be adjusted by the addition of a proper biological buffer. A buffer is an aqueous solution consisting of a mixture of a weak acid and its conjugate base or a weak base and its conjugate acid. By convention, the acid-base properties of buffers are described using their p*K*a values which are the negative logarithmic of their acid constants. When pH is near the p*K*a of the buffer, changes in the number of protons or OH^- ions do not significantly alter the pH of solution. The ability of a buffer to maintain the pH is maximal at the p*K*a of the buffer and commonly adopted working range of a buffer is within one pH unit of the p*K*a value. The quantitative measure of the resistance of a buffer solution to pH change on addition of hydroxide ion is termed as buffer capacity. It can be defined as a positive quantity by employing any of the two equivalent expressions:

(A)

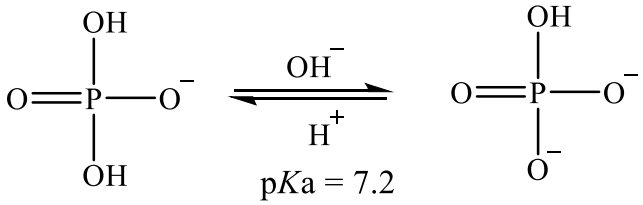

(B)

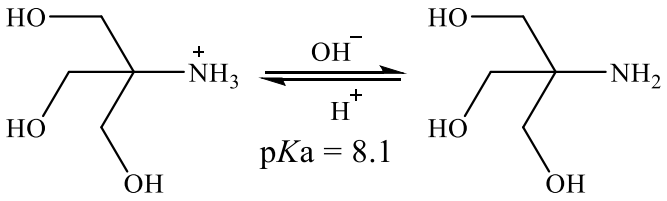

(C)

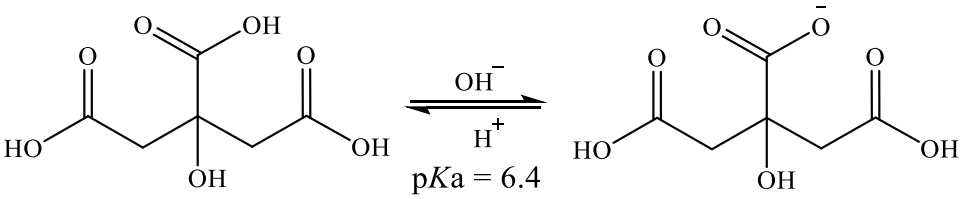

Figure 1.3 Acidic-basic forms of common buffer components (A) Phosphate (B) Tris, and (C) Citrate.

$$\text{Buffer Capacity} = \frac{dC_{\text{NaOH}}}{d\text{pH}} = -\frac{dC_{\text{HCl}}}{d\text{pH}} \tag{1.8}$$

In addition to the p*K*a the choice of buffer for a particular biological system also depends on its chemical characteristics. An ideal buffer should be chemically inert to the protein and should not affect the biochemical processes in which the underlying protein is involved.[108-110]

There are several common buffers used in biochemical studies such as phosphate, tris and citrate etc. (Fig. 1.3).These buffers are sometimes associated with certain limitations for their use in biological samples.[76] These limitations include inhibition for certain enzymes (e.g. inhibition of aminopeptidases, aminotransferases and cholinesterases by Tris buffer)[111-113], precipitation of certain polyvalent cations (e.g. phosphate buffer binds to Ca^{2+} and tris reacts with Cu^{2+} and Ca^{2+})[114]

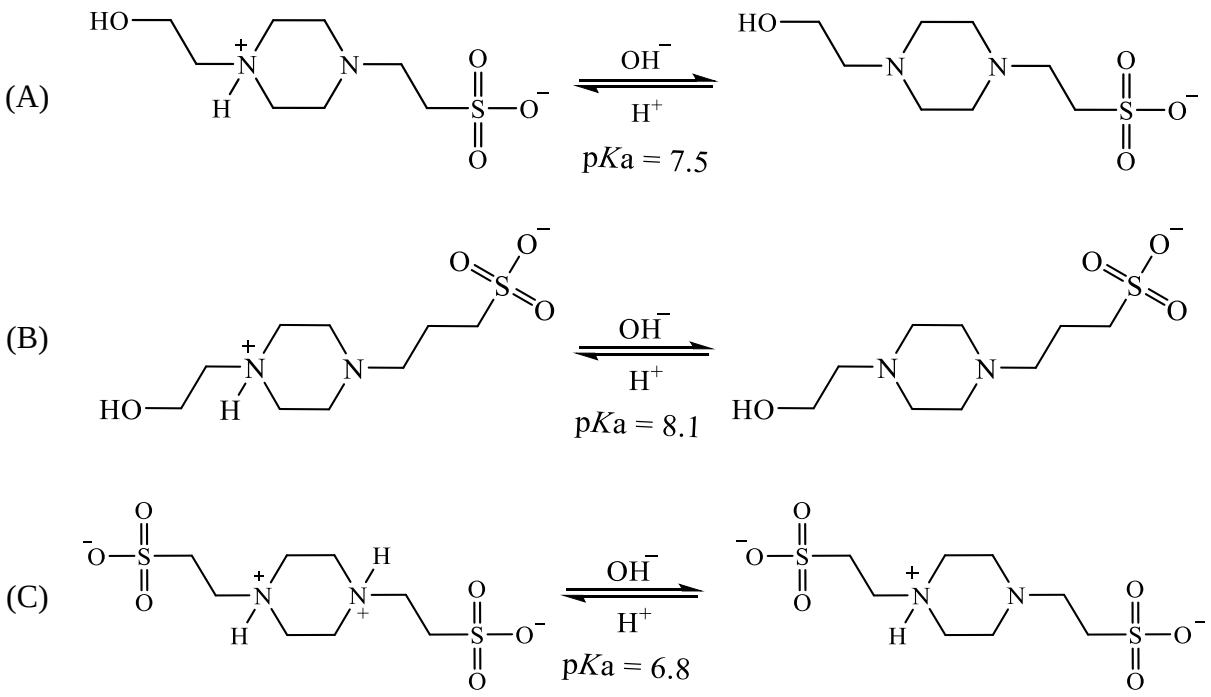

Figure 1.4 Acidic-basic forms of Good's buffers species used in this dissertation (A) HEPES (B) HEPPS, and (C) PIPES.

and strong effects of concentration and temperature on p*K*a e.g. by tris, phosphate and citrate etc.[115] To overcome these limitations, a class of zwitterionic N-substituted aminosulfonic acid buffers with working range between pH 6.0 to 10.5 are extensively used for protein samples. The buffers are named as Good's buffers and exhibit negligible impact on biochemical and biological processes, show weak temperature dependence of p*K*a and do not bind with cations.[116, 117] Based on these characteristics, the LLPS studies discussed in this dissertation focus on HEPES, HEPPS and PIPES buffers of Good's family. However, as will be shown in Chapter 9, our studies indicated that some members of this family are not inert and affect the LLPS of lysozyme solutions. The acid-base forms of these buffers are shown in Fig. 1.4.

PART I

Salt-induced Diffusiophoresis of Lysozyme

Chapter 2

Theoretical Background of Diffusiophoresis

2.1 Introduction

This chapter reviews the mathematical details of diffusion and diffusiophoresis which were used to interpret the experimental results mentioned in the forthcoming chapters. We start with the examination of diffusion in binary systems and then extend our analysis to the ternary systems. We then conclude this chapter by introducing and discussing the diffusiophoresis of macromolecules induced by salt concentration gradients.

2.2 Diffusion in Binary System

In the limiting case of an ideal dilute solution of solute(1) in solvent(0) under isothermal conditions, the average distance between solute particles is very high and particle-particle interactions become negligible. Under these conditions, the drift velocity, $\vec{v} \equiv (v_x, v_y, v_z)$, of solute particles is given by:[30]

$$\vec{v}_1 = \frac{\vec{F}_1}{\mathrm{f}_0} \tag{2.1}$$

where $\vec{F}_1$ is the diffusion driving force and f_0 is the frictional coefficient experienced by a solute particle as it diffuse through the solvent medium. For diffusion, the driving force is the gradients of chemical potential, μ_1 of solute aka component 1, given as:.[118]

$$\mu_1 = \mu_1^0 + RT \ln C_1 \tag{2.2}$$

where μ_1^0 is a constant called the standard state chemical potential of component 1, R is the gas constant, C_1 is the molar concentration of component 1 and T is the absolute temperature. If the chemical potential of component 1, μ_1, is uniform in the system, then there will be no driving force for diffusion. However, the existence of chemical potential gradient will result the mass transfer via diffusion consistent with second law of thermodynamics, therefore the driving force, $\vec{F}$, will be;[119]

$$\vec{F} = -\frac{\nabla \mu_1}{N_A} = -\frac{k_B T}{C_1} \nabla C_1 \tag{2.3}$$

where $\nabla \equiv \left(\partial / \partial x, \partial / \partial y, \partial / \partial z\right)$. Combining Eq. 2.1 and 2.3, we obtain:[120]

$$-\vec{J}_1 = \frac{k_B T}{f_0} \nabla C_1 = D_1^0 \nabla C_1 \tag{2.4}$$

where $\vec{J}_1 = C_1 \vec{v}_1$ is the net molar flux of solute 1 and $D_1^0 = k_B T / f_0$ is the trace diffusion coefficient of solute 1. This relation is known as Einstein equation[121] and is used to describes the Brownian motion.[120] For a spherical particle and at infinite dilute solution, Stokes' law shows that $f_0 = 6\pi\eta R_h$ where η is the viscosity coefficient of solution and R_h is the hydrodynamic radius of particle[122, 123] which can be obtained from dynamic light scattering. Writing Eq. 2.4 in terms of Stock's law results the following Stokes-Einstein equation:[31]

$$D_1^0 = \frac{k_B T}{6\pi\eta R_h} \tag{2.5}$$

Equation 2.5 relates the diffusion of solute particle to the viscosity of the fluid and exhibits that the solute with large hydrodynamic radius will have small diffusion coefficient. For example, protein diffusion coefficient is lower than that of a salt. Eq. 2.5 can be used to calculate the diffusion coefficient of a solute in different medium using the viscosity data provided the hydrodynamic radius of particle remains the same. Eq. 2.4 can be extended to any arbitrary solute concentration by replacing $D_1^0 = k_B T/\mathrm{f}_0$ with $D_1(C_1)$ a parameter representing the *mutual* diffusion coefficient owning to the compensation of solvent diffusion in the opposite direction of solute molecules. $D_1(C_1)$ accounts for solute particle-particle hydrodynamic interactions and thermodynamic non-ideality. Hence generalization of Eq. 2.1 for a binary system with finite solute concentration represents a relation known as Fick's law, which is given as:[124]

$$-J_1 = D_1 \nabla C_1 \tag{2.6}$$

The vector arrow (→) on J_1 has been omitted intentionally for simplicity and this notation will be adopted henceforth. The diffusion in binary system can be described theoretically using non-equilibrium thermodynamics. As in the case of velocity and fluxes, diffusion coefficient must be defined with respect to a reference frame.[125, 126] In the solvent-fixed frame of reference, the solvent net motion in solution due to diffusion is set to zero, *i.e.*, $(J_0)_0 = 0$, where subscript "0" outside parenthesis identifies the solvent-fixed reference frame. In the volume-fixed frame of reference, the center of the system within which diffusion occurs is set to be fixed. This implies that the flux of the binary system components satisfies the condition, $(J_0)_V \bar{V}_0 + (J_1)_V \bar{V}_1 = 0$. Here, $\bar{V}_0$ and $\bar{V}_1$ represents partial molar volume of solvent and solute respectively in the volume-fixed (subscript

"*V*") reference frame.[127] The diffusion coefficient in the solvent-fixed frame, $(D_1)_0$, is related to that in the volume-fixed frame, $(D_1)_V$, by the following relation:[128, 129]

$$(D_1)_0 = \frac{(D_1)_V}{1 - C_1\bar{V}_1} \tag{2.7}$$

Note that $(D_1)_0 = (D_1)_V = D_1^0$ in the limit of ideal dilute solution ($C_1 \to 0$). The solvent-fixed diffusion coefficient, $(D_1)_0$, is more simply related to the chemical potential gradient of solute as compared to the solvent-fixed diffusion coefficient, $(D_1)_V$. Therefore the non-equilibrium thermodynamics can be invoked to describe the diffusion in the solvent-fixed frame of reference.[55, 130-132] In this reference frame, one can write;

$$-J_1 = L_1 \nabla \mu_1 \tag{2.8}$$

where the notation "( )$_0$" has been omitted in Eq. 2.8 for simplicity. L_1 is referred as Onsager transport coefficient.[37, 133, 134] For a general (non-ideal) solution, the chemical potential of neutral solute(1) can be expressed as $\mu_1 = \mu_1^0 + RT \ln f_1 C_1$, where f_1 represents the activity coefficient of solute 1. In the case of electrolytes, the chemical potential becomes, $\mu_1 = \mu_1^0 + \nu_1 RT \ln f_1 C_1$ where ν is the number of ions in the electrolyte; e.g. $\nu = 2$ for NaCl. After comparing Eq. 2.8 with Fick's law relation (Eq. 2.6), we obtain:

$$D_1 = L_1 \mu_{11} \tag{2.9}$$

where $\mu_{11} = (\partial \mu_1 / \partial C_1)_{T,P} = (RT / C_1) y_1$ represents the chemical potential derivative of component 1 ($\mu_{11} = (\nu_1 RT / C_1) y_1$ for electrolytes). The coefficient $y_1 \equiv (1 + d \ln f_1 / d \ln C_1)$ is the thermodynamic corrective factor for the non-ideality of solution with $y_1 = 1$ in the limit of $C_1 \to 0$

. Eq. 2.9 establishes the relationship between diffusion and thermodynamics. At infinite dilution, $\mu_{11} = RT / C_1$, we therefore have:

$$D_1^0 = RT \frac{L_1}{C_1} \tag{2.10}$$

2.3 Diffusion in Ternary System

Equation 2.6 can be expanded to a ternary solute(1)-solute(2)-solvent(0) system, such as:

$$-J_1 = D_{11}\nabla C_1 + D_{12}\nabla C_2 \tag{2.11}$$

$$-J_2 = D_{21}\nabla C_1 + D_{22}\nabla C_2 \tag{2.12}$$

where D_{11} and D_{22} are the diffusion coefficients of solute(1) and solute(2) components induced by their own concentration gradients ∇C_1 and ∇C_2 respectively. These diffusion coefficients are closely related to corresponding diffusion coefficients D_1 and D_2 of binary solute(1)-solvent and solute(2)-solvent binary systems. The off-diagonal diffusion coefficients D_{12} and D_{21} are denoted as cross-diffusion coefficients and describe the diffusion of one solute induced by the concentration gradient of other solute. In the present case, solute(1) and solute(2) corresponds to protein (lysozyme) and salt (KCl, NaCl or $MgCl_2$) respectively. Hence, D_{12} describes the flux of lysozyme induced by the concentration gradient of salt while D_{21} describes the flux of salt induced by the concentration gradient of lysozyme.[36] The cross-diffusion terms, D_{12} and D_{21}, in Eq. 2.11 and 2.12, vanishes as $C_1 \to 0$ and $C_2 \to 0$ respectively. As in the case of the binary system, the solvent-fixed frame remains *i.e.,* $(J_0)_0 = 0$ and in the volume-fixed frame of reference, the flux of ternary system components also satisfies the condition, $(J_0)_V \bar{V}_0 + (J_1)_V \bar{V}_1 + (J_2)_V \bar{V}_2 = 0$. Here, J_i

and $\bar{V}_i$ represent the molar flux and partial molar volume of component *i* in the system respectively. Eq. 2.7 can be expanded for ternary components to express the link between solvent-fixed frame coefficients, $(D_{ij})_0$ and volume-fixed frame coefficients, $(D_{ij})_V$:[128, 129]

$$(D_{11})_0 = (D_{11})_V + [C_1 / (1 - C_1\bar{V}_1 - C_2\bar{V}_2)][\bar{V}_1(D_{11})_V + \bar{V}_2(D_{21})_V] \quad (2.13)$$

$$(D_{12})_0 = (D_{12})_V + [C_1 / (1 - C_1\bar{V}_1 - C_2\bar{V}_2)][\bar{V}_1(D_{12})_V + \bar{V}_2(D_{22})_V] \quad (2.14)$$

$$(D_{21})_0 = (D_{21})_V + [C_2 / (1 - C_1\bar{V}_1 - C_2\bar{V}_2)][\bar{V}_1(D_{11})_V + \bar{V}_2(D_{21})_V] \quad (2.15)$$

$$(D_{22})_0 = (D_{22})_V + [C_2 / (1 - C_1\bar{V}_1 - C_2\bar{V}_2)][\bar{V}_1(D_{12})_V + \bar{V}_2(D_{22})_V] \quad (2.16)$$

Non-equilibrium thermodynamics can be applied in the solvent-fixed reference frame and can be extended to the ternary system. Accordingly, Eq. 2.8 can be expanded as:

$$-J_1 = L_{11}\nabla\mu_1 + L_{12}\nabla\mu_2 \quad (2.17)$$

$$-J_2 = L_{21}\nabla\mu_1 + L_{22}\nabla\mu_2 \quad (2.18)$$

Here again, the subscript "0" has been omitted for simplicity. The term, L_{ij} (*i*,*j* = 1,2), represents Onsager transport coefficients and in the solvent-fixed frame of reference, these coefficients will obey Onsager reciprocal relationship $L_{12} = L_{21}$. The combination of Eq. 2.11, 2.12 and Eq. 2.17, 2.18 will result:

$$D_{11} = L_{11}\mu_{11} + L_{12}\mu_{21} \quad (2.19)$$

$$D_{12} = L_{11}\mu_{12} + L_{12}\mu_{22} \quad (2.20)$$

$$D_{21} = L_{21}\mu_{11} + L_{22}\mu_{21} \quad (2.21)$$

$$D_{22} = L_{21}\mu_{12} + L_{22}\mu_{22} \tag{2.22}$$

These relations show that ternary diffusion coefficients are the linear combinations of Onsager coefficients and thermodynamic factors. The cross terms will be large if $\mu_{ij} \equiv (\partial \mu_i / \partial C_j)_{T,P,C_k,k\neq j}$ is large even if the Onsager coefficients L_{ij} are zero.

2.4 Diffusiophoresis of Macromolecules in the Presence of Salts

If v_1 is the net diffusion rate of a macromolecule "1" with respect to the solvent-fixed reference frame, we have $(J_1)_0 = C_1 v_1$. In the presence of salt "2" with concentration C_2 and chemical potential gradient $\nabla\mu_2$, we can then write according to Eq. 2.17:

$$-v_1 = \frac{(L_{11})_0}{C_1}\left(\nabla\mu_1 + \frac{(L_{12})_0}{(L_{11})_0}\nabla\mu_2\right) \tag{2.23}$$

In the limit of $C_1 \to 0$, we can write[135]:

$$v_1 = -D_1^0\left(\nabla \ln C_1 + \hat{D}_{12}\frac{\nabla\mu_2}{RT}\right) \tag{2.24}$$

The description of diffusiophoresis provided by Eq. 2.24 is analogous to the electrokinetic equation employed for electrophoresis in the presence of external electric field, where an external gradient of electrical potential replaces the gradient of salt chemical potential. Eq. 2.24 is equivalent to Eq. 2.23, where interconversion is obtained after differentiating $\mu_1(C_1, \mu_2)$ in Eq. 2.23 in the limit of $C_1 \to 0$. The trace-diffusion coefficient of macromolecule, $D_1^0 = (L_{11})_0 / C_1$, characterizes its aqueous Brownian mobility at infinite dilution. The salt thermodynamic driving force, $\nabla\mu_2$, responsible for diffusiophoresis can be given as:

$$\frac{\nabla \mu_2}{RT} = \frac{\nu_2 y_2}{C_2} \nabla C_2 \tag{2.25}$$

where factor $1/C_2$ is the salt thermodynamic ideality and is dominant at low salt concentration. The factor $y_2 \equiv (1 + d \ln f_2 / d \ln C_2)$ is the thermodynamic factor of the binary salt-water system with f_2 being the corresponding activity coefficient of the salt. The values of $y_2(C_2)$ are available through the literature. The factor ν_2 represents the moles of ions per mole of salt, with $\nu_2 = 2$ for NaCl and KCl and $\nu_2 = 3$ for $MgCl_2$.

Equation 2.20 can be used to relate $(L_{12})_0$ to $(D_{12})_0$ in Eq. 2.23.[136] Comparison with Eq. 2.24 then yields:

$$\hat{D}_{12} = \frac{C_2}{\nu_2 y_2 D_1^0} \lim_{C_1 \to 0} \left[\frac{(D_{12})_0}{C_1} \right] \tag{2.26}$$

where we have also used Eq. 2.25 for $\nabla \mu_2$. Note that D_1 is the function of salt concentration. The values of macromolecule trace diffusion coefficient $D_1^0(C_2)$ can be obtained from the known value of $D_1^0(0)$ in water and from available viscosity data on binary salt-solvent system using $D_1^0(C_2) = D_1^0(0) / \eta_{r,2}(C_2)$ where $\eta_{r,2}(C_2)$ is the value of relative viscosity at C_2.[137] To determine $\hat{D}_{12}$ from Eq. 2.25, experimental values of D_{12} are needed.

2.5 Concentration Profile of Macromolecules in a Steady-state Diffusiophoresis

In recent studies of poly(ethylene glycol) (PEG) diffusiophoresis induced by salt concentration gradients in aqueous ternary mixture,[41, 48] it was found that the diffusiophoresis of macromolecules

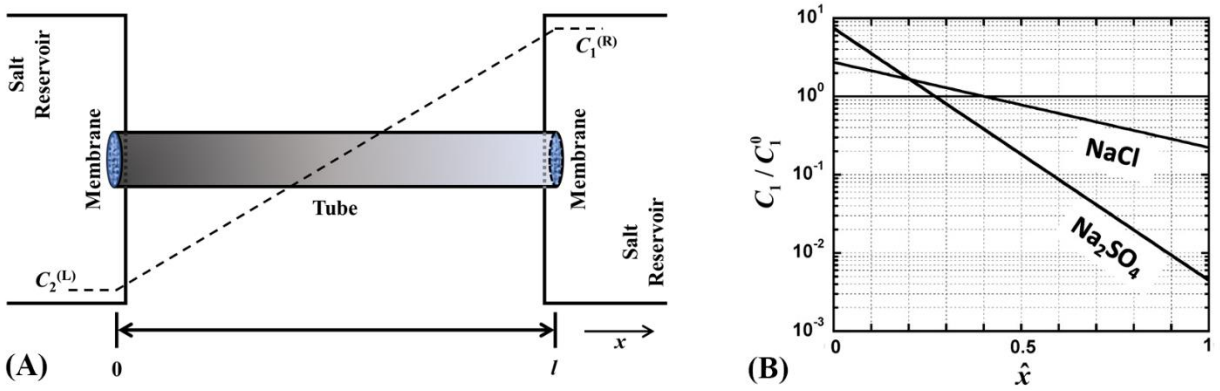

Figure 2.1 (A) Schematic diagram showing a tube of length, l containing a macromolecular solution, located along the x-axis and connected to two salt reservoirs through two semipermeable membranes. The corresponding salt concentration profile in steady-state conditions is described as a dashed line with positive slope. (B) Adopted from Ref. [41], a logarithmic diagram showing three normalized polymer concentration profiles, as a function of the normalized position inside the tube obtained for B = 0 (baseline), B = 2.5 (NaCl), and B = 7.4 (Na_2SO_4) .

is significantly dependent on the nature of the salt and can be exploited in diffusion based mass-transport processes. The significance of polymer diffusiophoresis was analyzed theoretically in terms of macromolecule concentration profile under steady-state conditions. This theoretical analysis will be extended and generalized to salt-induced diffusiophoresis of proteins in Chapter 5. Here we review the basic analysis introduced for diffusiophoresis of neutral macromolecule in the presence of a salt with negligible thermodynamic non-ideality ($y_2 = 1$).

To model the concentration profile in steady-state diffusiophoresis, we consider the diffusion of macromolecule occurring along the x direction of a hypothetical tube of length, l, having semipermeable membranes at its two ends (see Fig. 2.1A). Both tube ends are interfaced with salt-water reservoirs having different salt concentrations, $C_2 = C_2^{(L)}$ and $C_2 = C_2^{(R)}$ at $x = 0$ and $x = l$, respectively. Steady-state conditions inside the tube are achieved by maintaining the salt concentrations constant in both reservoirs. If salt diffusion coefficient is approximated to be a constant, then; $C_2 = C_2^{(L)} + \Delta C_2 (x / l)$. This implies that $dC_2 / dx = \Delta C_2^{(L)} / l$. If a uniform macromolecular solution at low concentration, C_1^0, is initially inserted in the tube, the salt

concentration gradient caused by the two reservoirs will induce a non-uniform macromolecule concentration, C_1, due to diffusiophoresis. Since the macromolecules cannot cross the two membranes, the condition $v_1 = 0$ must be respected throughout the tube in steady-state conditions. Thus Eq. 2.24 becomes

$$\frac{d \ln C_1}{y_2 dC_2} = -\nu_2 \frac{\hat{D}_{12}}{C_2} \tag{2.27}$$

If we set the salt thermodynamic non-ideality y_2 = 1, Eq. 2.27 can be rewritten in the following way:

$$\frac{d \ln C_1}{dC_2} = -w \tag{2.28}$$

where $w = \nu_2 \hat{D}_{12} / C_2$ ($\nu_2 = 2$ for NaCl and $\nu_2 = 3$ for Na_2SO_4) can be approximated as a constant because $\hat{D}_{12}$ is directly proportional to C_2 for neutral macromolecules.[41, 48] Integration of Eq. 2.28 with respect to x = 0 then yields:

$$C_1 = C_1(0) \exp(-w \Delta C_2 x / l) \tag{2.29}$$

where we have used $dC_2 / dx = \Delta C_2 / l$ and $C_1(0)$ is the concentration of macromolecule at x = 0. This concentration can be replaced by the initial uniform macromolecule concentration, C_1^0, using the following mass balance relationship:

$$C_1^0 = \frac{1}{l} \int_0^l C_1 dx = \frac{2C_1(0)}{w \Delta C_2} \sinh(w \Delta C_2 / 2) \tag{2.30}$$

Thus, substitution of $C_1(0)$ with C_1^0 in Eq. 2.29 yield

$$\hat{C}_1 = \frac{B\exp(-B\hat{x})}{2\sinh(B/2)} \tag{2.31}$$

where $\hat{C}_1 = C_1 / C_1^0$, $\hat{x} \equiv x/l$ and $B \equiv w\Delta C_2$. Figure 2.1(B) shows a representative normalized concentration profile of a polymer induced by NaCl (B = 2.5) and Na_2SO_4 (B = 7.4) with osmolar-concentration difference of 1M (ΔC_2 = 0.50M for NaCl and ΔC_2 = 0.33M for Na_2SO_4), adopted from Ref. [41]. The logarithmic profile illustrates that polymer concentration is enhanced and depleted near the left and right membrane locations respectively. In the case of NaCl, the polymer concentration near the left compartment is predicted to be 2.7 times the value of C_1^0, while that near the right compartment is predicted to be 22% of C_1^0. However, in the case of Na_2SO_4, diffusiophoretic effects are more drastic with the corresponding enhancement and depletion of polymer are given by $y(0)$ = 7.4 and $y(l)$ = 0.0044, respectively. These findings encourage to extend these studies for the diffusiophoresis of protein to better elaborate the applications for diffusion-based mass-transport processes. However, this analysis needs to be generalized to the case of charged macromolecules such as proteins. Furthermore, the assumption of y_2 = 1 is not expected to be reasonable for salts in general, especially at high salt concentration ($C_2 > 1$M). Thus, a more accurate analysis should include effects of salt thermodynamic non-ideality. This will be investigated in Chapter 5.

Chapter 3

Materials and Experimental Methods

3.1 Materials and Solution Preparation

Two-times recrystallized and lyophilized egg white lysozyme used in this work was from lot 39E11265A, obtained from Worthington Biochemical Corporation, NJ, USA. Reagent grade NaCl (99.71%), KCl (99.71%), and $MgCl_2$ (99.71%) were obtained from Thorn Smith, MI, USA and $NaNO_3$ with 99.1% purity was obtained from J. T Bakers Chemical Co. NJ, USA. All these reagents were used without further purification. Deionized water was passed through a four-stage Millipore filter system to provide high-purity water for all the experiments. All the potentiometric measurements were made in the water thermostat (25.00±0.05ºC) using Thermo Scientific Orion 3 Star pH/mV meter equipped with Orion combination pH micro glass electrode (model 8220BNWP). The chloride ions potentiometric measurements were carried out using Cole-Parmer chloride ion-selective electrode (model K-27502-13) containing 1M KNO_3 internal reference solution.

The stock solutions of protein and salts were prepared by weight with appropriate buoyance corrections using a Mettler-Toledo AT400 electrobalance to 0.1 mg. Protein concentrations in aqueous solutions were determined based on UV absorption at 280 nm (DU 800

spectrophotometer, Beckman Coulter), using the extinction coefficient value of 2.64 $mg^{-1}\cdot mL\cdot cm^{-1}$.[138] Molar concentrations were calculated using the lysozyme molar weight of 14.307 $kg\cdot mol^{-1}$ at the isoelectric point (~11). Absorbance values showed that the lyophilized powder of lysozyme contains a protein weight fraction of 0.885±0.05. Thus, protein stock solutions were prepared by weight and their concentrations corrected by the factor of 0.885. This value of 0.885 was based on the ratio between the observed extinction coefficients (around 23.2-23.4) and the literature experimental value of 26.4.

3.2 Density Measurements

To further examine the employed lysozyme material, density measurements were performed on ≈1% protein solutions using a computer-interfaced Mettler-Paar DMA40 density meter. The vibrating tube in the density meter was thermostated with a large water bath well-regulated at 25.00 ºC with temperature controlled at 0.001ºC. The density, *d*, of solution is related to the vibration period *T* of the tube as[139, 140]:

$$d = A + BT^2 \tag{3.1}$$

where *A*, and *B* are the instrument constants determined using two reference periods which were chosen to be water with density 0.997045 g/cm^3 (at 25 ºC) and air with density 0.00115 g/cm^3. The density of air was calculated by employing a state equation depending on temperature, pressure and humidity.

The obtained density values were utilized to calculate the specific lysozyme volume of ν_1 =0.715±0.01 $cm^3\cdot g^{-1}$ (molar volume of 10.2 $dm^3\cdot mol^{-1}$) based on $\nu = w_1\nu_1 + (1-w_1)\nu_0$, where w_1 is the protein weight fraction, and ν, ν_1 and $\nu_0 = 1.003$ $cm^3\cdot g^{-1}$ are the specific volumes of

solution, protein and water, respectively. This specific volume value were in agreement with volumetric data previously reported on lysozyme [87].

3.3 Determination of Protein Dry Weight

To estimate the percentage of water contents in protein, weighted amount of protein samples was taken in three dry vials. These vials were placed in a vacuum oven at 60 ˚C for 5 days. The water contents were estimated from weight loss of protein samples. The table 3.1 shows the comparison between protein initial weight and weight measured. The final average weight of the samples was found to be 0.914 ± 0.05 of their initial values. The water contents were calculated to be 8.6% in protein.

Table 3.1 Analysis of water contents in Lysozyme

Sample	Initial weight (g)	Final Weight (g)	Wight loss (g)
1	0.1440	0.1318	0.0122
2	0.1478	0.1343	0.0135
3	0.1282	0.1177	0.0105

3.4 Determination of Chloride Ions in a Protein Molecule

The number of Cl^- ions in each protein molecule were determined using the Fajans method.[50] The 0.001 M protein titrand solution was prepared by weight by dissolving calculated amount of lysozyme in 10 g of deionized water. The pH of this solution was maintained at 7 using a standardized 0.05M NaOH solution in water. In this solution 13 μL of dichlorofluorescein dye was added along with 1 mg of Dextrin. The former works as indicator while later prevents AgCl coagulation. In this solution, 0.1 M $AgNO_3$ titrant was added dropwise using a plastic syringe

equipped with capillary tubing till the end point was achieved. The whole process was repeated thrice and average value of Cl^- ion were used for estimation of charge on protein at different pH.

3.5 Determination of Free Chloride Concentration in Protein

The free chlorides present in protein solution were quantified by potentiometric measurements in 0.1M $NaNO_3$ solution at pH of 4.5. The 5% stock lysozyme solution by weight was prepared by dissolving calculated amount of solid lysozyme in deionized water. The percent solution was converted to molar concentration using molecular weight of lysozyme. Three dilutions (0.3mM, 0.6mM, 1.2mM) of protein stock solution were prepared in 0.1M $NaNO_3$ solution. Calibration curve for chloride ions was constructed using nine solutions of NaCl with different concentrations (range: 0.5-10mM) in 0.1M $NaNO_3$ aqueous solution. The potentiometric measurements were carried out at 25.00±0.05 ˚C in a water bath using chloride ion-selective electrode. The Cl^- ions potential (mV) in three dilutions of protein were measured and free Cl^- ions were calculated by taking the ratio of the measured Cl^- ions concentration to the protein molar concentration.

3.6 Preparation of Solutions for Protein Charge Determination

In order to determine the excess protonation state, hence the charge, on lysozyme at different pH in the presence of NaCl, KCl and $MgCl_2$, the 5% aqueous lysozyme stock solution was prepared by weight. The 10% (by weight) stock solutions of NaCl, KCl were prepared in deionized water. These solutions were diluted to the target concentrations (0.1M, 0.25M, 0.5M, 0.9M) using the molar masses of NaCl and KCl. The 10% (by weight) stock solutions of $MgCl_2 \cdot 6H_2O$ was also prepared in deionized water and its exact concentration was determined by density measurements and fitting the measured density data to polynomial model $d = d_0 + \sum_{i=2}^{n} A_i (\mathrm{W\%})^{i/2}$ of Miller *et al*[56] where $d_0 = 0.997045$ g.cm^{-3} is the density of pure water, A_i are the coefficients determined

using fitting and the concentration in W% units. The polynomial coefficients used for the fitting are mentioned in table 3.2. The original model was based on mol/kg and mol/dm^3 concentration units which was converted to W% units. The difference between experimental densities mentioned by Miller *et al*., and the modified least-square W% fit was of order of 10^{-5} as can be seen in Fig. 3.1. Owning to excellent prediction of densities, this model was used to calculate the exact W% of $MgCl_2$ in its 10% stock solution.

Table 3.2 Values of the coefficients A_i used in the density expression $d = d_0 + \sum_{i=2}^{n} A_i (\mathrm{W\%})^{i/2}$

A_2	0.0099180266000
A_3	-0.0024866849000
A_4	0.0014121360000
A_5	-0.0003726409900
A_6	0.0000483716150
A_7	-0.0000023844769

The stock solution of $MgCl_2$ was diluted to the target concentrations (0.1M, 0.5M, 0.9M) using molar masses of 95.211 g/mol by excluding the molar mass of six water molecules. The ternary solution of lysozyme (0.6mM by weight) was prepared by diluting its stock solution in NaCl, KCl and $MgCl_2$ dilutions. The 0.05M stock NaOH solution was prepared in deionized water using standard procedure and was standardized against primary standard Potassium Hydrogen Phthalate. The 0.05M stock HCl solution was prepared by dilution using its standard molarity and was standardized against NaOH. To keep the concentration of salts constant in the ternary solution, HCl and NaOH solutions used to control the pH, were also prepared in solution bearing the same concentration of salts as in ternary solution.

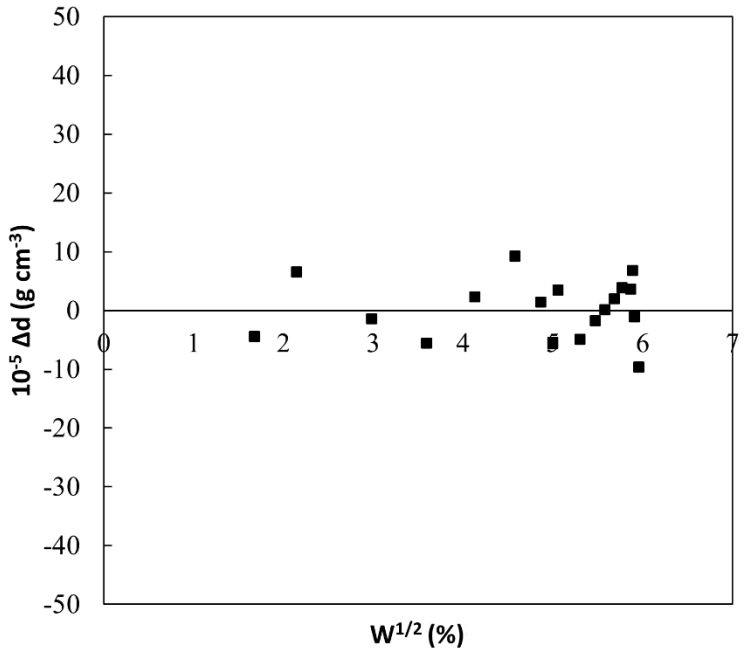

Figure 3.1 Difference between experimental literature densities and our calculated densities using polynomial model for $MgCl_2 \cdot 6H_2O$.

3.7 Acid-Base Titrations for Protein Charge Determination

The excess protonation state, v_H of a protein represents the number of protons in excess with respect to the number of protons, χ_H, bound to the protein at the isoelectric point. For example, if the protonation state of the protein is 10 ($\chi_H = 10$) at its isoelectric point and then the solution pH is decreased such that the new protonation state becomes 12, we then deduce that $v_H = 2$. To determine the excess protonation state, a 10g aliquot of ternary solution was taken as titrand in an Erlenmeyer flask and was placed in a water bath at temperature 25.00 ± 0.05 °C. A double junction glass-combination micro electrode connected to pH meter and calibrated using pH 4.00 and pH 7.00 standards was inserted in the flask along with a glass stirring rod. The HCl titrant solution was taken in a plastic syringe fitted with a plastic tubing. The weight of empty syringe and filled

with HCl salt solution was measured and this solution was added drop by drop in titrand solution. The weight of syringe was measured again after each successive addition till the pH was change from initial pH to final pH of ~3.0. The added mass of HCl salt solution was converted into volume using the density of solution. The excess protonation state was calculated using the charge balance relation:

$$\nu_H = \nu_C^o + \Delta\nu_C - ([H_3O^+] - [OH^-]) / C_1 \quad (3.2)$$

where ν_C^o is the initial number of chloride ions per protein molecule determined as mentioned in section 3.4, $\Delta\nu_C$ is the chloride ions per protein molecule from titrant, C_1 is the protein molar concentration in the final solution and $[H_3O^+]$ and $[OH^-]$ are the molar concentrations of hydronium and hydroxide ions, respectively discussed in next section. Similar procedure was adopted for pH change from initial pH to pH 7.0 using salt solutions of NaOH.

3.8 Determination of H^+ Ion Concentration from pH

The measured pH of solution cannot be used directly to calculate the concentration of H^+ ions due to the difference in concentration and activity. To account for the activity corrections for H^+ ion in the given electrolyte solution, we performed a calibration curve between measured pH and $-\log[H^+]$ of the solution. Initially HCl solution of concentration 0.001 ($-\log[H^+] = 3$) was prepared in deionized water and salt solutions of NaCl, KCl and $MgCl_2$ with concentrations mentioned in Section 3.6 were prepared using this HCl solution. These salt solutions were used to prepare a series of solutions having $-\log[H^+]$ between 3.00 and 4.00 with difference of 0.25 $-\log[H^+]$ units. The pH of these solutions was measured using pH/mV meter equipped with Orion combination pH micro glass electrode. It was ensured that the pH/mV meter, glass electrode and calibration standards are the same as those used for potentiometric measurements of ternary protein

solutions mentioned in Section 3.6. The obtained results were analyzed in terms of Pitzer model[141] on KaleidaGraph as given in Eq. 3.3:

$$-\log[H^+] = \text{pH} + a + b \cdot 10^{-\text{pH}} \tag{3.3}$$

where *a* and *b* are the coefficients obtained from curve-fitting analysis. Eq. 3.3 is based on the assumption that the corrective term ($a + b \cdot 10^{-\text{pH}}$) is linear with the concentration of H^+ ions. The obtained concentration of H^+ ions was used to determine the value $v_{\mathbf{H}}$ using procedure detailed in Section 3.7.

Chapter 4

Behavior of Lysozyme Diffusiophoresis Coefficients in the Presence of Salts

4.1 Extraction of Lysozyme Diffusiophoresis Coefficients

In order to study the salt-induced diffusiophoresis of lysozyme, its diffusiophoresis coefficients were extracted from previously reported experimental multicomponent diffusion-coefficient data.[36, 51, 142] Specifically, ternary diffusion coefficients in the volume-fixed reference frame, $(D_{ij})_V$ with $i, j = 1, 2$ for protein (1) and salt (2), are available at the lysozyme concentration of $C_1 = 0.600\,\text{mM}\,(8.58\ \text{g}\cdot\text{L}^{-1})$ as a function of salt concentrations (C_2) at 25 °C. From now on, for the sake of clarity the terminology "P" for protein and "S" for salts will replace the more generalized terminology of '1" and "2" used for macromolecule and salts respectively in Chapter 2. As described in section 2.4 (Eq. 2.26), the diffusiophoresis coefficient is related to the cross-diffusion term divided by the concentration of macromolecule. We rewrite Eq. 2.26 as[136]:

$$\hat{D}_{\text{PS}} \equiv \frac{C_{\text{S}}}{\nu_{\text{S}}\, y_{\text{S}} D_{\text{P}}^{0}} \lim_{C_{\text{P}}\to 0} \frac{D_{\text{PS}}}{C_{\text{P}}} \tag{4.1}$$

At low protein concentration, experimental values of the ratio $(D_{\text{PS}})_V / C_{\text{P}}$ are known to be independent of C_{P} within the experimental error.[36, 48] We therefore set them to be equal to $\lim_{C_{\text{P}}\to 0}[(D_{\text{PS}})_V / C_{\text{P}}]$. For the protein tracer-diffusion coefficient, $D_{\text{P}}^{0}(C_{\text{S}})$, we use: $D_{\text{P}}^{0}(0) = 0.132\times 10^{-9}\,\text{m}^2\cdot\text{s}^{-1}$.[137] The dependence of D_{P}^{0} on salt concentration C_{S}, was calculated

from available[143, 144] viscosity data on binary salt-solvent systems using $D_{\mathrm{P}}^{0}(C_{\mathrm{S}}) = D_{\mathrm{P}}^{0}(0) / \eta_{\mathrm{r,S}}(C_{\mathrm{S}})$,[145] where $\eta_{\mathrm{r,S}}(C_{\mathrm{S}})$ is the value of relative viscosity at C_{S}. Thermodynamic and transport coefficients of binary salt-water systems are given in Table 4.1. As detailed in section 2.2, to convert volume-fixed diffusion coefficients into the corresponding solvent-fixed values, $D_{\mathrm{PS}} / C_{\mathrm{P}}$, the terms $\bar{V}_{\mathrm{S}} D_{\mathrm{S}}$ was added to $(D_{\mathrm{PS}})_{V} / C_{\mathrm{P}}$, where $\bar{V}_{\mathrm{S}}(C_{\mathrm{S}})$ and $D_{\mathrm{S}}(C_{\mathrm{S}})$ are the partial molar volume and solvent-fixed diffusion coefficient of the salt component in the binary salt-water mixtures, respectively.[127, 136] Finally, $\hat{D}_{\mathrm{PS}}(C_{\mathrm{S}})$ was calculated from $D_{\mathrm{PS}} / C_{\mathrm{P}}$ using Eq. 4.1 with $\nu_{\mathrm{S}} = 2$ for NaCl and KCl, and $\nu_{\mathrm{S}} = 3$ for $MgCl_2$.

Table 4.1. Thermodynamic and transport properties of aqueous potassium chloride, sodium chloride and magnesium chloride at 25 ºC.

Salt	C_{S} / M	$\bar{V}_{\mathrm{S}} / \mathrm{cm}^3 \cdot \mathrm{mol}^{-1}$	y_{S}	$D_{\mathrm{S}} / 10^{-9} \mathrm{m}^2 \cdot \mathrm{s}^{-1}$	$\eta_{r,\mathrm{S}}$
Potassium chloride	0.250	28.3	0.900	1.851	0.999
	0.500	28.9	0.904	1.876	0.998
	0.900	29.7	0.927	1.934	0.997
	1.200	30.3	0.950	1.985	0.998
	1.500	30.7	0.976	2.040	1.000
Sodium chloride	0.250	18.0	0.919	1.620	1.023
	0.500	18.6	0.937	1.602	1.047
	0.650	18.9	0.953	1.587	1.062
	0.900	19.4	0.983	1.559	1.088
	1.300	20.0	1.038	1.512	1.132
Magnesium chloride	0.093	17.4	0.863	1.044	1.041
	0.233	18.8	0.927	1.039	1.102
	0.464	20.2	1.077	1.056	1.206
	0.930	22.8	1.466	1.094	1.447
	1.599	25.9	2.201	1.125	1.911
	2.000	27.3	2.717	1.118	2.285

4.2 Effects of Salt Type on Lysozyme Diffusiophoresis

The experimental behavior of salt-induced lysozyme diffusiophoresis, $\hat{D}_{PS}$, as a function of salt concentration, C_S, is shown in Fig 4.1 for the NaCl, KCl and $MgCl_2$ cases. In the $MgCl_2$ case, diffusiophoresis data cover salt concentrations as high as 2 M, while the salt concentration range is somewhat reduced for the other two salts cases due to a relatively low lysozyme solubility.[51, 53] For all three salts, $\hat{D}_{PS}(C_S)$ is positive, thereby implying that protein migration occurs from high to low salt concentration. At low salt concentrations, values of $\hat{D}_{PS}$, are predicted to be positive from an electrophoretic mechanism[36, 38] which will be discussed quantitatively in Chapter 6. This electrophoretic mechanism is related to salt chemical potential gradient been able to produce an internal electric field due to the difference in the mobility of salt ionic components. This mechanism makes diffusiophoresis similar to electrophoresis. If the negatively charged ions of salt

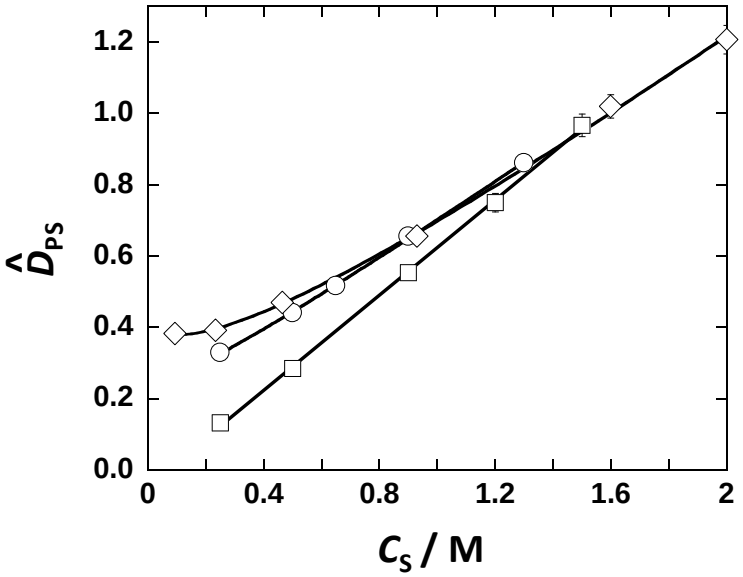

Figure 4.1 Lysozyme diffusiophoresis coefficient, $\hat{D}_{PS}$, as a function of salt concentration, C_S, for the NaCl (circles), KCl (squares) and $MgCl_2$ (diamonds) cases. Solid curves are calculated fits through the data.

have higher mobility along the salt chemical potential gradient as compared to the positively charged ions, a charge separation can potentially occur. This is responsible for a gradient of electric potential also known as diffusion potential. In this case the internal electric field is oriented towards higher salt chemical potential. Thus, a positively charged protein will migrate towards low salt chemical potential, consistent with electric field orientation. This mechanism is illustrated in Fig. 4.2. Hence, the internal electric field produced by the salt concentration gradients is predicted to induce migration of positively-charged lysozyme from high to low salt concentration. This analysis allows us to deduce that $\hat{D}_{PS}$ increases with the difference in mobility between the relatively fast chloride anion (counterion for positively charged proteins) and that of the slower metal cations (coions), which are positive in all three salt cases.[146] At low C_S, the magnitude of diffusiophoresis was found to be the largest in the $MgCl_2$ case and close to zero in the KCl case. This is qualitatively consistent with the known ranking in ion mobility: $Cl^- \approx K^+ > Na^+ > Mg^{2+}$.[146]

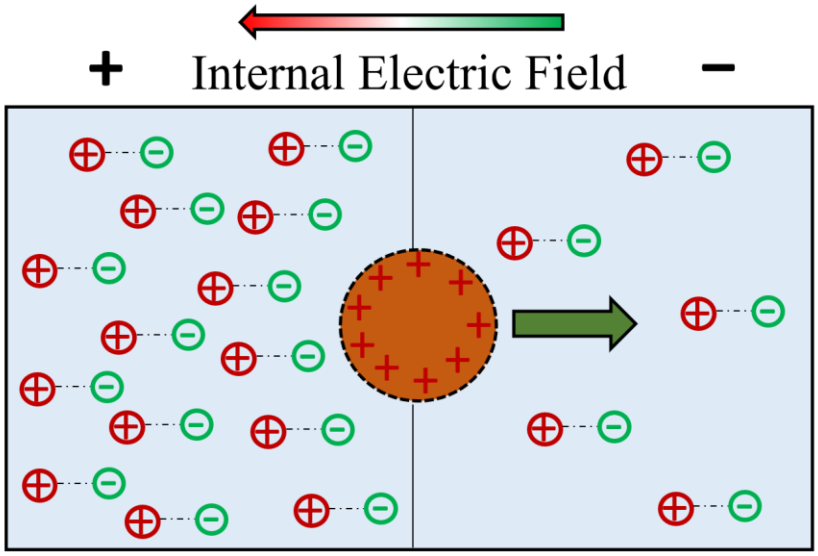

Figure 4.2 Migration of a positively charged macromolecule under the influence of a salt chemical potential gradient. In this case anions tend to diffuse faster than cations, thereby creating an internal electric field pointing from low to high salt concentration (see arrow on the top). Correspondingly, the positively charged macromolecule will migrate from high to low salt concentration due to this internal electric field.

As C_S increases, diffusiophoresis also increases, with the value of $\hat{D}_{PS}$ becoming approximately the same in all three salt cases. The magnitude of $\hat{D}_{PS}$ at relatively high salt concentrations has been linked to protein preferential hydration and salting-out strength,[36, 41] which also drives protein migration from high to low salt concentration. Note that this type of mechanism has been also considered for colloidal particles when considering the case of non-electrolyte gradients.[29, 147] In our case, a weak dependence of $\hat{D}_{PS}$ on the nature of the chloride salt at high C_S is consistent with the Hofmeister series,[41, 145] which indicates that the nature of the cation is significantly less important than that of the anion in the salting-out ranking of salts. In Chapter 6 a quantitative theoretical examination of lysozyme diffusiophoresis is provided based on the electrophoretic mechanism.

4.3 Analysis of Salt Thermodynamic Driving Forces

To assess the impact of a salt concentration gradient on protein diffusiophoresis, it is also important to consider the magnitude of the salt thermodynamic driving force. This is represented by the difference in salt chemical potential that can be established in a protein aqueous mixture. Since lysozyme solubility in aqueous $MgCl_2$ is relatively high compared to that with NaCl and KCl,[148] relatively large differences in $MgCl_2$ concentrations can be established. This leads to gradients, ∇C_S of $MgCl_2$ concentration that are relatively large. Furthermore, it is also important to examine how a salt concentration gradient translates into the corresponding gradient of salt chemical potential. For salts, we can rewrite Eq. 2.25 of Chapter 2 as:[41]

$$\frac{\nabla \mu_S}{RT} = \nu_S y_S \frac{\nabla C_S}{C_S} \tag{4.2}$$

The mole of ions per mole of salt is $\nu_S = 3$ for $MgCl_2$, a value that is 50% larger than that of NaCl and KCl ($\nu_S = 2$). In Eq. 4.2 $y_S = 1$ in the limit of $C_S \to 0$ because the solution becomes ideal at the infinite dilution. Thermodynamic data on binary salt-water systems[55, 56] given in Table 4.1 show that y_S decreases down to $y_S = 0.9$ at ionic strengths of about 0.2 M in all three salt cases (this ionic strength corresponds to 0.1 M $MgCl_2$ concentration) and then increases as salt concentration further increases. Interestingly, this thermodynamic factor remains about $y_S \approx 1.0$ for NaCl and KCl within the experimental salt concentration range, while it becomes significantly large for $MgCl_2$. Specifically, the $MgCl_2$ thermodynamic factor becomes $y_S = 1.5$ at C_S = 1 M and further increases to $y_S = 2.7$ at C_S = 2 M. We therefore conclude that the factor $\nu_S y_S$ in Eq. 4.2 is significantly large for the $MgCl_2$ case compared to other two salt cases as can be seen in table 4.1.

4.4 Relative Ranking of Salts

This section summarizes our results on the relative effectiveness of the investigated chloride salts on lysozyme diffusiophoresis. The lysozyme diffusiophoresis coefficient, $\hat{D}_{PS}$, at low salt concentration, is found to have a large magnitude in the $MgCl_2$ case followed by the NaCl and KCl cases, respectively. Furthermore, for $MgCl_2$, the thermodynamic driving forces discussed in Eq. 4.2 was also found to be relatively large because both ν_S and y_S are higher for $MgCl_2$ than for the other two salts. Finally, the accessible gradient of salt concentrations, ∇C_S are also relatively large for $MgCl_2$ due to the higher solubility of lysozyme in the presence of salt. This analysis allows us to conclude that diffusiophoresis effects are expected to be relatively large for positively charged proteins in the presence of $MgCl_2$ concentration gradients. In Chapter 5, the magnitude of

protein diffusiophoresis in the presence of $MgCl_2$ concentration gradients will be discussed by examining the theoretical mass transport process introduced in Chapter 2.

Chapter 5

Role of Diffusiophoresis on Protein Transport

5.1 Protein Concentration Profile in Steady-state Diffusiophoresis

To characterize diffusiophoresis effects, we extended the theoretical examination of the diffusion-based transport process of section 2.5 to lysozyme subject to a steady-state concentration gradient of $MgCl_2$. The theoretical examination in section 2.5 assumed $\hat{D}_{PS}$ directly proportional to C_S and consequently $w = \nu_S \hat{D}_{PS} / C_S$ to be constant. This is a good approximation only for neutral macromolecules such as PEG. Indeed, as we can deduce from Fig. 4.1, $\hat{D}_{PS}(C_S)/C_S$ is not a constant because $\hat{D}_{PS}$ does not approaches zero at low C_S. Furthermore, salt thermodynamic non-ideality was neglected in section 2.5, $y_S = 1$. Clearly, this is not a good approximation for $MgCl_2$. Finally, the salt diffusion coefficient was also assumed to be constant so that C_S is a linear function of position. This assumption is based on the salt diffusion coefficient being a constant independent of salt concentration. All these approximations are removed in the following discussion.

As in section 2.5, we consider the hypothetical case of diffusion occurring inside a capillary tube of length, l, located along the x axis. The two tube extremities are connected with two large salt-water reservoirs at different salt concentrations: $C_S = C_S^{(L)}$ and $C_S = C_S^{(R)}$ at $x = 0$ and $x = l$, respectively. A protein-salt-water mixture is located inside this tube. To impede protein transport into the reservoirs, semipermeable membranes close the two tube extremities. A schematic

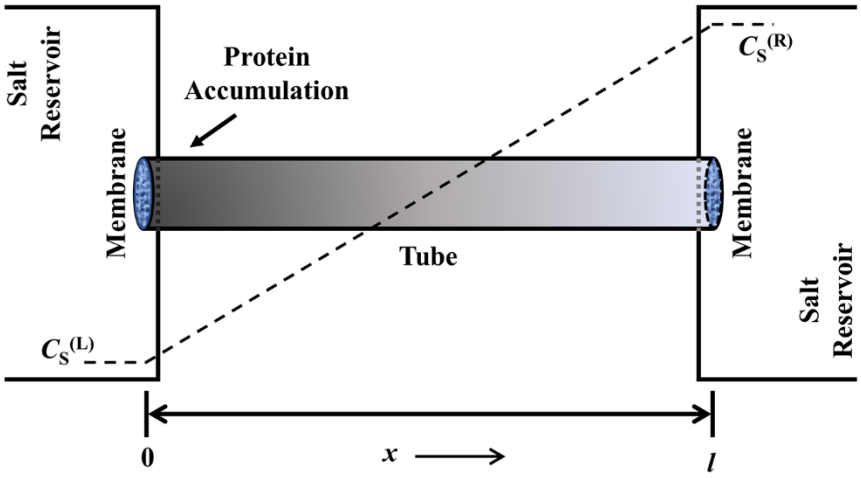

Figure 5.1 Schematic representation showing a tube of length, l containing a protein solution, located along the x-axis and connected to two salt reservoirs with salt concentrations, $C_S^{(L)}$ and $C_S^{(R)}$, through two semipermeable membranes. The corresponding salt concentration profile in steady-state conditions is described as a dashed line with positive slope.

diagram showing the capillary tube between the two large salt-water reservoirs is illustrated in Fig. 5.1. Salt-water reservoirs create a steady-state salt concentration gradient along the tube. If we set $C_S^{(R)} > C_S^{(L)}$, C_S increases from $x = 0$ to $x = l$, approximately in a linear fashion. We specifically choose $C_S^{(L)}$ = 0.093 M and $C_S^{(R)}$ = 2.0 M, to match the experimental range of diffusiophoresis data in Fig. 4.1 of previous chapter for the $MgCl_2$ case.

We assume that Brownian diffusion and diffusiophoresis are the only two processes responsible for protein transport within the tube. If an initially uniform lysozyme solution of concentration, C_P^0, is inserted in the tube, the salt concentration gradient will induce a *non-uniform* protein concentration, $C_P(x)$, in steady-state conditions due to diffusiophoresis. Specifically, protein migration occurs along the negative direction of the x axis if $\hat{D}_{PS} > 0$ and $C_S^{(R)} > C_S^{(L)}$. Since protein is confined inside the tube, protein flux must be zero in steady-state conditions. This leads to an accumulation of protein inside the tube at $x = 0$. To determine $C_P(x)$, we rewrite Eq.

2.24 (Chapter 2) to steady-state conditions. Specifically, we first rewrite Eq. 2.24 for our protein-salt system:

$$-\frac{v_P}{D_P^0} = \frac{d\ln C_P}{dx} + \hat{D}_{PS}\frac{v_S y_S}{C_S}\frac{dC_S}{dx} \tag{5.1}$$

and then rearrange in the following way:

$$\frac{d\ln \hat{C}_P}{dC_S} = -\hat{D}_{PS}\frac{v_S y_S}{C_S} + \frac{v_P}{D_P^0}\frac{dx}{dC_S} \tag{5.2}$$

where $\hat{C}_P \equiv C_P / C_P^0$ is the normalized protein concentration. Since protein is confined inside the tube, the protein flux must be zero in steady-state conditions in the volume-fixed reference frame. Correspondingly, we have from Eq. 2.23: $v_P = -\bar{V}_S D_S (dC_S / dx)$ because v_P and $\hat{D}_{PS}$ are defined with respect to the solvent-fixed reference frame, and $\bar{V}_S(C_S)$ and $D_S(C_S)$ are the partial molar volume and solvent-fixed diffusion coefficient of the salt component in the binary salt-water mixtures, respectively. This represents a small residual value of v_P taking into account water flux from low to high salt concentration. Therefore Eq. 5.2 can be rewritten in the following way:

$$\frac{d\ln \hat{C}_P}{dC_S} = -\left(\hat{D}_{PS}\frac{v_S y_S}{C_S} - \frac{\bar{V}_S D_S}{D_P^0}\right) = -w \tag{5.3}$$

Equation 5.3 represents a generalization of $w = v_S \hat{D}_{PS} / C_S$ introduced in Chapter 2 (see Eq. 2.28). The behavior of $\hat{D}_{PS}(C_S)$ was previously discussed (see Fig. 4.1). We now discuss the behavior of other terms in Eq. 5.3. In Fig. 5.2, $MgCl_2$ thermodynamic factor (y_S) is plotted as a function of salt concentration (C_S). Note that y_S significantly increases as salt concentration increases and

strong deviations from thermodynamic ideality (y_S different from 1) can be noticed. Therefore, y_S cannot not be assumed to be equal to 1 as was done in section 2.5.

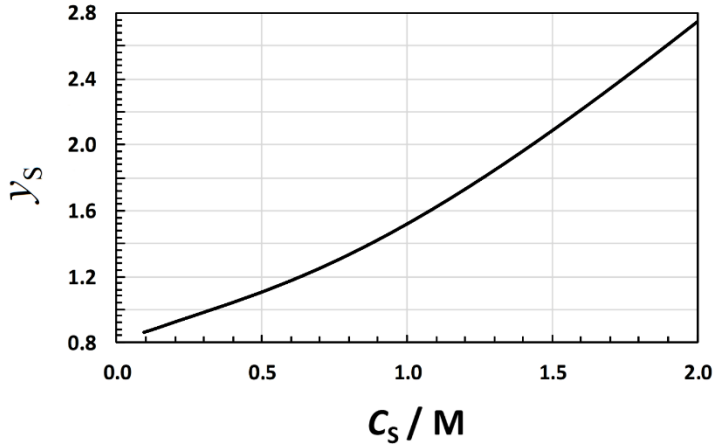

Figure 5.2 Thermodynamic factor of $MgCl_2$ as a function of its concentration. The value of y_S shows significant deviation from 1 at higher salt concentration.

It is now shown that $\bar{V}_S D_S / D_P^0$ in Eq. 5.3 is small. This contribution represents a small correction to convert protein diffusiophoresis from solvent-fixed to device reference frame.[127, 136] We calculated this term using the values of $\bar{V}_S$ and $D_S(C_S)$ of table 4.1 of Chapter 4. To determine lysozyme tracer-diffusion coefficient $D_P^0(C_S)$, we used $D_P^0(C_S) = D_P^0(0)/\eta_{r,S}(C_S)$, where $\eta_{r,S}(C_S)$ is relative viscosity also reported in table 4.1 and $D_P^0(0) = 0.132\times10^{-9}\,m^2\cdot s^{-1}$.[137] Figure 5.3(A) illustrates that the second term in bracket of Eq. 5.3, $\bar{V}_S D_S / D_P^0$ is small compared to the first term.

The behavior of $w(C_S)$ for lysozyme in the presence of $MgCl_2$ is shown in Fig 5.3(B). Here, we can see that $w(C_S)$ decreases as C_S increases to ≈ 0.7 M where a minimum occurs and then increases with salt concentration. The relatively very large values of w at low salt concentrations are related to protein charge. On the other hand, the increase in the values of w at high salt concentration are attributed to the salt thermodynamic non-ideality. This plot

demonstrates that $w(C_S)$ is not constant (as assumed for neutral molecule in section 2.5) and varies with salt concentration. The lower values of $w(C_S)$ obtained in the NaCl and KCl cases are included for comparison.

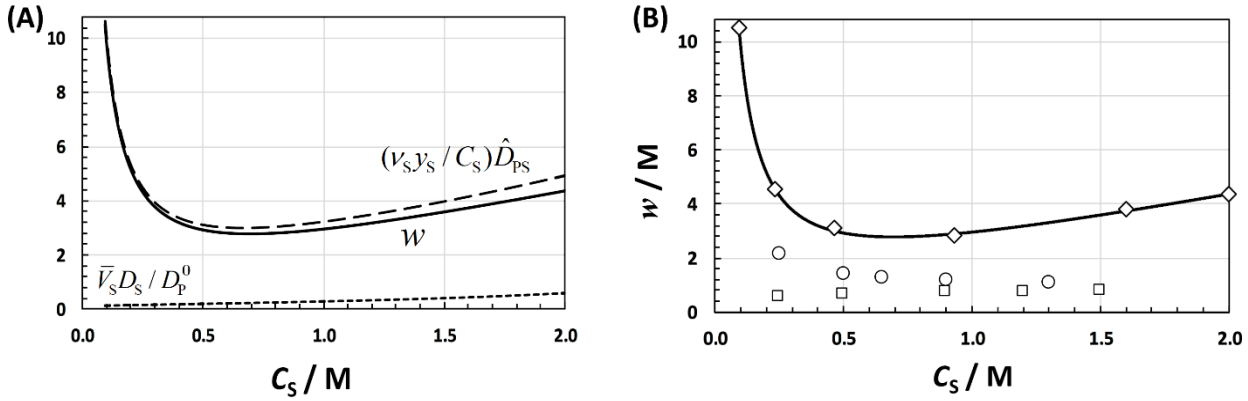

Figure 5.3 (A) Comparison of w with its two contributions, $\hat{D}_{PS}(\nu_S y_S)/C_S$ and $\bar{V}_S D_S / D_P^0$ (Eq. 5.3) as a function of C_S. (B) Values of *w* as a function of C_S for the $MgCl_2$ (diamonds) case. The solid curve is a fit through the data based on the empirical function: 1.0316 C_S^{-1} - 0.38016 $C_S^{-0.5}$ + 0.48772 + 1.8151 C_S . For comparison, values of *w* for the NaCl (circles) and KCl (squares) cases are included.

5.2 Determination of Protein Concentration Profile

To get the concentration profile of protein in the tube of Fig. 5.1, we need to integrate Eq. 5.3 with the condition that $w(C_S)$ is not a constant. Indefinite integration of Eq. 5.3 formally yields:

$$\hat{C}_P = c\ \exp(-\tilde{w}) \tag{5.4}$$

where *c* is an integration constant to be determined and we have introduced the integral function $\tilde{w}(C_S)$ by

$$\tilde{w} \equiv \int_{C_S^{(L)}}^{C_S} w(C_S')\, dC_S' \tag{5.5}$$

This function can be numerically evaluated. The corresponding plot is shown in Fig. 5.5(A). Note that $\tilde{w}(C_S^{(L)}) = 0$ since integration starts at $C_S = C_S^{(L)}$. Constant *c* can be determined by applying mass conservation to protein components:

$$\int_0^1 \hat{C}_P d\hat{x} = \frac{1}{C_S^{(R)} - C_S^{(L)}} \int_{C_S^{(L)}}^{C_S} \hat{C}_P \beta dC_S' = 1 \tag{5.6}$$

where $\hat{x} \equiv x/l$ is normalized position and $\beta \equiv (d\hat{x}/dC_S)(C_S^{(R)} - C_S^{(L)})$ is a unitless concentration-dependent coefficient linking C_S to $\hat{x}$. It describes the deviations of salt concentration profile $C_S(x)$ from linearity with $\beta = 1$. In Chapter 4 we assumed that $\beta = 1$. After inserting Eq. 5.4 into Eq. 5.6, we obtain:

$$c = \frac{C_S^{(R)} - C_S^{(L)}}{\int_{C_S^{(L)}}^{C_S} \exp(-\tilde{w}) \beta dC_S'} \tag{5.7}$$

The expression of $\beta(C_S)$ can be identified using Fick's law for salt diffusion flux J_S:

$$J_S = -[(1 - C_S \bar{V}_S) D_S] \frac{dC_S}{dx} \tag{5.8}$$

where $D_S(C_S)$ is the available $MgCl_2$ diffusion coefficient in the solvent-fixed reference frame (Table 4.1) and $(1 - C_S \bar{V}_S) D_S$ is the corresponding diffusion coefficient in the volume-fixed reference frame. If $(1 - C_S \bar{V}_S) D_S$ is assumed to be a constant then dC_S/dx is a constant because J_S is a constant in steady-state conditions. This leads to $\beta = 1$. Figure 5.4 shows the salt diffusion coefficient (D_S, solvent-fixed frame; $D_S(1 - C_S \bar{V}_S)$, volume-fixed frame) plotted as a function of salt concentration. Here we can see that salt diffusion coefficient is not a constant but moderately

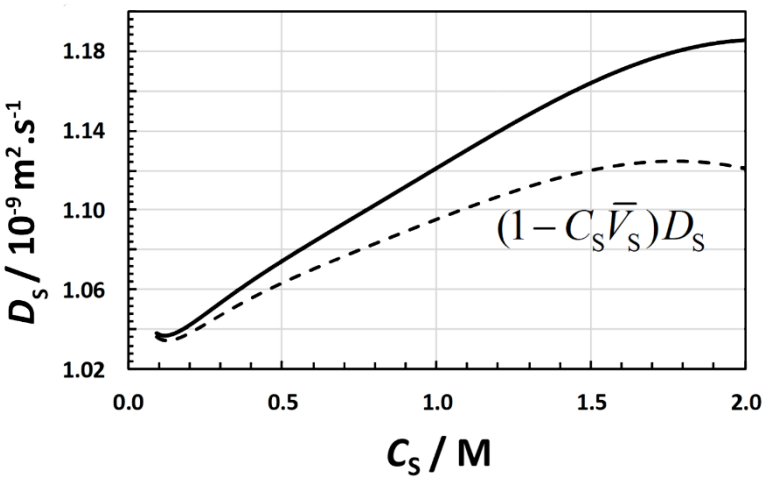

Figure 5.4 Diffusion coefficient, D_S, as a function of C_S for $MgCl_2$ case. For comparison the factor in square brackets of Eq. 5.8 is included (dashed curve).

increases with salt concentration. To assess its effect on β, we apply steady-state condition (constant flux J_S) to Eq. 5.8. This yields:

$$J_S = -\frac{\int_{C_S^{(L)}}^{C_S^{(R)}} (1-C_S'\bar{V}_S)D_S dC_S'}{l} \tag{5.9}$$

We then equate Eq. 5.8 and Eq. 5.9:

$$\frac{d\hat{x}}{dC_S} = \frac{(1-C_S\bar{V}_S)D_S}{\int_{C_S^{(L)}}^{C_S^{(R)}} (1-C_S'\bar{V}_S)D_S dC_S'} \tag{5.10}$$

Since $\beta \equiv (d\hat{x}/dC_S)(C_S^{(R)} - C_S^{(L)})$, we conclude that

$$\beta = \frac{(C_S^{(R)} - C_S^{(L)})(1-C_S\bar{V}_S)D_S}{\int_{C_S^{(L)}}^{C_S^{(R)}} (1-C_S'\bar{V}_S)D_S dC_S'} \tag{5.11}$$

The definite integral in Eq. 5.11 can be evaluated numerically. We can then determine the plot of $\beta(C_S)$ shown in Fig. 5.5. We can see that deviations of $\beta(C_S)$ from $\beta = 1$ remain small (less than

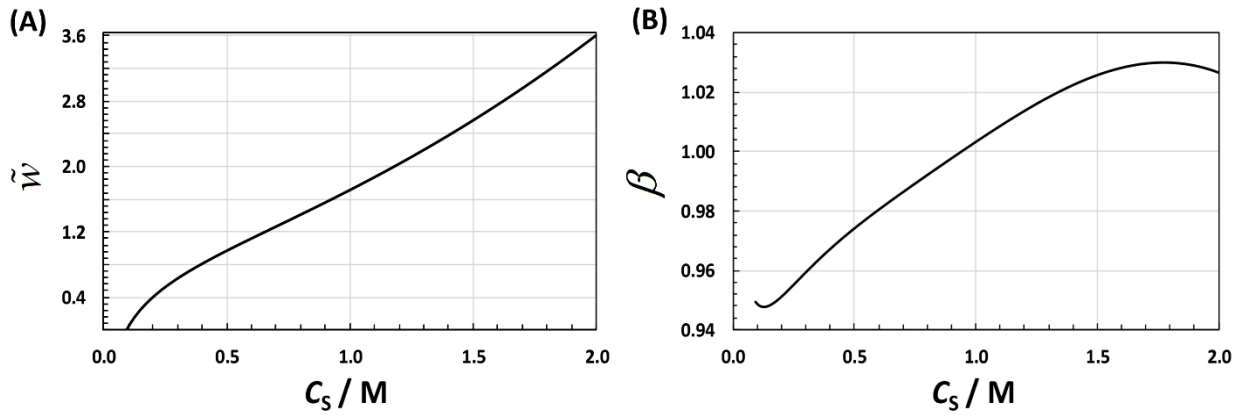

Figure 5.5 (A) Integral function, $\tilde{w}$, as a function of C_S (B) Coefficient, β, as a function of C_S.

about 5%). We can then conclude that dC_S / dx is approximately a constant and assuming that C_S is a linear function of *x* is a reasonable approximation. We are now in position to evaluate $\hat{C}_P(C_S)$. After inserting Eq. 5.7 into Eq. 5.4, we obtain:

$$\hat{C}_P = \frac{(C_S^{(R)} - C_S^{(L)})\exp(-\tilde{w})}{\int_{C_S^{(L)}}^{C_S^{(R)}} \exp(-\tilde{w})\beta dC_S'} \tag{5.12}$$

The behavior of $\hat{C}_P$ as a function of C_S is shown in Fig 5.6.

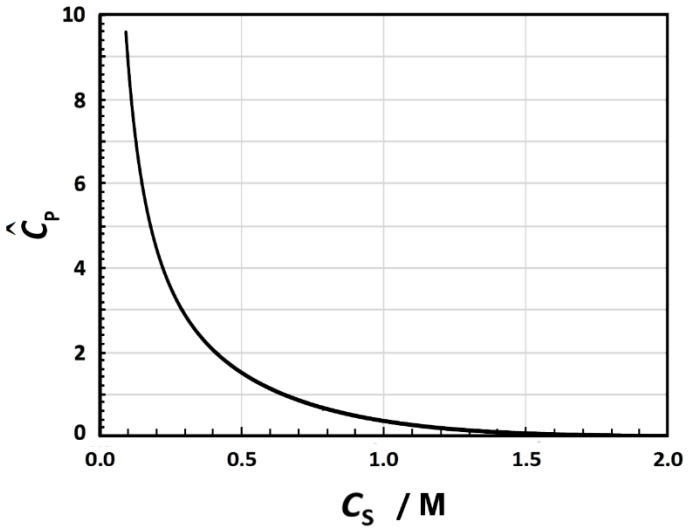

Figure 5.6 Normalized protein concentration profile, $\hat{C}_P$, as a function of salt concentration, C_S inside the tube.

Correspondingly, $\hat{x}(C_S)$ can be obtained by numerical integration of $d\hat{x}/dC_S \equiv \beta/(C_S^{(R)} - C_S^{(L)})$:

$$\hat{x} = \frac{\int_{C_S^{(L)}}^{C_S} \beta \, dC_S'}{C_S^{(R)} - C_S^{(L)}} \tag{5.13}$$

The dependence of C_S on the position x, which is extracted from Eq. 5.13, is shown in Fig. 5.7. Here we can appreciate that C_S is approximately a linear function of *x*.

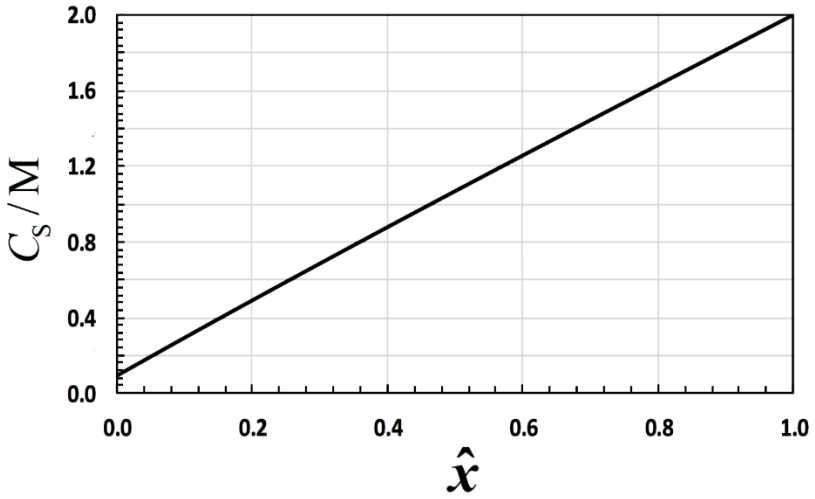

Figure 5.7 Salt concentration profile, C_S, as a function of normalized position, $\hat{x} \equiv x/l$.

Finally, combination of $\hat{C}_P(C_S)$ and $C_S(x)$ leads to $\hat{C}_P(x)$ shown in Fig. 5.8(A). Figure 5.8(B) shows the corresponding logarithmic plot where we see significant deviation from linearity This concentration profile reveals a 10-fold enhancement in C_P near the 0.093-M salt reservoir ($x \approx 0$) and a 100-fold depletion near the 2.0-M salt reservoir ($x \approx l$) due to the diffusiophoresis. It is important to remember that in the simplified mass transfer model discussed in section 2.5, the expected concentration profile of macromolecule is a linear function of position. In Fig. 5.8(B) we

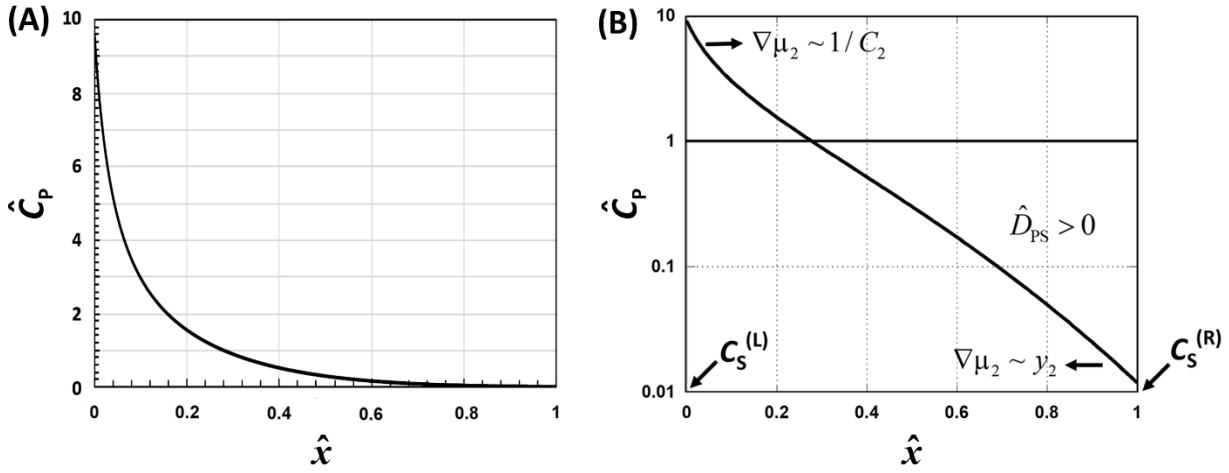

Figure 5.8 (A) Normalized protein concentration, $\hat{C}_P = C_P / C_P^0$ profile as a function of $\hat{x}$. (B) Logarithmic diagram showing the steady-state normalized profile of lysozyme concentration, $\hat{C}_P = C_P / C_P^0$, along the x axis obtained in the presence of a $MgCl_2$ gradient with $C_S^{(L)}$ = 0.093 M and $C_S^{(R)}$ = 2.0 M.

can see that $\ln\hat{C}_P$ exhibits an inflection point at $x/l \approx 0.3$, with $\ln\hat{C}_P$ curving upward and downward towards the left and right reservoirs, respectively. This behavior is related to the $w(C_S)$ minimum around the salt concentration of ≈ 0.7 M (see Fig 5.3B). In other words, protein charge is responsible for amplifying the increase in protein concentration at low salt concentration ($x \approx 0$), while salt thermodynamic non-ideality ($y_S > 1$) is responsible for a more effective decline in protein concentration at high salt concentration ($x \approx l$). This behavior was not grasped by the basic model discussed in Chapter 2. All these features related to $MgCl_2$-induced protein diffusiophoresis are appealing for protein manipulation in solution (e.g. using microfluidic technologies) with applications to protein concentration and purification.

Chapter 6

Quantitative Theoretical Examination of Lysozyme Diffusiophoresis

6.1 Theoretical Examination of Diffusiophoresis Coefficients

In this chapter, we theoretically examine the effect of salt type on the experimental behavior of $\hat{D}_{\mathrm{PS}}(C_{\mathrm{S}})$ shown in Fig. 4.1 of Chapter 4. Typically, an electrophoresis model is employed to describe salt-induced diffusiophoresis of charged particles.[36, 38, 149] The connection of diffusiophoresis with electrophoresis stems from salt concentration gradients being able to create an internal electric field, directly proportional to the difference between the mobilities of the two salt ions as described in section 4.2 of Chapter 4. For protein diffusiophoresis in the presence of symmetric electrolytes such as NaCl and KCl ($\nu_{\mathrm{S}} = 2$), we have:[36]

$$\hat{D}_{\mathrm{PS}}^{(\mathrm{e})} = \frac{\sigma Z_{\mathrm{P}}}{2}(\tau_{\mathrm{C}} - \tau_{\mathrm{M}}) \tag{6.1}$$

where the superscript "(e)" is appended to $\hat{D}_{\mathrm{PS}}$ to indicate that this expression of diffusiophoresis takes into account the electrophoretic mechanism only, and ignores diffusiophoresis contributions such as those related to specific protein-salt interactions (e.g. protein preferential hydration), which are expected to dominate at high salt concentrations.[36, 41] In Eq. 6.1, τ_i is a transference number and represents the fraction of charge transported by ion "*i*".[150] In the limit of infinite dilute solution, the τ_i of an ion with ionic concentration C_i and ionic charge Z_i is the arithmetic average of the

ion trace-diffusion coefficient D_i, that is $\tau_i = C_i Z_i^2 D_i / \sum_k C_k Z_k^2 D_k$ where k is the individual component of the electrolyte. For NaCl and KCl we have, $\tau_C = D_C / (D_C + D_M)$ and $\tau_M = D_M / (D_C + D_M)$, whereas for $MgCl_2$, $\tau_C = D_C / (D_C + 2D_M)$ and $\tau_M = 2D_M / (D_C + 2D_M)$ with τ_C and τ_M ($\tau_C + \tau_M = 1$) being the transference numbers of chloride (C) and metal ion (M), respectively. The term $\tau_C - \tau_M$ in Eq. 6.1 characterizes the strength of the internal electric field. Transference numbers are preferred to ionic mobilities in order to extend the validity of the internal electric field factor in Eq. 6.1 beyond the limit of $C_S \to 0$. Experimental values of transference numbers have been reported for many aqueous salts as a function of C_S at 25 °C.[53, 55, 146] These values are reported in table 6.1 for NaCl and KCl while table 6.2 presents the values form $MgCl_2$ at different experimental salt concentrations.

Table 6.1 Experimental transference numbers of chloride (C) and metal ion (M), respectively for NaCl and KCl at different concentrations of salt.

Salt	C_S / M	τ_C	$\tau_C - \tau_M$
KCl	0.250	0.511	0.021
	0.500	0.511	0.023
	0.900	0.512	0.024
	1.200	0.512	0.024
	1.500	0.513	0.025
NaCl	0.250	0.620	0.240
	0.500	0.625	0.250
	0.650	0.627	0.255
	0.900	0.631	0.261
	1.300	0.634	0.268

Table 6.2 Experimental transference numbers of chloride (C) and metal ion (M), respectively for $MgCl_2$ at different concentrations of salt.

C_S / M	τ_C	$\tau_C - \tau_M / 2$
0.093	0.638	0.457
0.233	0.656	0.484
0.464	0.675	0.513
0.930	0.703	0.555
1.599	0.735	0.603
2.000	0.752	0.628

In Eq. 6.1, σ is an electrokinetic factor with $\sigma = 1$ when $C_S \to 0$, and Z_P is the protein charge at its slip boundary, thereby taking into account the contribution of small ions located within the hydrodynamic volume of the diffusing particle. In the limit of $C_S \to 0$, $\hat{D}_{PS}^{(e)} \to (Z_P / 2)(\tau_C - \tau_M)$ represents the Nernst-Hartley equation,[36] which shows that the intercept of $\hat{D}_{PS}(C_S)$ in the presence of a given salt is directly proportional to protein charge. For lysozyme at pH 4.5, salt-osmotic diffusion data[36, 51, 142] indicate that the Donnan charge is 8 ± 1 at pH 4.5. This value, which accounts for the binding of 2-3 chloride counterions to lysozyme, can be taken as Z_P. For the electrokinetic factor, σ, we may write:[36]

$$\sigma = \frac{h}{1 + \kappa R_P} \tag{6.2}$$

where R_P is the protein hydrodynamic radius (radius at the slip boundary) with $R_P = 1.863$ nm for lysozyme,[137] $\kappa \equiv (8000 \pi N_A \lambda_B I)^{1/2}$ is the Debye constant,[151] with I being the salt ionic strength, N_A the Avogadro's number and λ_B the Bjerrum length (0.7151nm for water at 25 ºC), and h is

a corrective coefficient. In Eq. 6.2, $(1+\kappa R_{\mathrm{P}})^{-1}$ is the dominant factor describing the electrophoretic effect exerted by a spherically symmetric ion cloud, making σ to sharply decrease as ionic strength increases. Values of $\sigma \approx 0.2$ correspond to our experimental salt concentration range. For spherical particles, h may be described by the Henry's function:[152, 153]

$$h(\kappa R_{\mathrm{P}}) = 1.5 - e^{\kappa R_{\mathrm{P}}}\,[7.5\,E_7(\kappa R_{\mathrm{P}}) - 3E_5(\kappa R_{\mathrm{P}})] \tag{6.3}$$

with $E_n(x) \equiv \int_1^{\infty} t^{-n} e^{-xt}\,dt$, which takes into account particle curvature. Note that $h(0) = 1$ (Debye-Huckel limit) and $h(\kappa R_{\mathrm{P}})$ moderately increases with salt ionic strength up to $h(\infty) = 1.5$ (Smoluckowski limit).[53] It is important to observe that this description of σ is expected to be accurate only at relatively low ionic strengths. As salt concentration increases, the accuracy of Eq. 6.2 becomes less important because σ dependence on salt concentrations becomes relatively weak and non-electrophoretic contributions dominate the behavior of $\hat{D}_{\mathrm{PS}}(C_{\mathrm{S}})$.

The three salt cases considered in this work are particularly interesting for understanding how a significant change in the magnitude of $\tau_{\mathrm{C}} - \tau_{\mathrm{M}}$ impacts protein diffusiophoresis. In the KCl case, $\tau_{\mathrm{C}} - \tau_{\mathrm{M}} \approx 0.02$ [55] is very small and the role of the electrophoretic mechanism discussed above is marginal. Thus, this salt case represents a sort of baseline for understanding salt-induced protein diffusiophoresis. For NaCl, its value of $\tau_{\mathrm{C}} - \tau_{\mathrm{M}} \approx 0.25$ [55] implies that there is a much more contributing electrophoretic mechanism. Finally, the $MgCl_2$ case represents a further step up in complexity due a relatively large electrophoretic contribution and the divalent nature of this salt, which also requires modification of Eq. 6.1.

In the KCl case, we use Eq. 6.1 and Eq. 6.2 with $Z_{\mathrm{P}} = 8$ and available transference numbers[55] to calculate $\hat{D}_{\mathrm{PS}}^{(\mathrm{e})}(C_{\mathrm{S}})$ and subtract its small contribution to the experimental values of $\hat{D}_{\mathrm{PS}}(C_{\mathrm{S}})$.

We remark that an accurate description of $\hat{D}_{PS}^{(e)}(C_S)$ is not crucial in this case due to its marginal impact on $\hat{D}_{PS}(C_S)$. In Fig. 6.1, $\hat{D}_{PS}(C_S)$ and the residual diffusiophoresis, $\hat{D}_{PS}^{(r)} \equiv \hat{D}_{PS} - \hat{D}_{PS}^{(e)}$, are plotted as function of C_S for KCl. Note that $\hat{D}_{PS}^{(r)}$ is slightly lower than $\hat{D}_{PS}$ due to the small positive contribution of $\hat{D}_{PS}^{(e)}$. Since $\hat{D}_{PS}^{(r)}$ linearly increases with C_S, we fit these data to the linear equation $\hat{D}_{PS}^{(r)} = c + bV_W C_S$, where c and b are two unitless parameters to be determined and the molar volume of water $V_W = 18.07\,\mathrm{cm}^3 \cdot \mathrm{mol}^{-1}$ is included so that b may be approximately interpreted as the excess of water molecules outside the slip boundary of the diffusing protein, driving diffusiophoresis by preferential hydration.[127] We find: $c = -0.07 \pm 0.01$ and $b = 37 \pm 1$. We

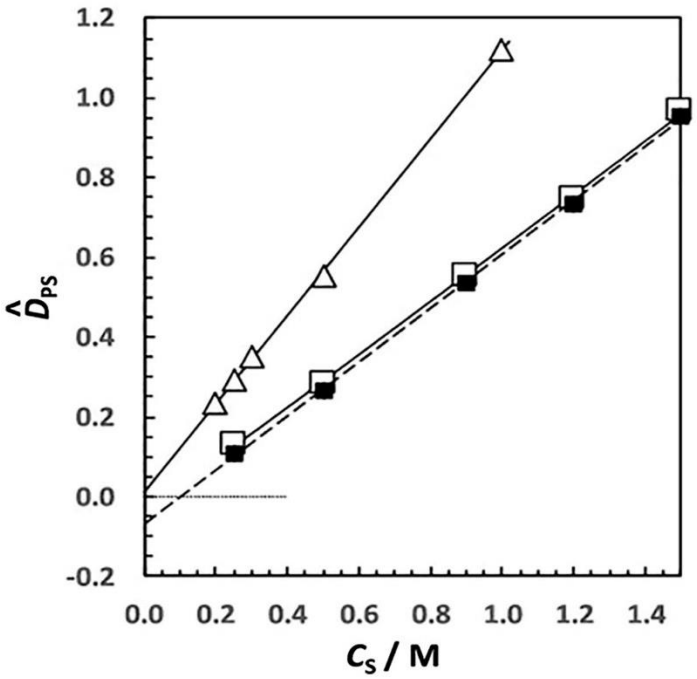

Figure 6.1 Lysozyme diffusiophoresis coefficient (open squares) and residual diffusiophoresis coefficient (solid squares) as a function of KCl concentration. PEG diffusiophoresis coefficient (open triangles, normalized to $D_p(0) = 0.132\times10^{-9}$ $m^2 \cdot s^{-1}$) as a function of KCl concentration is included for comparison. The dotted horizontal line indicates the position of zero intercept. The solid and dashed curves are fits through the data described in the main text.

note that ignoring the small contribution of $\hat{D}_{PS}^{(e)}(C_S)$ altogether would still yield an appreciable negative intercept ($c = -0.04 \pm 0.01$).

Residual diffusiophoresis of a charged particle can be compared to diffusiophoresis of a neutral particle, for which it is expected that $\hat{D}_{PS}$ vanishes when $C_S \to 0$. This is illustrated in Fig. 6.1, where the experimental behavior of KCl-induced diffusiophoresis of polyethylene glycol (PEG) is included for comparison.[41] The small negative intercept found in the lysozyme case may be attributed to chemiphoresis,[29] the mechanism responsible for negative diffusiophoresis due to the reduction of the thickness of electrical double layer (κ^{-1}) along a salt concentration gradient. Specifically, the thickness of the double layer decreases as salt ionic strength increases. This reduction implies a lower electrostatic energy. Thus, particle motion occurs towards lower electrostatic energy and consequently higher salt concentration.[154] This suggests that chemiphoresis prevails on electrophoresis in the KCl case within the experimental salt concentration range. The small contribution of chemiphoresis is expected to approach zero in the limit of both low and high ionic strength, with a shallow maximum contribution at an intermediate salt concentrations.[29, 36] It is therefore reasonable to assume that, within the experimental error, its contribution is a constant in the explored salt concentration range. Finally, the positive value of b is consistent with protein preferential hydration driving protein diffusiophoresis toward a salt-depleted environment.[41]

We now turn our attention to the NaCl case. Here, we fit diffusiophoresis data to the equation: $\hat{D}_{PS} = \hat{D}_{PS}^{(e)} + c + bV_W C_S$ with $\hat{D}_{PS}^{(e)}$ given by Eq. 6.1 and Eq. 6.2 and use available transference numbers.[53] Due to the large contribution of $\hat{D}_{PS}^{(e)}$, we now assume that $c = -0.07$ is the same as for KCl, and determine Z_P and b. Our analysis is illustrated in Fig. 6.2. We find:

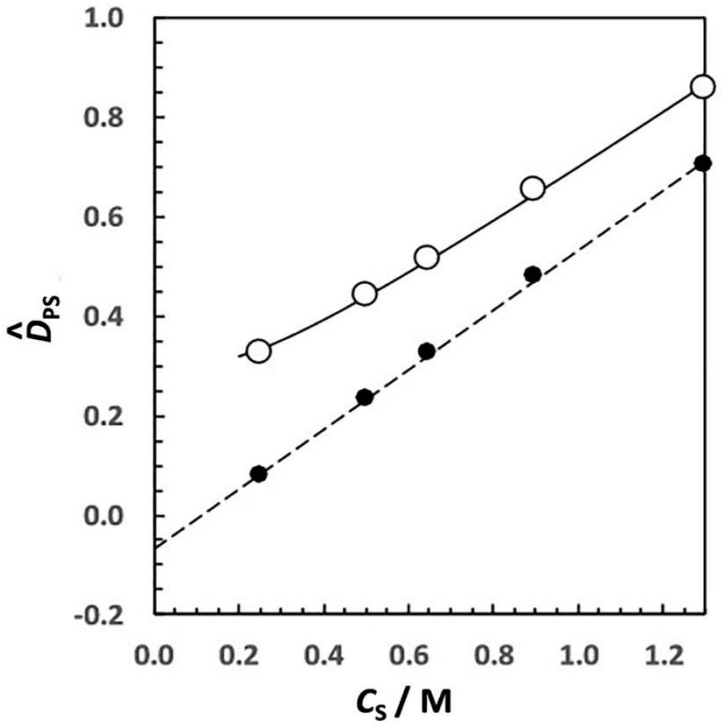

Figure 6.2 Lysozyme diffusiophoresis coefficient (open circles) and residual diffusiophoresis coefficient (solid circles) as a function of NaCl concentration. The solid and dashed curves are fits through the data described in the main text.

$Z_P = 7.7 \pm 0.7$ and $b = 33 \pm 1$. The extracted value of Z_P matches the Donnan charge of 8 ± 1 while the value of b is comparable with that obtained in the KCl case. The corresponding residual diffusiophoresis plot is shown in Fig. 6.2.

We finally consider the $MgCl_2$ case. Due to the divalent nature of the metal ion ($\nu_S = 3$), Eq. 6.1 changes to[36, 41]

$$\hat{D}_{PS}^{(e)} = \frac{\sigma Z_P}{3}\left(\tau_C - \frac{\tau_M}{2}\right) \tag{6.4}$$

Available transference numbers[56] allow us to assess that the electrophoretic mechanism is significant with $\tau_C - \tau_M / 2$ increasing from 0.46 to 0.63 as C_S increases from 0.093 M to 2.0 M. In relation to σ in Eq. 6.2, it is important to note that Henry's function is expected to be more

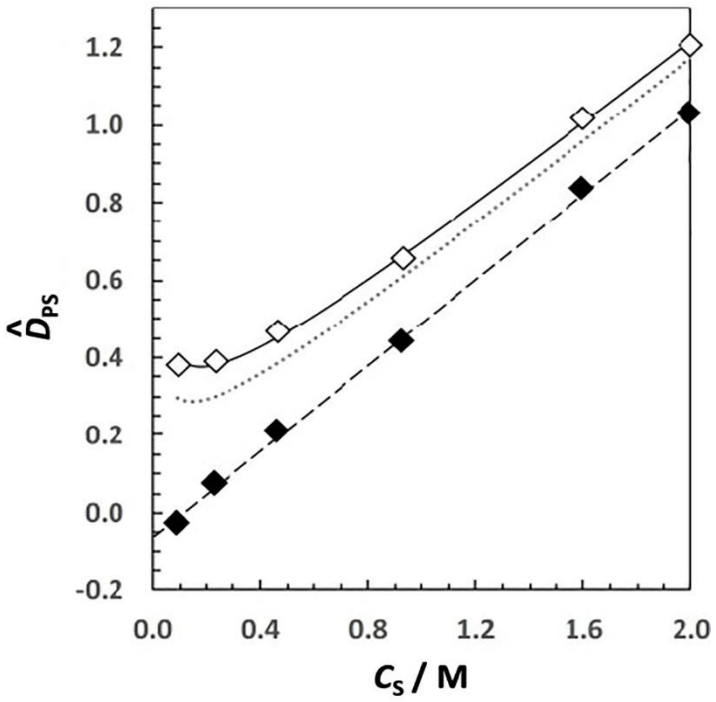

Figure 6.3 Lysozyme diffusiophoresis coefficient (open diamonds) and residual diffusiophoresis coefficient (solid diamonds) as a function of $MgCl_2$ concentration. The dotted curve represents diffusiophoresis coefficients calculated using Z_P = 7.7. The solid and dashed curves are fits through the data described in the main text.

accurate for symmetric electrolytes but can be still considered as an acceptable approximation for asymmetric electrolytes. After setting $c = -0.07$ for the small chemiphoretic contribution, we find: $Z_P = 10.4 \pm 0.9$ and $b = 31 \pm 1$. Our analysis is illustrated in Fig. 6.3. Interestingly, the extracted value of b is the same as that extracted in the NaCl case within the experimental error, while the value of Z_P is 35% larger. This difference is noticeable as pointed out by the dashed curve in Fig. 6.3, which is constructed using $Z_P = 7.7$ (from NaCl-related analysis). The relatively large value of $Z_P = 10.4$ may be related to model approximations and/or an actual increase in protein charge within the experimental $MgCl_2$ concentration range. In either case, $MgCl_2$-induced diffusiophoresis is appreciably larger than predicted from theory. To appreciate its significance, we note that a re-examination of the mass-transfer problem discussed is Chapter 5 show that a

decrease in protein charge from 10.4 to 7.7 reduces protein accumulation at $x = 0$ by ≈30% and consequently also reduces protein depletion at $x = l$ by ≈30%. The effect of $MgCl_2$ on protein charge will be further discussed below by examining hydrogen-ion titrations in the presence of salts.

6.2 Hydrogen-ion Titrations

To examine the effect of salt on lysozyme charge, we performed hydrogen-ion titrations.[101, 104] Experimental details are provided in section 3.8. We specifically determined the excess of bound hydrogen ions per protein, ν_H, as a function of measured pH around pH 4.5 (see Eq. 3.2 of Chapter 3). Our results for lysozyme in aqueous KCl (Fig. 6.4) are in good agreement with the literature.[101] Note that ν_H becomes the same as Z_P in the absence of binding of salt ions. The behavior of ν_H

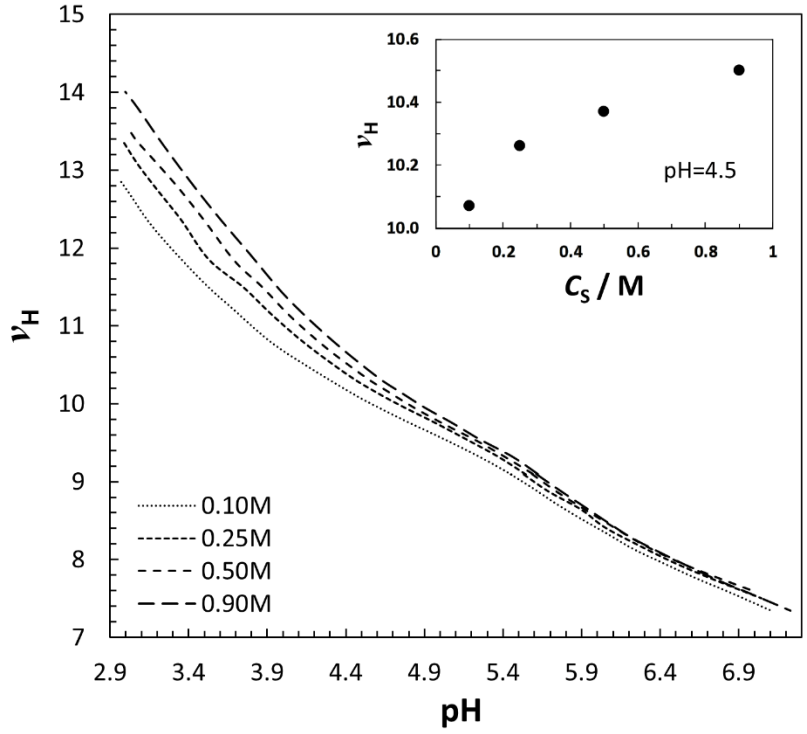

Figure 6.4 Excess number of bound protons per lysozyme, ν_H, as a function of pH in aqueous KCl at the listed concentrations. Curves interpolate experimental data points (not shown). The inset shows ν_H as a function of salt concentrations, C_S, at pH 4.5.

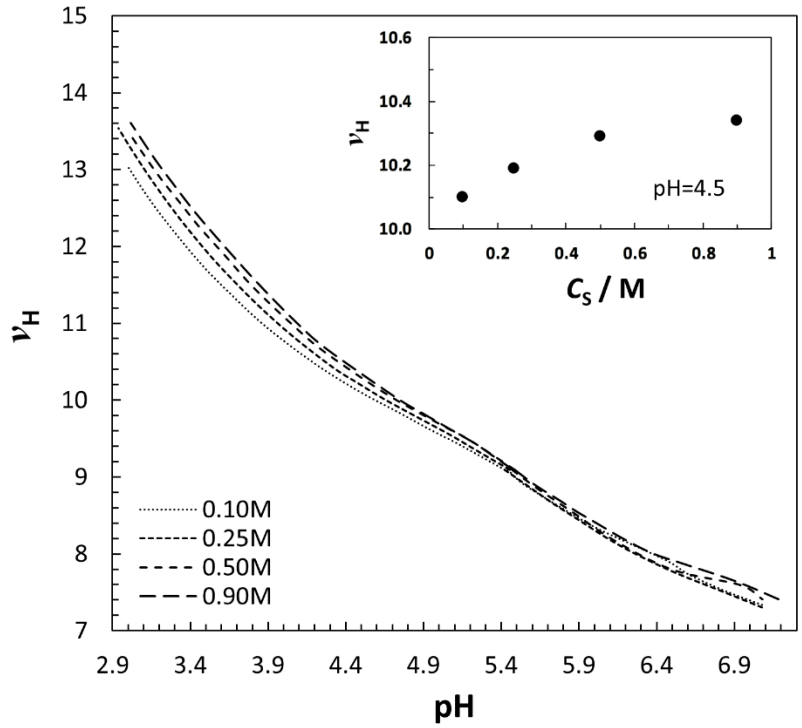

Figure 6.5 Excess number of bound protons per lysozyme, ν_H, as a function of pH in aqueous NaCl at the listed concentrations. The inset shows ν_H as a function of salt concentrations, C_S, at pH 4.5.

in the KCl and NaCl cases, which is illustrated in Figs. 6.4 and 6.5 shows that a minor increase in ν_H with salt concentration occurs at any measured pH. In contrast, ν_H was found to appreciably *decrease* as C_S increases in the $MgCl_2$ case as shown in Fig. 6.6. If ion binding is ignored, a decrease in ν_H due to $MgCl_2$ implies a corresponding decrease in protein charge, in disagreement with the hypothesized effect of this salt on Z_P. To reconcile the behaviors of ν_H and Z_P, a competitive binding of Mg^{2+} and H^+ toward the available $-COO^-$ sites on the protein surface may be considered. In the presence of $MgCl_2$, less carboxylate sites are available to bind protons thereby reducing the value of ν_H. At the same time, replacing H^+ with Mg^{2+} produces a net increase in protein charge due to the divalent nature of magnesium ions, qualitatively consistent with the interpretation of our diffusiophoresis results.

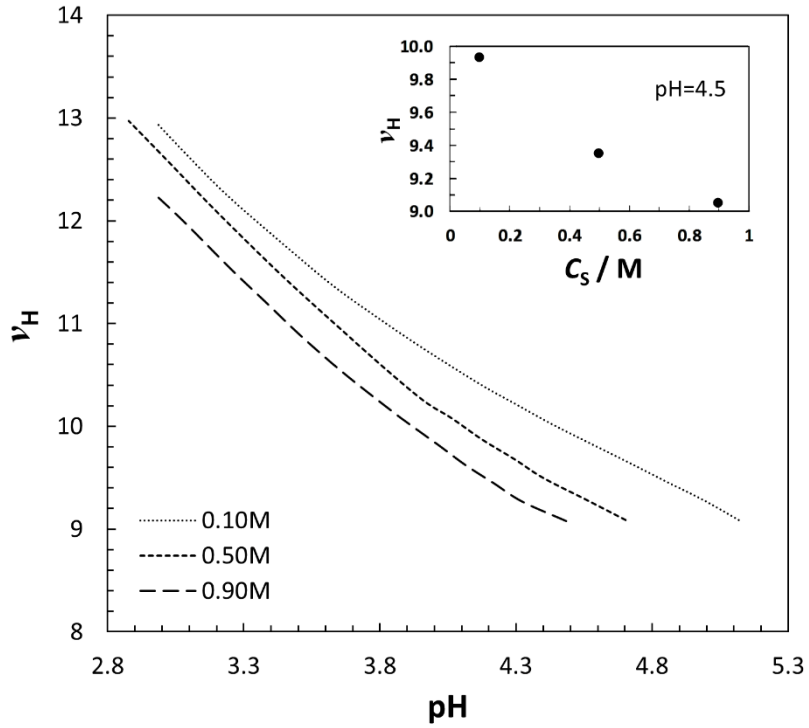

Figure 6.6 Excess number of bound protons per lysozyme, ν_H, as a function of pH in aqueous $MgCl_2$ at the listed concentrations. The inset shows ν_H as a function of salt concentrations, C_S, at pH 4.5.

6.3 Summary and Conclusions

Lysozyme diffusiophoresis coefficients, $\hat{D}_{PS}$, were found to be positive and increase with salt concentration in all three salt cases. At low salt concentrations, diffusiophoresis coefficients are consistent with the electrophoretic mechanism. Specifically, values of, $\hat{D}_{PS}$, were found to be the largest in the $MgCl_2$ case and close to zero in the KCl case, consistent with the known ranking in ion mobility. The three salt cases considered in this work allowed us to examine the contribution of chemiphoretic mechanism (KCl), electrophoretic mechanism (NaCl), and ion valence ($MgCl_2$) to diffusiophoresis. In the case of $MgCl_2$, lysozyme diffusiophoresis coefficients were found to be even larger than predicted. Effects of salt on hydrogen-ion titration curves are consistent with the

binding of Mg^{2+} ions to carboxylate groups of lysozyme. The corresponding increase in lysozyme charge can explain larger, $\hat{D}_{PS}$, values.

Theoretical examination of steady-state diffusiophoresis inside a capillary tube indicates that concentration gradients of $MgCl_2$ produce significant accumulation of lysozyme at one tube end (low salt concentration) due to protein charge and the relatively low mobility of Mg^{2+} ions compared to Cl^- ions. Correspondingly, a significant depletion of lysozyme is predicted at the other tube end (high salt concentration) due to a large salt thermodynamic factor. These findings suggest that $MgCl_2$ concentration gradients could be exploited for protein manipulation with applications relevant to microfluidic technologies and diffusion-based mass transfer in general.

PART II

Lysozyme Condensation in Aqueous Mixtures

Chapter 7

Theoretical Background on Phase Transitions of Protein Aqueous Mixtures

7.1 Introduction

Phase separation refers to the spontaneous partitioning of a system into multiple phases of distinct properties such as density, and concentration, *etc.* different from the initial phase.[155] Protein condensation refers to the formation of protein-rich phases, such as droplets, aggregates, crystals, and gels from the protein solutions.[67] Liquid-liquid phase separation (LLPS) represents the reversible formation of two separate coexisting liquid phases from an initially homogeneous solution of macromolecules (proteins, polymers) or colloidal particles (e.g. polymer nanoparticles), onset by the change in conditions such as temperature, additives, ionic strength, pH, etc.[156] One of the two coexisting liquid phases is diluted and other is concentrated in macromolecule. As discussed below, the diluted and concentrated phases can be formally treated as a gas and as a liquid, respectively. In this chapter, the fundamental principles of LLPS of the solutions of globular macromolecules are reviewed. We start with the qualitative examination of the phase behavior of these systems, focusing on protein phase diagram and then explain LLPS generated by decreasing temperature. We shall also describe the role of protein-protein and protein-salt interactions on their phase separation behaviours.

7.2 Phase Behavior of Globular Macromolecules

This section provides a qualitative description of the phase diagram of globular macromolecules. Figure 7.1 shows a representative schematic temperature-volume fraction (T-ϕ_1) phase diagram of binary macromolecular solutions. The volume fraction of the macromolecule is defined as $\phi_1 = n_1 V_1 / V$ where n_1 and V_1 are the number of moles and molar volume of the macromolecule, respectively, while V is the total volume of the system. It can be observed in Fig. 7.1, that the systems exhibit a broad region of liquid-solid coexistence.[157, 158] Interestingly, the liquid-liquid coexistence curve lies below the solid-liquid coexistence (solubility) curve and are metastable

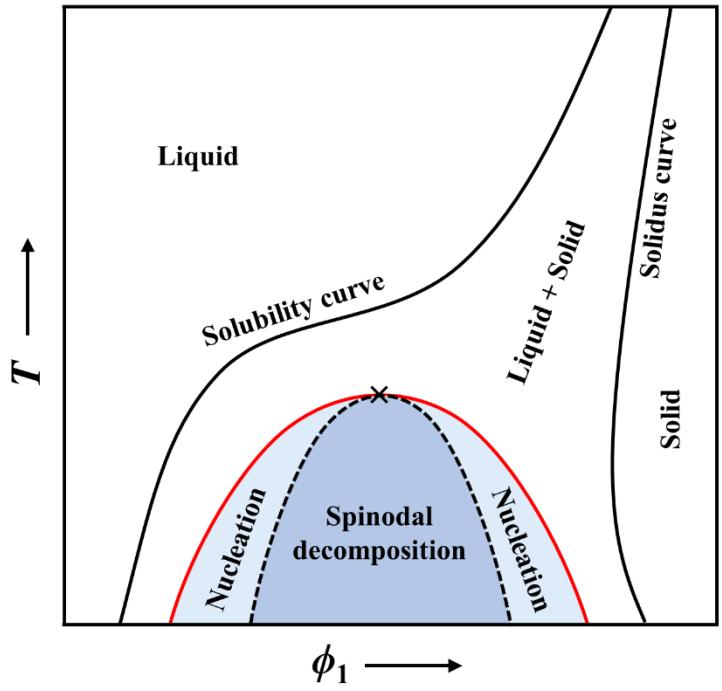

Figure 7.1 A representative phase diagram for a binary globular macromolecular solution. The region shown using the blue colors corresponds to the LLPS regions. The LLPS inside the dashed line region follows the spinodal decomposition while outside the dashed line LLPS occurs through nucleation and growth. Symbol "×" represents the maxima of curve, also known as critical point. The solubility and solidus curves represent the fraction of macromolecule in dissolved and in crystal state, respectively, at a given temperature.[157,158]

because the coexistence of two liquid phases occurs within the region of liquid-solid coexistence.[65, 158] Metastability can be defined as the existence of a given phase of a chemical substance for a transient time outside its domain of thermodynamic stability (e.g. homogeneous mixture phase) before evolving towards the thermodynamically stable phase (e.g. solid-phase). In the case of proteins, LLPS can be observed because crystallization is a relatively slow process. The metastability of protein LLPS has been linked to the short nature of protein-protein attractive interactions as it will be discussed later. In other words, two proteins can feel a reciprocal attraction only if they are close to each other. This is related to the fact that the typical range of van der Waals and other interactions is small compared to the characteristic size of proteins or other globular colloidal particles. It is important to remark that LLPS metastability has been also predicted to occur for large colloidal particles.[159] However, metastable LLPS is more difficult to observe in these cases because crystallization and precipitation are relatively fast. On the other hand, the condition of short-range interactions does not apply to linear polymers because the range of van der Waals and other interactions is comparable to the characteristic size of monomers.

The phase separation temperature, T_{ph}, in Fig. 7.1 is located on the binodal curve (solid red line) which establishes the boundary where two distinct phases co-exist in solution. Between the binodal and spinodal (dashed lines) curves lies a metastable region where liquid demixes via a nucleation process (droplet formation). The spinodal zone (areas delineated by dashed lines), is a subdomain within the demixing domain in which demixing does not occur by nucleation but by the so-called spinodal decomposition *i.e.,* worm-like bicontinuous network formation.[158, 160]

The metastable protein-rich phase can be an intermediate in the process of formation of the stable crystalline or even amorphous precipitates phases.[161, 162] The previous experimental and theoretical work has predicted that the metastability of the protein-rich liquid phase with respect

to the crystalline phase may provide a mechanism of the solution-to-crystals phase transition.[159, 163-167] According to this mechanism, the nucleation of the crystalline nuclei proceeds in two steps: formation of a protein-rich droplet due to the LLPS, and appearance of a crystalline nucleus within the droplet due to the ordering of a certain number of molecules.[65, 159, 168] The enhanced crystal-nucleation can be elaborated by using the ideas of nucleation theory.[169-171] According to this theory, the change in Gibbs free energy with the formation of a crystal from a droplet can be given as:[169-171]

$$\Delta G = \left(\frac{4}{3}\pi R^3\right)\frac{\Delta_{\text{crys}}G}{V_1} + (4\pi R^2)\gamma \tag{7.1}$$

where R is the radius of a crystal which is considered spherical for simplicity, $\Delta_{\text{crys}}G$ is the corresponding Gibbs free energy of crystallization, and γ is the surface tension between the crystal and surrounding medium in the protein-rich droplet. The first energy term on the right of Eq. 7.1 is denoted as a volume term that characterizes the thermodynamic saturation while the second term is denoted as a surface term.[171] The negative volume contribution is directly proportional to R^3 while the surface positive contribution is directly proportional to R^2. The contribution of the bulk term decreases as R increases because $\Delta_{\text{crys}}G$ is negative. On the other hand, the surface term increases with R because $\gamma > 0$.[169-171] As a net result, ΔG first increases as R increases and then displays a maximum (ΔG^*) before decreasing then becoming negative as R further increases. The maximum value of ΔG^* is known as the nucleation barrier and can be given as:

$$\Delta G^* = \frac{16\pi}{3}\frac{V_1^2\gamma^3}{\Delta_{\text{crys}}G^2} \tag{7.2}$$

Equation 7.2 shows that the nucleation barrier can be reduced by increasing $\left|\Delta_{\text{crys}}G\right|$, which describes supersaturation or decreasing γ.[172] In the phases separated by LLPS, the surface energy of the crystal in the protein-rich phase is smaller than the surface energy of crystal formed in the protein-poor phase because the protein-rich liquid phase has many protein molecules making multiple attractive interactions with the crystal. In other words, the better *wetting* of crystals in the protein-rich phase lowers the contribution of surface term, which leads towards enhanced crystal-nucleation as compared to in the protein-poor phase.

7.3 Thermodynamics of Globular Macromolecules

Generally, the processes of solution mixing and phases transitions are described in isothermal and isobaric conditions.[61, 173] Therefore, these processes can be described by using the variations of Gibbs free energy, *G*, as a function of the composition of the aqueous mixture.[174] For phase transition to be thermodynamically favored, it needs to result in a decrease in the mixture's Gibbs free energy.[174] However, the majority of the phase transitions in the aqueous solutions of macromolecules are associated with insignificant variations in the total volume of the systems.[61] Thus, these approximately isochoric processes can be equally described using the Helmholtz free energy, *A*, which for an open system can be presented as:[175]

$$dA = -SdT - pdV + \sum_i \mu_i dn_i \tag{7.3}$$

where μ_i is the chemical potential of the *i*th component of the system. For a specific binary macromolecule(1)-solvent(0) two-component system composed of n_1 moles of macromolecule and n_0 moles of solvent at constant temperature *T* and pressure *p*, Eq. 7.3 can be expanded as:[173]

$$dA = -pdV + \mu_1 dn_1 + \mu_0 dn_0 \tag{7.4}$$

where μ_1 and μ_0 is the chemical potential of macromolecule and solvent, respectively. If we assume that the molar volume of the macromolecule, V_1, is constant and independent of the composition and molar volume of the solvent, V_0 is also constant following the Gibbs-Duhem relation, then the total volume of the system will be invariant upon phase transition.[61, 173] The differential of the total volume of our open system at constant *T* and *p* can be written as:

$$dV = V_1 dn_1 + V_0 dn_0 \tag{7.5}$$

Substituting the value of dn_0 from Eq. 7.5 into Eq. 7.4 will give us:

$$dA = -\left(p - \frac{\mu_0}{V_0} \right) dV + \left(\mu_1 - \mu_0 \frac{V_1}{V_0} \right) dn_1 \tag{7.6}$$

If we consider a system consisting of pure solvent with the same total volume *V*, then the free energy of this system can be expressed as: [173]

$$dA' = -\left(p - \frac{\mu_0'}{V_0} \right) dV \tag{7.7}$$

where μ_0' represents the chemical potential of the pure solvent. Subtraction of Eq. 7.7 from Eq. 7.6 will results: [173]

$$d(A - A') = \left(\frac{\mu_0 - \mu_0'}{V_0} \right) dV + \left(\mu_1 - \frac{\mu_0 V_1}{V_0} \right) dn_1 \tag{7.8}$$

The difference $A - A'$ is the change in free energy when a given amount of solvent molecules is replaced by the same volumetric amount of macromolecules at constant *T* and *V*. Since osmotic pressure of the binary system is defined by $\Pi \equiv -(\mu_0 - \mu_0')/V_0$,[61, 173] we can write Eq. 7.8 as:

$$d\tilde{A} = -\Pi dV + \tilde{\mu}_1 dn_1 \tag{7.9}$$

where $\tilde{A} \equiv A - A'$. Equation 7.9 shows that a liquid mixture of incompressible binary components can be equivalently treated as a compressible fluid consisting of one effective component with pressure Π and chemical potential, $\tilde{\mu}_1 \equiv \mu_1 - \mu_0(V_1 / V_0)$ denoting the effective chemical potential.[173] In addition, we can appreciate that the LLPS of this binary system can be treated as the gas-liquid condensation of the one-component gas system.[176]

7.4 Protein-protein Interactions in Aqueous Mixtures

The thermodynamic formalism introduced in the previous section can be used to describe protein-protein interactions. All macromolecules, including proteins, exhibit varying degrees of weak, nonspecific interactions with each other and with solvent systems.[177] In broad terms, the solvent system represents here a mixture of solvent molecules, buffer, and salt ions used to maintain the functional ionic strength of protein mixtures. For simplicity, the parts of the mixture other than the protein can be considered as a background medium focusing on the protein component of the mixture as an effective one-component system.[178, 179] The interactions between protein macromolecules tend to be very low in affinity, short-lived, lacking stereospecificity, and distributed throughout the surface of the protein.[177, 180] By fitting the experimental data of proteins using the theoretical concepts from colloidal sciences, it had been concluded that, due to their effective surface charge, proteins interact by long-range electrostatic repulsion at low ionic strength which becomes screened as the ionic strength increases.[181] This allows short-range attractive forces to become more important. The solubility of proteins and their phase separations are controlled by the protein-protein net interactions in the background solvent.[177, 180] When these net interactions become sufficiently attractive then phase separation will occur and the molecular mixture separates into two phases; a large volume low concentration dilute phase, and a small volume, high concentration condensed phase.[177, 180-182]

Thermodynamically, the protein-protein interactions in water can be described using the model of a non-ideal gas.[183] The effectively one component protein-water mixture can be characterized by expanding the virial equation of state:[184]

$$\frac{\Pi}{k_B T} = \frac{\phi_1}{V_1}(1 + B\phi_1 + \cdots) \tag{7.10}$$

or equivalently, we can also write

$$\frac{\tilde{\mu}_1 - \tilde{\mu}_1^0}{k_B T} = \ln\left(\frac{\phi_1}{V_1}\right) + 2B\phi_1 + \cdots \tag{7.11}$$

where $\tilde{\mu}_1^0$ is the effective chemical potential in standard states and B is the second virial coefficient. This parameter is used to quantify intermolecular interactions between the protein molecules. In continuum solvent generalization, B describes the two-body solvent-mediated interactions.[185] If on average, there are attractive interactions between the protein molecules, B will be negative and results in the lowering of the osmotic pressure (and chemical potential) of the solution.[186] On the contrary, the repelling protein-protein interactions result in positive B values and increased osmotic pressure (and chemical potential).[186] Assuming that the interaction potential between protein molecules is averaged over angular coordinates, B can be expressed as:[187]

$$B(T) = \frac{2\pi}{V_1}\int_0^\infty r^2[1 - e^{-u(r)/k_B T}]\,dr \tag{7.12}$$

where $u(r)$ is the spherically symmetric potential energy for protein-protein interactions.[187] A simple model that allows us to unambiguously identify three important parameters describing protein-protein interactions, namely the size of particles, range of interactions, and the strength of

interactions, is the square-well potential model. In this model, the potential energy, $u(r)$ for a pair of protein molecules having a hard-core diameter (σ) and separated by a distance *r* is given by:[188]

$$u(r) = \begin{cases} +\infty, & \text{for } r < \sigma, \\ -\varepsilon, & \text{for } \sigma \le r < \lambda\sigma, \\ 0, & \text{for } r \ge \lambda\sigma. \end{cases} \tag{7.13}$$

where $\varepsilon > 0$ for attractive interactions and characterizes the depth of well (magnitude of interaction). The parameter λ, with $\lambda > 1$ is a constant describing the width of the well (range of interaction) and plays a fundamental role in the location of the phase diagram and LLPS metastability. Using the square-well potential in Eq. 7.12, the expression for *B*(T) can be obtained as:[187]

$$B(T) = 4\left[\lambda^3 - e^{\varepsilon/k_B T}\left(\lambda^3 - 1\right)\right] \tag{7.14}$$

In the special case considering protein molecules as a hard-sphere ($\varepsilon = 0$ and $\lambda = 1$) $B^{\mathrm{HS}} = 4$.[182] Equation 7.14 gives *B* as a function of temperature.[187] Equation 7.14 quantifies the strength of interactions between protein molecules required to derive the phase separation. It has been observed that for various protein systems the value of the normalized second virial coefficient at the critical LLPS temperature is universal:[182, 189]

$$\frac{B}{B^{\mathrm{HS}}} \approx -1.5 \tag{7.15}$$

It has also been reported that the optimal range of protein crystallization corresponds to the slightly negative value of the B / B^{HS}.[172]

7.5 Liquid-liquid Phase Boundary

We now link the LLPS boundary to the behavior of protein chemical potential, $\tilde{\mu}_1$. The composition of two co-existing phases, denoted as I and II, can be determined from the following two equilibrium conditions.[175, 176]

$$\tilde{\mu}_1(\phi_1^{(\mathrm{I})}, T_{\mathrm{ph}}) = \tilde{\mu}_1(\phi_1^{(\mathrm{II})}, T_{\mathrm{ph}}) \tag{7.16}$$

$$\Pi(\phi_1^{(\mathrm{I})}, T_{\mathrm{ph}}) = \Pi(\phi_1^{(\mathrm{II})}, T_{\mathrm{ph}}) \tag{7.17}$$

where $\phi_1^{(\mathrm{I})}$ and $\phi_1^{(\mathrm{II})}$ are the volume fraction of the macromolecule in the co-existing phases I and II, respectively and T_{ph} is the phase separation temperature. From these equilibrium relationships of Eq. 7.16 and Eq. 7.17, the following equivalent expression can be obtained: [175, 176]

$$(\phi_1^{(\mathrm{II})} - \phi_1^{(\mathrm{I})})\tilde{\mu}_1(\phi_1^{(\mathrm{I})}) = \int_{\phi_1^{(\mathrm{I})}}^{\phi_1^{(\mathrm{II})}} \tilde{\mu}_1(\phi_1) d\phi_1 \tag{7.18}$$

The graphical form of Eq. 7.18 is known as Maxwell equal-area rule.[175, 176] The LLPS phase boundaries can be constructed by using Eq. 7.18 in terms of $\phi_1^{(\mathrm{I})}$ and $\phi_1^{(\mathrm{II})}$.[190, 191] Figure 7.2(A) shows a representative ϕ_1 vs. $\tilde{\mu}_1$ plots at three different temperatures. For the curve shown in black, at $T = T^c$, $\tilde{\mu}_1(\phi_1^c, T^c)$ displays a horizontal inflection point. This temperature corresponds to the critical point.[192] The critical point, satisfies the conditions of $(\partial\tilde{\mu}_1 / \partial\phi_1)_{\phi_1^c, T^c} = 0$ and $(\partial^2\tilde{\mu}_1 / \partial\phi_1^2)_{\phi_1^c, T^c} = 0$.[176] The highest temperature curve (red curve) *i.e.,* for $T > T^c$, the chemical potential curve is monotonically increasing with ϕ_1. In this temperature domain, the system remains homogeneous at any ϕ_1. For the chemical potential curve calculated at $T < T^c$ (green curve), the immiscibility gap where LLPS occurs is defined by the solid circles for which

equilibrium condition Eq. 7.16 holds. The areas of curves inside the dashed line satisfy the Maxwell equal-area rule (Eq. 7.18) and describe phase equilibrium together with Eq. 7.16. This curve exhibits maxima and minima, represented using letters *b* and *c*, respectively.[176] These extremes demark the spinodal boundary (see section 7.2) inside which $(\partial\tilde{\mu}_1/\partial\phi_1)_T < 0$.[176] The region between these points is thermodynamically unstable. In Fig. 7.2(A), the points represented using letters *a* and *d* establish the regions where the solution will undergo LLPS. The phase separation between the regions *a*-*d* will occur through one of the two mechanisms as mentioned in section 7.2.[176] If the system is unstable (region *b*-*c*), such that $(\partial\tilde{\mu}_1/\partial\phi_1)_T < 0$ then the phase separation will occur without an energy barrier following the spinodal decomposition. On the other hand, if $(\partial\tilde{\mu}_1/\partial\phi_1)_T > 0$ (region *a*-*b* and *c*-*d*) then the phase separation will occur through nucleation and growth, consistent with the formation of spherical droplets.[193]

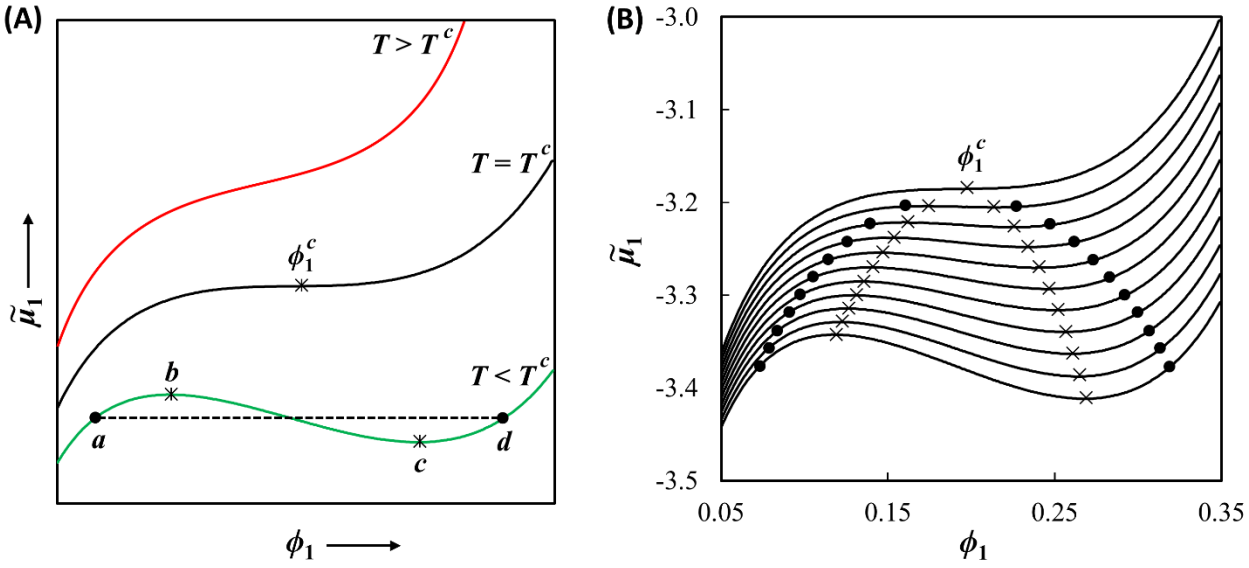

Figure 7.2 Typical isothermal plots of $\tilde{\mu}_1$ as a function of ϕ_1 at three representative temperature (A) and several different temperatures decreasing from top to bottom (B). The crosses on the curve represents points on the spinodal boundary and black dots show binodal boundary. The areas between dashed line and corresponding curves follow the Maxwell equal-area rule. Image in (B) adopted from Ref. [176] is obtained from the Monte Carlo simulations using square-well potential model and $\lambda = 1.25$. The isotherms result from variations of $\varepsilon / k_B T$ from 1.267 to 1.317 in steps of 0.005.

Figure 7.2(B) shows ϕ_1 vs. $\tilde{\mu}_1$ plots at eleven different temperatures data obtained using Monte Carlo simulations for spherical particles in the presence of attraction energy using the square-well potential and $\lambda = 1.25$.[176] The studies mentioned in Ref. [[176]] show that a decrease in λ (range of interactions), shifts ϕ_1^c to higher values leading to the metastability. All temperature profiles in Fig. 7.2(B), other than that of the critical temperature are associated with miscibility gaps. These identity the domain in which LLPS occurs. This domain is shown using solid black dots in Fig. 7.2(B) and illustrates the typical dome-like shape of the LLPS boundary.[176] The crosses represent the points demarking the spinodal boundary within the LLPS domain.

7.6 Effective Protein-protein Interactions in Protein-salt-water Solutions

At low ionic strength of the protein solution, the presence of salt in the protein mixture modifies the repulsive protein-protein electrostatic interactions through a mechanism known as the diffusive screening of the protein charge.[172] Increasing the ionic strength typically decreases the range and magnitude of screened electrostatic repulsive interactions.[172, 181] Hence, the solution phase is more prone to LLPS on increasing the ionic strength.[172] The effects of salts nature and type on protein-protein interactions are typically reflected in the second virial coefficient.[172] Increases in the concentration of the monovalent salts ions, such as NaCl in lysozyme solutions, make *B* more negative by increasing the relative contribution of attractive protein-protein interactions compared to the reduced electrostatic repulsion.[172, 194]

To account for the effect of salts on protein interactions and protein phase behavior the Derjaguin-Landau-Verwey-Overbeek (DLVO) theory can be used.[195] According to this theory, particle-particle interactions are described by three contributions: short-range excluded-volume or

steric repulsions, short-range van der Waals attractions, and long-range electrostatic repulsions.[195, 196] In DLVO potential, Coulomb electrostatic repulsive interactions are readily parametrized by macroscopic solution properties, such as ionic strength and dielectric permittivity.[195] The DLVO potential, $u_{\mathrm{DLVO}}(r)$, is written as:[195, 197]

$$u_{\mathrm{DLVO}}(r) = u_{\mathrm{HS}}(r) + u_{\mathrm{SC}}(r) + u_{\mathrm{VDW}}(r) \tag{7.19}$$

where the hard-sphere steric contribution, $u_{\mathrm{HS}}(r)$, is given by:[195, 197]

$$u_{\mathrm{HS}}(r) = \begin{cases} \infty, & \text{for } r \le \sigma + \delta, \\ 0, & \text{for } r > \sigma + \delta. \end{cases} \tag{7.20}$$

where δ is a layer thickness describing the Stern layer and the solvation shell around a protein.[195] For $r > (\sigma + \delta)$, the screened Coulomb contribution $u_{\mathrm{SC}}(r)$ is given as:[195, 197]

$$u_{\mathrm{SC}}(r) = \frac{(eZ_{\mathrm{P}})^2}{4\pi\varepsilon_0\varepsilon_{\mathrm{s}}} \frac{\exp[-\kappa(r-\sigma)]}{(1+\kappa\sigma/2)^2 r} \tag{7.21}$$

where ε_0 and ε_{s} are the permittivity of the vacuum and the solvent, respectively, which exhibits weak dependence on temperature.[197, 198] The Debye screening length, κ^{-1} can be given as:[195, 197]

$$\kappa^{-1} = \left(\frac{\varepsilon_0\varepsilon_{\mathrm{s}} k_{\mathrm{B}} T}{2\times 10^3 e^2 N_{\mathrm{A}} I} \right)^{1/2} \tag{7.22}$$

where $I = 1/2\sum_i z_i^2 c_i$ is the ionic strength with z_i and c_i are the charge and concentration (M) of the *i*th ionic species, respectively (see also section 6.1 of Chapter 6). The van der Waals contribution $u_{\mathrm{VDW}}(r)$ to Eq. 7.19 is approximated as:[195, 197]

$$u_{\mathrm{VDW}}(r) = -\frac{A_{\mathrm{H}}}{12}\left(\frac{\sigma^2}{r^2-\sigma^2} + \frac{\sigma^2}{r^2} + 2\ln\left[1-\frac{\sigma^2}{r^2}\right]\right) \tag{7.23}$$

where A_{H} is the effective Hamaker constant,[199] which determines the strength of van der Waals contribution. It also accounts for non-DLVO forces, such as hydration, the hydrophobic effect, and hydrogen bonding, *etc*.[199] From the DLVO potential (Eq. 7.19) the normalized second virial coefficient can be computed using Eq. 7.12 as:[195, 197]

$$\frac{B}{B^{\mathrm{HS}}} = 1 + \frac{3}{4(\sigma+\delta)^3}\int_{\sigma+\delta}^{\infty}\left(1-\exp\left[-\frac{u_{\mathrm{SC}}(r)+u_{\mathrm{VDW}}(r)}{k_{\mathrm{B}}T}\right]\right)r^2 dr \tag{7.24}$$

where $B^{\mathrm{HS}} = 4(1+\delta/\sigma)^3$. In the DLVO model, the salt concentration and dielectric properties are taken into account through the repulsive screened Coulomb contributions (Eqs. 7.21 and 7.22).[195] Attractive interactions are effectively taken into account by the values of A_{H} and δ (Eqs. 7.23 and 7.24).[195] The value of B/B^{HS} at the phase separation temperature depends on the protein charge Z_{P}, ionic strength of the solution, and dielectric properties of the solution.[195] Figure 7.3 shows a typical behavior of lysozyme B/B^{HS} dependence on salt (NaCl) concentration at different values of Hamaker constant.[200] The magnitude of B/B^{HS} decreases (more negative) with an increase in the value of Hamaker constant. The optimum of Hamaker constant can be estimated from values of B determined by light scattering measurements[196] which is set for $8.3k_BT$ for lysozyme and NaCl mixture in sodium acetate buffer.[195, 198, 201, 202]

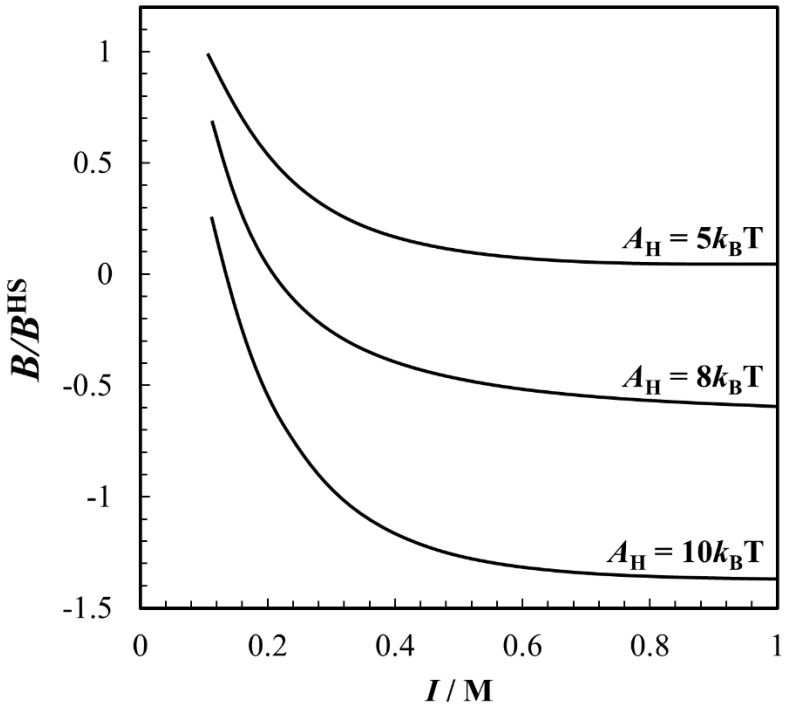

Figure 7.3 Calculated values of B/B^{HS} as a function of salt ionic strength, *I*, at three values of Hamaker constant, A_H, $5k_BT$, $8k_BT$, $10k_BT$ in NaCl solution at pH 4.5 using $\sigma = 34.4\text{Å}$ and $\delta = 6.9\text{Å}$ for lysozyme. The image is adopted from Ref. [200].

Chapter 8

Materials and Experimental Methods for LLPS Studies of Lysozyme

8.1 Materials and Solution Preparation

Two-times recrystallized and lyophilized egg-white lysozyme was purchased from Worthington Biochemical Corporation, NJ, USA, and used without further purification. Our previous chemical analysis shows that this lysozyme material consists of 89% isoelectric lysozyme, 9% water, and 2% HCl. Protein concentrations in aqueous solutions were determined based on UV absorption at 280 nm as mentioned in section 3.1 of Chapter 3. Molar concentrations were calculated using the lysozyme molar weight of 14.307 $kg \cdot mol^{-1}$ at the isoelectric point. Analytical reagent grade Sodium Chloride (NaCl, Mallinckrodt), 4-(2-hydroxyethyl)-1-piperazineethanesulfonate (HEPES, 238.30 $g \cdot mol^{-1}$, Sigma Aldrich) Tris (Hydroxymethyl) Amino Methane (Tris, 121.14 $g \cdot mol^{-1}$, Fischer Sci.), Sodium Hydroxide (NaOH, 40.00 $g \cdot mol^{-1}$, Fischer Sci.), Hydrochloric Acid (HCl 36.5-38.0% w/w, Pharmca), Sodium Phosphate monobasic ($NaH_2PO_4 \cdot H_2O$, 137.99 $g \cdot mol^{-1}$, Fischer Sci.), Sodium Phosphate dibasic (Na_2HPO_4, 141.96 $g \cdot mol^{-1}$, Fischer Sci.) and N,N-dimethylindoaniline dye (bromophenol blue, 669.96 $g \cdot mol^{-1}$, Sigma Aldrich) were used without further purification. De-ionized water was passed through a four-stage Millipore filter system to provide high-purity water for all the experiments. Aqueous stock solutions of HEPES, HEPES-NaCl, Tris-NaCl, Na_2HPO_4/ NaH_2PO_4 and HEPES-NaCl at pH 7.4 were prepared by solute weight

and volumetric flasks. The targeted value of pH was obtained by adding small amounts of aqueous ≈ 0.1M NaOH to HEPES stock solutions or aqueous ≈ 0.1 M-HCl to Tris stock solutions prior final volume adjustment. Lysozyme aqueous solutions were prepared by first mixing protein powder with NaCl-free HEPES or Tris stock solutions followed by one dialysis step (Amicon, Millipore, 10-kDa cutoff membrane) against these same stock solutions. Lysozyme solutions were then transferred into centrifugal filter devices (Amicon Ultra, Millipore, 10-kDa cutoff membrane) where they were dialyzed exhaustively into HEPES-NaCl or Tris-NaCl stock solutions and concentrated to final targeted protein concentration (up to ≈ 260 $g \cdot L^{-1}$) using a centrifuge (Allegra 25R centrifuge, Beckman Coulter). Dilution of these concentrated protein solutions was achieved by adding HEPES-NaCl or Tris-NaCl stock solutions. The same approach was used to prepare solutions for turbidity experiments in the presence of phosphate buffer, Isothermal Titration Calorimetry (ITC) experiments at pH 5.4 and protein-dye binding experiments (phenol blue is previously added into the HEPES-NaCl stock solution).

8.2 Turbidity Measurements

The LLPS temperature, T_{ph}, was determined by measuring the turbidity of freshly prepared aqueous lysozyme samples as a function of temperature. A homogenous small sample (≈200 μL) with a given composition was first incubated at 50 °C for ≈ 5 min prior to the turbidity experiment. Figure 8.1 shows the scheme of the turbidity meter apparatus used in the studies. The turbidity meter is comprised of a programmable circulating bath (1197P, VWR), a calibrated thermocouple (±0.1 °C), a homemade optical cell, where the initially-transparent sample (optical path of L = 0.4 cm) and a thermocouple probe are located.[203] Collimated light from a solid-state laser (633 nm, 5 mW, Coherent) passes through the sample, and its transmitted intensity, I, is recorded by a photodiode detector coupled with a computer-interfaced optical meter (1835-C Newport). After

recording the transmitted intensity, I_0, of the initially transparent sample, the temperature of the bath was changed at a constant rate of ±1 °C/min, and both temperature and transmitted intensity were continuously recorded. The opacification and phase separation as a function of temperature were monitored by using turbidity, τ, which can be given as:

$$\tau(T) = \frac{1}{L} \ln\left(\frac{I_0}{I}\right) \tag{8.1}$$

The temperature at which the turbidity shows a sharp increase upon cooling was chosen to identify the value of T_{ph} (cloud point). After achieving sample clouding by cooling (typically in the range from -15 to 5 °C), the temperature of the bath was steadily increased up to room temperature (≈ 22 °C).

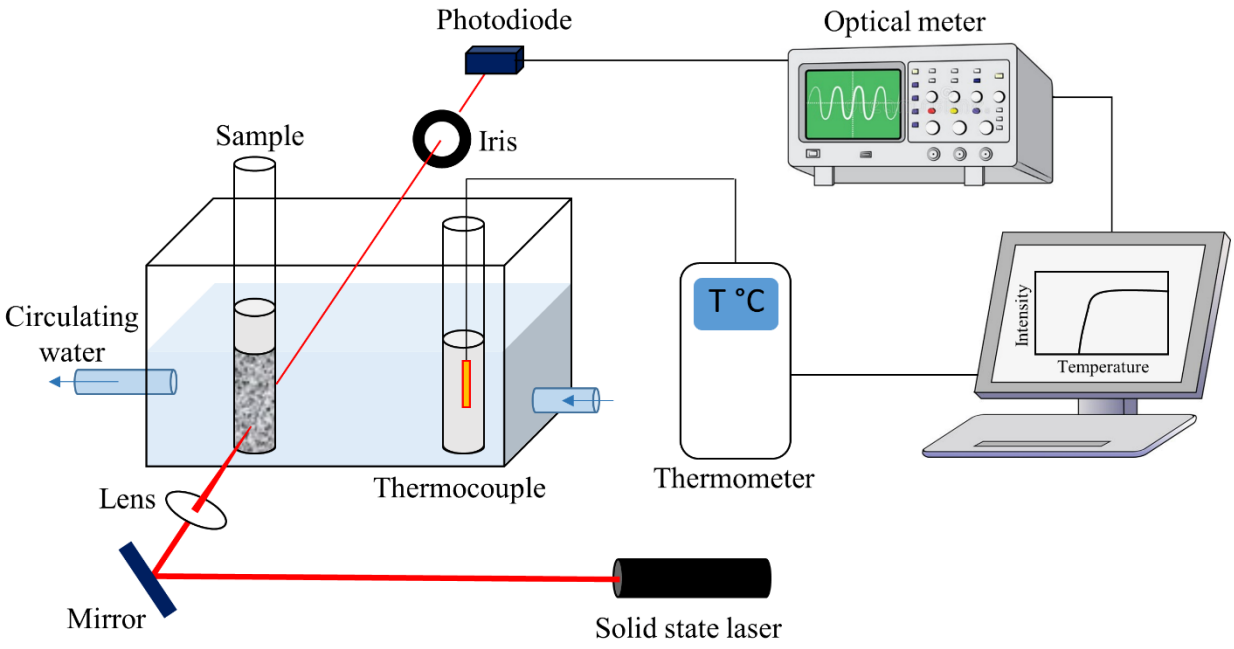

Figure 8.1 Scheme for the turbidity meter apparatus.

8.3 Optical Microscopy

After phase separation, ≈ 1 μL of the cloudy samples were promptly applied on the microscopic slide and covered by a coverslip. The sample was observed under a light microscope (Axioskop 40, Zeiss) using bright-field, polarization, and phase-contrast microscopy. The 20x, 40x, and 63x objectives were used to analyze the sample. Images were taken using a digital camera (Axiocam MRc, Zeiss) interfaced with a computer software (Axiovision AC 4.5, Zeiss).

8.4 Solubility Measurements

In the case of microparticles, cloudy samples (≈400 μL), prepared by cooling below LLPS temperature, were transferred into capped test tubes. These samples were then fully immersed in a temperature-controlled water bath at the desired temperature. Sample stirring was achieved by test-tube rotation (0.2 rpm) leading to a cyclic sample inversion inside the water bath, with mixing facilitated by a small glass bead inserted inside the test tube. After one day of equilibration, samples were positioned vertically and held stationary to allow for macroscopic phase separation inside the water bath. After separation was achieved, samples were quickly centrifuged by using our centrifuge with temperature control. The sample holders used in the centrifugation process were previously inserted in the water bath to minimize temperature differences with samples. The protein concentration in the supernatant was measured by spectrophotometer and was taken as the solubility values. Experiments repeated after the following day confirmed the solubility values with an error of ≈ 5% or less. To determine solubility data of rod-shaped crystals, heterogeneous samples were first taken to 50 °C to dissolve microparticles and then incubated at 4 °C, well above the clouding temperatures, to amplify crystal formation. Crystals were then added to a protein-free HEPES-NaCl medium and the supernatant concentration was measured using the same approach and analysis described for microparticles.

8.5 Dynamic Light Scattering

Dynamic light scattering (DLS) is a non-invasive and non-destructive technique that can be used to determine the diffusion coefficient, *D*, of macromolecule in solution.[204-206] It is based on the measurement of concentration fluctuations caused by the Brownian motion of solute particles in the solution.[204, 205] The difference between the polarizability of these solute particles and the surrounding medium (*i.e.*, solvent) results the scattering of incident photons in all directions. The total scattered electromagnetic field, *E*, of the sample containing *N* identical solute particles, can be given as:[205]

$$E = E^0 \sum_i^N e^{i\vec{q}.\vec{r}_i} \tag{8.2}$$

where E^0 is the amplitude of the electromagnetic wave scattered by each particle, $\vec{r}_i$ is the position vector of the *i*th particle and $\vec{q}$ is the scattering vector that can be calculated as:[205, 206]

$$q = |\vec{q}| = \frac{4\pi n}{\lambda} \sin\left(\frac{\theta}{2}\right) \tag{8.3}$$

where, *n* is the refractive index, λ is the wavelength of light in vacuum and θ is the scattering angle. The intensity of scattered light is proportional to the square of the amplitude of the electromagnetic wave and can be given as: [199]

$$I(t) = I^0 \left| \sum_i^N e^{i\vec{q}.\vec{r}_i} \right|^2 = I^0 \left[N + 2 \sum_{i=1}^N \sum_{j>1}^N \cos \vec{q} \cdot (\vec{r}_i - \vec{r}_j) \right] \tag{8.4}$$

where $\vec{r}_i - \vec{r}_j$ is the difference in the position between particle *i* and particle *j*. The first term in the square bracket, *N*, represents the net contribution of all particles, while the trigonometric term describes the interference of the scattered waves due to the different positions. According to Eq.

8.4, $I(t)$ fluctuates because $\vec{r}_i - \vec{r}_j$ fluctuates. The measured scattered-intensity is a stochastic function of time due to particle random motion.[204, 205] The scattered intensity, $I(t)$ at a given time correlates with the scattered intensity at a later time, $t+\tau$. This implies that a correlation function, associated with this stochastic scattered intensity can be built. Slow (rapid) fluctuations of $\vec{r}_i - \vec{r}_j$, correspond to a small (great) loss of correlation over time. Hence, a low (large) diffusion mobility corresponds to a slowly (rapidly) decaying correlation function. In the limit of zero mobility, fluctuations of $\vec{r}_i - \vec{r}_j$ are "frozen" and no loss of correlation over time occurs.[204-206]

Correlation between two scattered intensity values can be determined by introducing the normalized intensity correlation function, $g^{(2)}(\tau)$:[205, 206]

$$g^{(2)}(\tau) \equiv \frac{\langle I(t)I(t+\tau)\rangle}{\langle I(t)\rangle^2} = \frac{\int_0^\infty I(t)I(t+\tau)dt}{\langle I(t)\rangle^2} \tag{8.5}$$

Correlation functions are calculated by using a correlator, a circuit board composed of various logic chips and operational amplifiers which continuously multiply and add measured intensity values. This device collects the $I(t)$ as a function of time (with the difference of 10^{-9} to 10^{-3} seconds) and computes $g^{(2)}(\tau)$ by numerically solving the integral of Eq. 8.5. For identical particles with diffusion coefficient, *D*, the correlation function is described by the Siegert equation:[206]

$$g^{(2)}(\tau) = 1 + \exp(-2q^2 D\tau) \tag{8.6}$$

Equation 8.6 shows that $g^{(2)}(\tau)$ is exponentially decaying over time, with a lifetime that is inversely proportional to the particle diffusion coefficient. However, in a typical DLS experiment,

the ensemble of scattering particles is not assumed to be monodisperse and Eq.8.6 is typically replaced (as in our experiments) by this more general equation: [206]

$$g^{(2)}(\tau) = \mathrm{B} + A\left[\sum_i W_i e^{-q^2 D_i \tau}\right]^2 \tag{8.7}$$

where $A \leq 1$ is the coherence factor that depends on detector area, optical alignment, and scattering properties of macromolecules, A = 1 corresponds to the theoretical limit in which scattered light is collected by the detection system from an infinitesimal solid angle and B is the baseline (~ 1).[206] Both parameters are determined through the application of the least-squares method. The term D_i is the diffusion coefficient associated with type *i* particles and W_i is the corresponding normalized scattering contribution, with W_i being proportional to $N_i M_i^2$ where N_i is the number of type *i* particles and M_i their corresponding molecular weight. Experimentally, a grid of *D*, $\{D_i\}$ is constructed and the corresponding $\{W_i\}$ are determined using the least-squares method, which gives the normalized light-scattering distribution $W(D)$ of diffusion coefficient. The average diffusion coefficient of the distribution can be determined as:

$$\langle D \rangle_z = \sum_{i=1}^{n} W_i D_i \tag{8.8}$$

where subscript represents the z-averaged distribution.

The light scattering instrument (Fig. 8.2) used for the studies mentioned in this dissertation, is built using the following main components: He-Ne laser (35 mW, 632.8 nm, Coherent Radiation), manual goniometer and thermostat (Photocor Instruments), multi-tau correlator, APD detector, and software (PD4042, Precision Detectors).[75] The laser beam is focused to the width around 10μm by a lens onto the center of the sample. The scattered light from the scattering volume

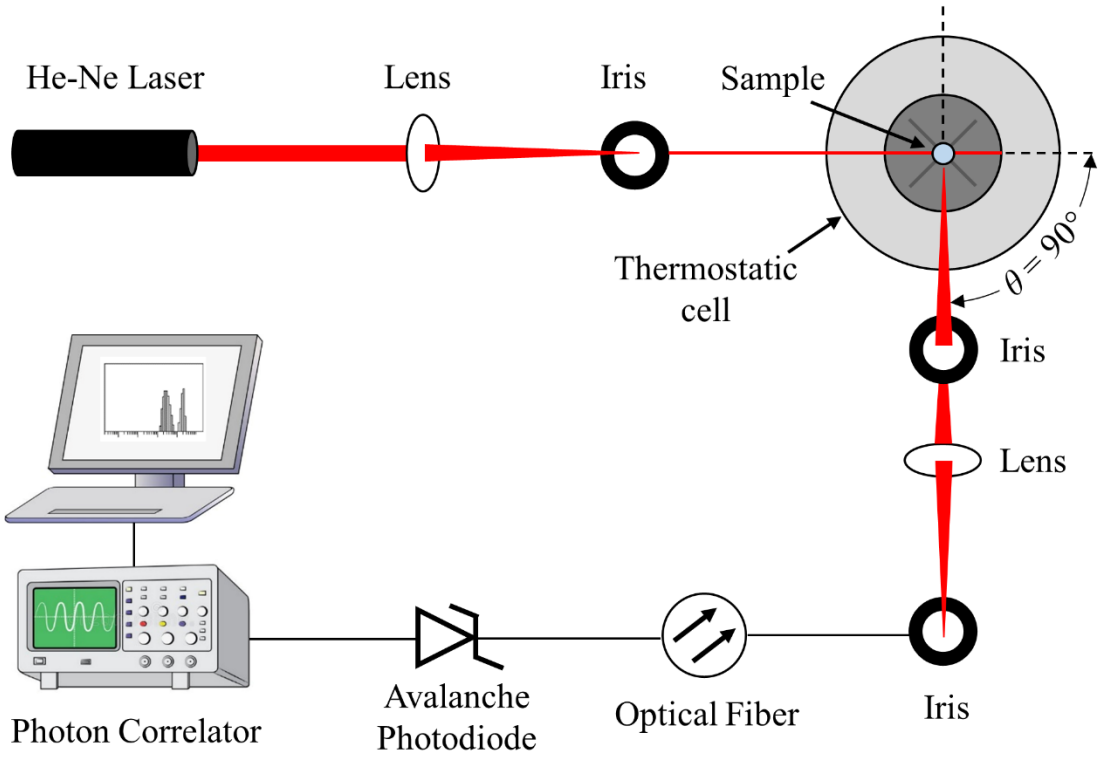

Figure 8.2 Scheme for the dynamic light scattering apparatus.

is collected at a scattering angle of 90° and focused by a condenser lens and an iris placed between the sample and the lens. The scattered light is then transmitted to the avalanche photodiode through an optical fiber which converts the light photos to the electric pulses which are processed and analyzed by the 256-channel correlator. The correlation functions are calculated after every 2 seconds and averaged over 300-3200 accumulations times to minimize the statistical errors.

For our studies, the measurements of dynamic light scattering were performed at 25.0 ± 0.1 °C. All protein samples were filtered through a 0.02 μm filter (Anotop 10, Whatman) and placed in a test tube. The scattering vector, given in Eq. 8.3, is calculated using n = 1.33 and λ = 632.8 nm. The scattered-intensity correlation functions were analyzed using a regularization algorithm (Precision Deconvolve 32, Precision Detectors). With the exception of experiments at 0.40 M HEPES, all scattered-intensity distributions were found to be monomodal and the

corresponding *z*-average diffusion coefficient, *D*, was calculated. In the 0.40 M HEPES case, as a small peak associated with a relatively high diffusion coefficient of ≈ 0.6×10^{-9} $m^2\cdot s^{-1}$ was also observed in the scattered-intensity distributions. This peak, which was attributed to HEPES contribution, was removed prior to the calculation of *D*. Values of *D* as a function of protein concentration were linearly extrapolated to zero concentration in order to extract the value of the protein tracer-diffusion coefficient, D_0. The corresponding hydrodynamic radius was calculated using the Stokes-Einstein equation (see section 2.2 of Chapter 2):

$$R_h = \frac{k_B T}{6\pi\eta D_0} \tag{8.9}$$

where T = 298.15 K, η the viscosity of the corresponding protein-free aqueous solution.[75] Viscosity values for all protein-free aqueous solutions were measured in our laboratory by using an Ubbelohde viscometer inserted inside a water bath at 25.00 °C with temperature control of 1 mK. Related density measurements were performed by using the method detailed in section 3.2 of Chapter 3.

8.6 Determination of HEPES Concentration in the Supernatant

Aqueous Lysozyme-HEPES-NaCl samples with lysozyme concentration of 200 $g\cdot L^{-1}$ were quenched to -10 °C to induce clouding. After a given incubation time, cloudy samples were quickly centrifuged by using our centrifuge with temperature control. An amount of transparent supernatant was then isolated. An aliquot of this supernatant was transferred into a centrifugal filter device (Amicon Ultra, Millipore, 10-kDa cutoff membrane) to remove lysozyme. After centrifugation, a known aliquot (≈ 250 μL) of the lysozyme-free filtrate was taken for the characterization of HEPES concentration. As a control experiment, the same centrifugation approach was used for a HEPES-NaCl stock solution in the absence of lysozyme. We then

performed hydrogen-ion titrations to determine the concentration of the HEPES basic form using the supernatant as the titrand. Measurements of pH were made using a Corning model 130 pH meter with a combination of pH microelectrode (Orion, model 8220BNWP). The meter was calibrated with standard pH 7 and pH 4 buffers. In all cases, the initial pH of the titrand is found to be 7.4. Small aliquots (≈ 10 μL) of a previously standardized 0.100 M HCl titrant solution were consecutively transferred into the titrand solution by using a syringe fitted with a plastic tubing. After a given aliquot addition, the pH value was recorded under mild stirring conditions. The titration was stopped when the pH value was found to be ~3.0. The weight of the syringe was measured after each titrant addition so that the amount of added titrant solution could be determined. Density values were used to convert masses into the corresponding solution volumes so that the number of moles of added HCl, n_{HCl}, could be calculated. A discrete set of titration data (n_{HCl}, pH) was then used to calculate $(n_{\mathrm{HCl}}^{i+1} - n_{\mathrm{HCl}}^{i}) / (\mathrm{pH}^{i} - \mathrm{pH}^{i+1})$ as a function of $(n_{\mathrm{HCl}}^{i+1} + n_{\mathrm{HCl}}^{i}) / 2$, where i is the integer number labeling a given titrant addition. The value of $(n_{\mathrm{HCl}}^{i+1} + n_{\mathrm{HCl}}^{i}) / 2$ corresponding to the maximum of $(n_{\mathrm{HCl}}^{i+1} - n_{\mathrm{HCl}}^{i}) / (\mathrm{pH}^{i} - \mathrm{pH}^{i+1})$ was used to determine the number of moles and concentration of HEPES basic form based on 1:1 stoichiometry. The corresponding error was evaluated from $(n_{\mathrm{HCl}}^{i+1} + n_{\mathrm{HCl}}^{i}) / 2$.

8.7 Bromophenol blue Binding Experiments

Aqueous Lysozyme-HEPES-NaCl samples with lysozyme concentration of 120 $g \cdot L^{-1}$ and bromophenol blue concentration of ≈ 100 μM were quenched to -10 °C to induce clouding. Cloudy samples were quickly centrifuged by using Allegra 25R centrifuge (Beckman Coulter) with temperature control. An amount of transparent supernatant was then isolated and its bromophenol

blue concentration was characterized. Dye concentrations were determined spectrophotometrically using the known extinction coefficient value of 6.60×10^4 $M^{-1}\cdot cm^{-1}$ at 592 nm.[207]

8.8 Isothermal Titration Calorimetry

Lysozyme-HEPES interactions were characterized by isothermal titration calorimetry (ITC) using the microcal ITC 200 system from GE healthcare life sciences.[208] ITC is a technique often used in host-guest interaction studies and to directly determine the thermodynamic parameters such as enthalpy and entropy changes, binding affinities, and stoichiometry in solution.[209, 210] In the microcalorimeter there are two cells, one acts as a reference (R) cell, the other contains the sample (S) or titrand cell of volume *V*. The electric powers w_S and w_R maintain the temperature of the sample cell T_S and reference cell T_R at pre-adjusted values. Sensitive thermocouple circuits maintain $T_S = T_R$ at any time during the experiment. When titrant is added to the titrand, the exothermic or endothermic nature of the event is recorded in terms of powers needed to maintain the $T_S = T_R$.[209, 210]

In an ITC experiment, the titrant is located inside a syringe with its needle tip positioned inside the titrand cell. Stirring is ensured by needle spinning. Precise sequential additions of volume, *v*, into the titrand cell are performed during the experiment. Each addition of titrant produces a value of differential heat which is calculated as the area associated with $w_S - w_R$ peak with respect to time. This integral is equal to the heat absorbed or released during the reaction event. The differential heat $q^{(k)}$ associated with each addition, *k*, can be given as: [209, 210]

$$q^{(k)} = \left[\left(V + v/2\right)\left(Q^{(k)}/V\right) - \left(V - v/2\right)\left(Q^{(k-1)}/V\right)\right] \Big/ \left(vC^0_{\text{titrant}}\right) \tag{8.10}$$

where $Q^{(k)}$ is the cumulative heat absorbed or released by the sample after injection *k*, and C^{0}_{titrant} is the concentration of the titrant in the syringe. To determine thermodynamic parameters from ITC, a model-based mathematical expression for the commutative heat as a function of system composition inside the cell is used. The mathematical expression for $Q^{(k)}$ is then inserted into Eq. 8.10 and the method of least squares is applied to $q^{(k)}$.[209, 210]

All ITC experiments used in this dissertation were performed at 25.0 °C. Specifically, a HEPES solution (0.18 M, titrant) was added to a dilute lysozyme solution (0.50 mM, titrand) inside the ITC cell. A given titration consists of a total of 26 titrant additions of v = 1.5 μL into the ITC cell with a volume of V = 204 μL.[208] The titrand solution was prepared by ultra-filtration at pH 5.4 and NaCl 0.20 M using a centrifugal filter device (Amicon Ultra, Millipore, 10-kDa cutoff membrane). Pure solid HEPES was then mixed with filtrate in order to prepare the titrand solution. Control experiments in which HEPES-free filtrate is added to lysozyme titrand solution produce negligible heat of mixing. Control experiments in which HEPES-filtrate solution is added to lysozyme-free filtrate as titrand solution produces significant heat of mixing related to HEPES dilution into water. Thus, related values of differential heat contribution were subtracted from those associated with lysozyme titration. The residual values of differential heat were then analyzed based on the ligand binding model with identical and independent binding sites (similar to the model discussed in section 1.2 of Chapter 1).[211] The HEPES-lysozyme binding can be described by the following relation known as Scatchard equation:[212]

$$\nu = \frac{n[\mathrm{L}]}{K + [\mathrm{L}]} \tag{8.11}$$

where K is the dissociation constant, n is the number of binding sites, [L] is free HEPES concentration and ν is the number of HEPES ions bound on one lysozyme. Eq. 8.11 leads to the following expression of cumulative heat, $Q^{(k)}$:[213]

$$Q^{(k)} = -\Delta_d H^0 V C_P^{(k)} \nu^{(k)} \tag{8.12}$$

where $C_P^{(k)}$ is the total concentration of lysozyme inside the cell after k injections and $\Delta_d H^0$ is the heat associated with one mole of bound HEPES. The term $\nu^{(k)}$ in Eq. 8.12 is given by:

$$\nu^{(k)} = \frac{n[\mathrm{L}]^{(k)}}{K + [\mathrm{L}]^{(k)}} \tag{8.13}$$

where

$$[\mathrm{L}]^{(k)} = \frac{-\left(K - C_L^{(k)} + nC_P^{(k)}\right) + \left[\left(K - C_L^{(k)} + nC_P^{(k)}\right)^2 + 4KC_L^{(k)}\right]^{1/2}}{2} \tag{8.14}$$

with $C_L^{(k)}$ being the concentration of HEPES in the cell after injection k.

Chapter 9

Effect of a Good Buffer on the Fate of Metastable Protein-rich Droplets

9.1 Introduction

The LLPS thermodynamic properties of protein aqueous solutions and their additives have been described fairly well. However, the evolution of the protein-rich liquid phase toward other protein condensed phases is not well understood. Understanding and controlling the kinetic evolution of metastable protein-rich microdroplets is important for the obtainment of protein crystals,[65, 214] comprehending formation of cell micro-compartments,[57, 215] protein aggregation,[216-218] and developing novel protein-based materials.[8] We proposed to modulate the fate of a protein-rich micro-droplets by combination of two additives. Specifically, one additive is necessary to induce LLPS. This is represented by a traditional precipitating agent acting through electrostatic,[196] salting-out[88, 196, 219, 220] or crowding mechanism.[203, 221, 222] The second additive introduces the variable that may change the fate of the protein-rich liquid phase. To reduce mixture complexity, the second additive may also be represented by buffer components at non-negligible concentrations.

We applied this strategy to lysozyme aqueous solutions in the presence of NaCl, its traditional precipitating agent. This protein was chosen because its solution properties are well characterized[66, 84-88] and LLPS can be observed in the presence of small amounts of NaCl, with

ionic strengths and pH values relevant to physiological composition (*i.e.,* 0.1-0.2 M NaCl at pH 7). Furthermore, theranostic applications of lysozyme in protein-based materials have recently emerged due to the antimicrobial properties of this protein.[8, 10, 89-91] We show that the addition of 4-(2-hydroxyethyl)-1-piperazineethanesulfonate (HEPES, 0.10 M, pH 7.4) at constant ionic strength (0.20 M including NaCl contribution) and pH leads to a major change in the fate of the protein-rich phase even if the corresponding change in the position of the LLPS boundary remains modest. This result becomes even more interesting after recognizing that the second additive we employ, HEPES, is a member of the Good's buffer family.[116] It is often believed that Good's buffers, which are extensively employed in biochemistry, exhibit negligible impact on biochemical and biological processes.[116, 117] In contrast, our findings show that this is not true for this well-known model protein, *i.e.,* HEWL.

9.2 Characterization of Temperature-turbidity Profile

To characterize the effect of HEPES on LLPS of lysozyme solutions, we focused on two aqueous systems of this protein. Both systems share the same ionic strength (0.20 M) and pH (7.4) to establish equivalent electrostatic-screening conditions (see section 7.6 of Chapter 7). These two systems differ in additives composition with one containing HEPES and NaCl (HEPES, 0.10 M; NaCl 0.15 M) and the other being the HEPES-free reference system (NaCl, 0.183 M; Tris, 0.020 M). It is important to note that these mixtures can slowly generate protein crystals. This has been verified after overnight sample incubation at 4 °C and 25 °C. Thus, all freshly prepared samples were promptly investigated. Moreover, they were first incubated at 50 °C for five minutes to hinder crystal formation and establish a unique starting point for the investigated protein systems. At this high temperature, which remains significantly lower than lysozyme unfolding temperature (≈75 °C),[223] these samples are homogeneous transparent mixtures.

As a starting point, LLPS was investigated by characterizing temperature-turbidity profiles[203, 224] for samples with lysozyme concentration, C_P, ranging from 70 to 250 g·L^{-1}. Our turbidity results are shown in Fig. 9.1 at two representative protein concentrations. Temperature-turbidity profiles show that sample clouding occurs by lowering temperature as expected for LLPS of lysozyme solutions. Clouding temperatures for the samples containing HEPES are found to be ≈10 °C lower than those observed in the reference system. The observed temperature difference corresponds to a ≈4% reduction in absolute temperature and protein-protein attraction[176] in the HEPES system. This is a modest temperature decrease, which can be related to the lower NaCl concentration in the HEPES system and a slightly weaker salting-out effect.

In the reference system, temperature-turbidity profiles show that mixtures become clear again by increasing temperature with a hysteresis gap of 1-3 °C within our experimental protein concentration range. This is a characteristic feature of LLPS, consistent with the reversibility properties of first-order phase-transitions. Indeed, we obtain similar results from experiments on

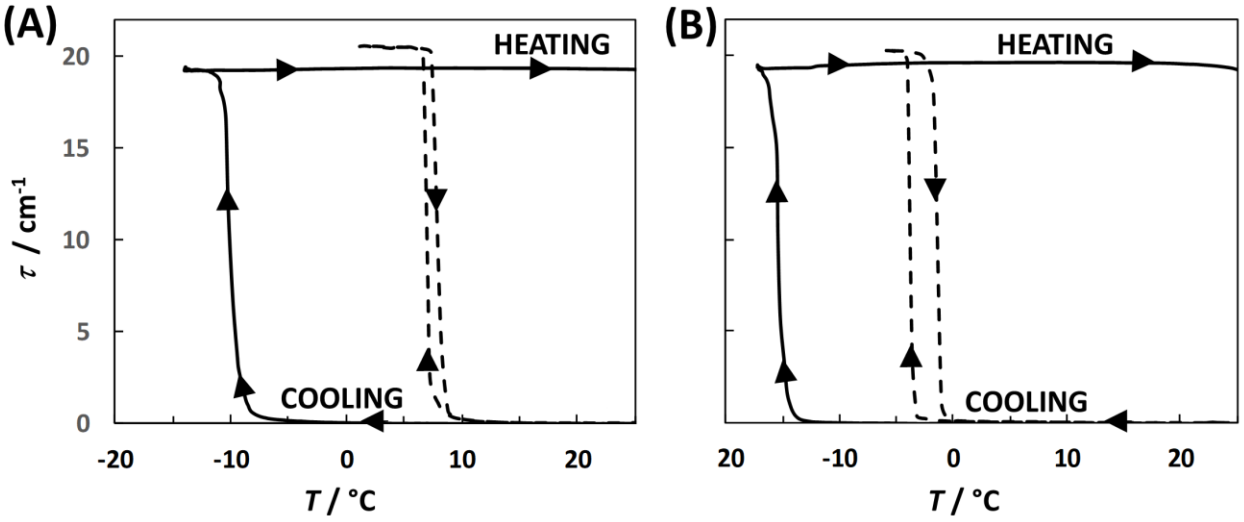

Figure 9.1 Representative temperature (T)-turbidity (τ) profiles for (A) HEPES system (solid curves) at C_P = 250 g·L^{-1} and reference system (dashed curves) at C_P = 250 g·L^{-1}, and (B) HEPES system (solid curves) at C_P = 70 g·L^{-1} and reference system (dashed curves) at C_P = 90 g·L^{-1}. Arrows indicate cooling and heating stages. Note that the freezing point of these samples occur around -20 °C.

lysozyme in the presence of 0.10 M Tris buffer or 0.10 M phosphate buffer at the same pH and ionic strength as expected from previous studies.[66, 84, 88] On the other hand, Fig. 9.1 reveals that, contrary to the reference system, lysozyme mixtures in the presence of HEPES remain cloudy at room temperature. This behavior was reproducibly observed in all our turbidity experiments with HEPES. Sample clarification could not be restored even by incubation at 25 °C after arbitrarily long periods of time. However, full sample clarification can be quickly achieved by incubation at 50 °C, thereby demonstrating process reversibility.

These findings demonstrate that HEPES have a crucial impact on the kinetic evolution of LLPS of lysozyme solutions. To further characterize the thermal behavior of our mixtures, still-images showing how sample turbidity changes as a function of temperature for both HEPES and reference system were captured. Representative snapshots for the HEPES system are illustrated in

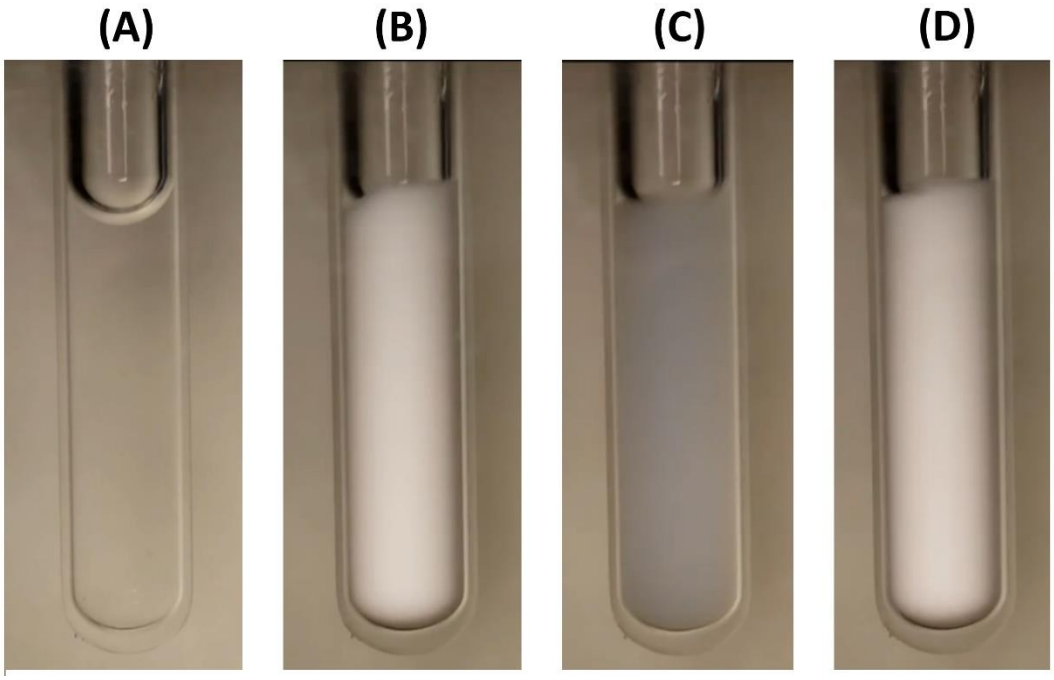

Figure 9.2 Photographs of lysozyme-HEPES sample at C_P = 250 g·L^{-1}. (A) Sample appears clear upon steady cooling, down to -8 °C (picture taken at -7 °C). (B) Sample becomes cloudy at -8 °C and remains in this state upon cooling down to -11 °C followed by heating up to -3 °C (picture taken at -8 °C). (C) Sample partially clears starting at -3 °C (picture taken at -3 °C). (D) Sample recovers its full cloudiness at 0 °C and remains in this state upon heating up to 35 °C (picture taken at 0 °C).

Figs 9.2A-D. Interestingly, after inducing sample clouding by cooling (see Fig. 9.2 A,B), a partial clarification upon heating is observed in a narrow temperature window of 3 °C (see Fig. 9.2 C) before becoming fully opaque again (see Fig. 9.2 D). Our results show that LLPS occurs at low temperatures and another phase transformation, which utilizes LLPS as a nucleation platform, rapidly and reproducibly occurs at relatively higher temperatures.

9.3 Light Microscopy Analysis

Our cloudy samples were inspected by light microscopy at room temperature. As shown in Fig. 9.3A, globular compact particles with a diameter of about 1-3 μm are observed. This shape resembles that of protein-rich liquid droplets, though droplets tend to be somewhat larger (5-10 μm).[224] As previously mentioned, these mixtures can eventually generate crystals. Indeed, relatively-large orthorhombic crystals[225-227] with a characteristic rod-shaped morphology were obtained from our lysozyme-HEPES mixtures after incubation of homogenous samples above 40 °C. These are illustrated in Fig. 9B. According to previous crystal growth and solubility studies,[225-

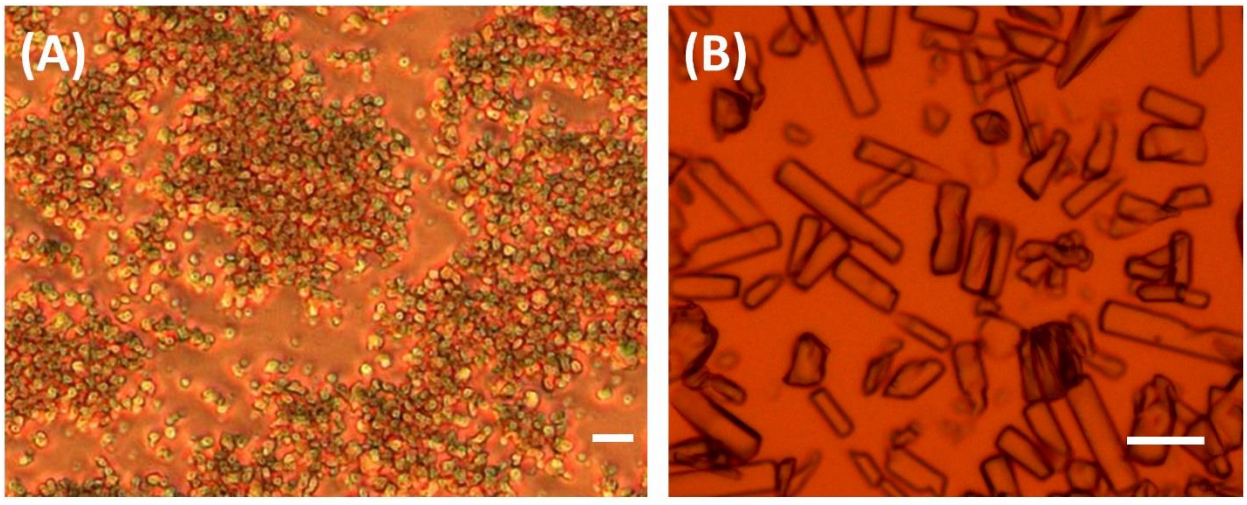

Figure 9.3 (A) Direct-field light-microscopy image showing globular condensates generated after clouding of a sample (C_P = 120 g·L^{-1}) was induced by cooling to -15 °C. Horizontal bar is 10 μm. (B) Direct-field light-microscopy image showing rod-shaped lysozyme crystals of a sample (C_P = 120 g·L^{-1}) after overnight storage at 4 °C. Horizontal bar is 30 μm. Both pictures were taken at room temperature. Both samples were initially incubated at 50 °C for 5 min.

[229] lysozyme crystals are mainly expected to exhibit tetragonal and orthorhombic morphologies, with tetragonal crystals being more stable at low temperatures. This property, which will be further discussed later, suggests that the microparticles in Fig. 9A are small tetragonal crystals.

Altogether, our results show that protein droplets act as templates for the formation of globular microparticles at relatively high temperatures. Since these particles are numerous and exhibit a narrow size distribution, this process may be exploited for the production of protein-based materials. It is important to remark that additive concentrations needed to produce this phase behavior are low compared to concentration of additives, which include denaturing organic solvents, typically employed for the preparation of protein-based materials.[8] Consistent with these observations, we also characterized the ability of microparticles to bind guest molecules by employing Bromophenol Blue as a model ligand.[207] Specifically, we find that the supernatant concentration of this dye reduces to 51% of the initial value (0.10 mM) after microparticle formation.

To further inspect the nature of the microparticles described in Fig 9.3A, we carried out similar LLPS experiments on lysozyme-HEPES at increasing NaCl concentrations, up to 0.30 M. The corresponding turbidity profiles show the same behavior as that illustrated for lysozyme-HEPES in Fig 9.1 with samples remaining cloudy at room temperature. For comparison, increasing

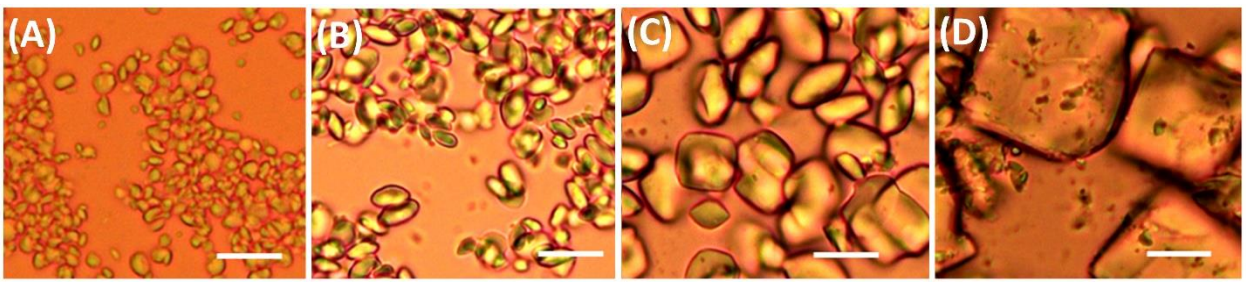

Figure 9.4 Direct-field light-microscopy images taken at room temperature showing effect of NaCl concentration (A, 0.15 M, T_{ph} = -12 °C; B, 0.20 M, T_{ph} = -6 °C; C, 0.25 M, T_{ph} = -1 °C; D, 0.30 M, T_{ph} = 4 °C) on lysozyme microparticles after clouding of the sample (C_P = 120 g·L^{-1}) was induced by cooling to -15 °C. Horizontal bar is 10 μm in all cases.

NaCl concentration to 0.4 M in the reference system still yields reversible turbidity profiles. In Fig 9.4, we can see that the size of HEPES-induced microparticles increases with NaCl concentration, revealing geometric shapes that are approximately squares, with more apparent crystalline traits of a tetragonal morphology at the highest salt concentration. These images further indicate that the microparticles in Fig. 9A are tetragonal microcrystals. It is important to note that these microcrystals are different from the relatively large protein crystals with sea-urchin morphologies previously reported under LLPS conditions.[84, 230]

9.4 Phase Diagram for Lysozyme-HEPES System

We have experimentally characterized the temperature(T)-concentration(C_P) phase diagram for our initial lysozyme-HEPES system at NaCl 0.15 M. This is illustrated in Fig. 9.5. The LLPS boundary was determined by using our cloud-point results (solid circles). The LLPS boundary obtained for the reference system, which is located at higher temperatures, is shown for comparison (open circles). The solubility of the globular microparticles was also characterized by measuring the equilibrium protein concentration in the supernatant of heterogeneous samples as a function of temperature. Solubility data, which are included in Fig. 9.5 (diamonds), show that the solubility of microparticles increases with temperature, with a sharp rise occurring above 40 °C. This is consistent with samples becoming transparent at 50 °C within our experimental range of protein concentrations. Relatively large rod-shaped crystals were observed by light microscopy in several samples containing microparticles at T ≈ 40 °C and above. In these cases, measured solubility values were disregarded. Contrary to globular microparticles, these crystals do not fully dissolve at 50 °C.

Solubility of rod-shaped orthorhombic crystals was also characterized to compare their thermodynamic stability with that of microparticles. The corresponding solubility curve is also

shown in Fig 9.5 (triangles). To determine these solubility data, heterogenous samples were first taken to 50 °C to dissolve microparticles and then incubated at 4 °C, well above the clouding temperatures in Fig 9.5, in order to amplify crystal formation. Crystals were then added to a protein-free HEPES medium and the supernatant concentration was measured as a function of temperature after equilibration. In Fig 9.5, we can see that the two solubility curves intersect at ≈ 40 °C with protein microparticles being thermodynamically more stable than rod-shaped crystals at lower temperatures. This solubility inversion, which is known to occur between orthogonal and orthorhombic crystals,[226-228] further indicates the tetragonal-crystal properties of lysozyme microparticles.

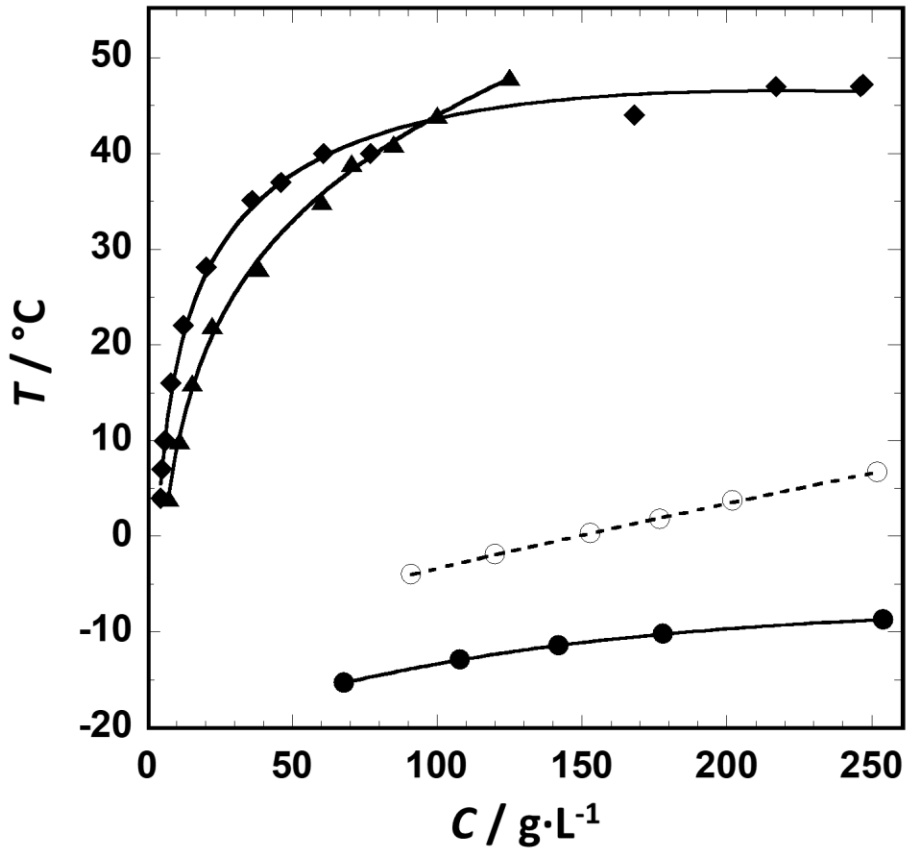

Figure 9.5 Temperature(T)-concentration(C_P) phase diagram of lysozyme-HEPES (0.10 M)-NaCl (0.15 M)-water system at pH 7.4 showing LLPS boundary (cloud points, solid circles) and solubility boundaries of protein microparticles (solid diamonds) and rod-like crystals (solid triangles). For comparison, the reversible LLPS boundary (open circles) of the reference system is included. All curves are guides for the eye.

9.5 Dynamic Light Scattering Analysis

Our phase-separation studies demonstrate that HEPES radically changes the fate of phase separation in lysozyme aqueous mixtures. From a molecular point of view, condensation of proteins is driven by a protein-protein net attraction energy in the aqueous medium. In some cases, phase separation may also involve the formation of mesoscopic clusters or intermediate soluble oligomers.[64, 231] Oligomerization is, for example, observed in the case of βB1-crystallins, where related LLPS leads to the formation of gel-like protein condensates.[64] Thus, we used dynamic light scattering (DLS) to probe both protein-protein interactions and protein aggregation in solution.[64] Specifically, we have characterized lysozyme-HEPES mixtures at 25 °C with protein concentrations as high as C_P = 20 g·L^{-1}.

All light-scattering distributions are monomodal and kinetically stable. This implies that no aggregate or clustering process occurs in these homogeneous mixtures. To characterize protein-protein interactions, we used our DLS distributions to extract the protein diffusion coefficient, D, as a function of protein concentration, C_P, and compare the experimental behavior of $D(C_P)$ with that associated with the reference system. Related data are shown in Fig. 9.6. Our $D(C_P)$ data can be examined according to the linear relation:

$$D = D_0\left(1 + k\phi_P\right) \tag{9.1}$$

where D_0 is the protein-tracer diffusion coefficient, related to the protein hydrodynamic radius (R_h), k is a unitless normalized slope with its value predicted to decrease as protein-protein attraction increases,[196, 232] and the protein volume fraction, $\phi_P = C_P V_P$, was calculated using the lysozyme specific volume[135] of V_P = 0.713 cm^3·g^{-1} (see section 3.2 of Chapter 3). Our results show an appreciable decrease in the k value from the HEPES to the reference case, thereby implying

that protein-protein attractive interactions become weaker in the presence of HEPES. This finding is consistent with the positions of the two LLPS boundaries in Fig. 9.5, where we can see that lower temperatures are needed to induce clouding in the HEPES case. To further corroborate this result, we performed DLS studies on lysozyme aqueous mixtures in which HEPES concentration was raised to 0.40 M at the same pH and ionic strength of the other two systems. Here, no NaCl is added since HEPES contribution to ionic strength is already 0.20 M. As we can appreciate in Fig. 9.6, a significant increase in the *k* value was observed, indicating a further weakening of protein-protein attraction. Consistent with these results, we notice that sample clouding of lysozyme in

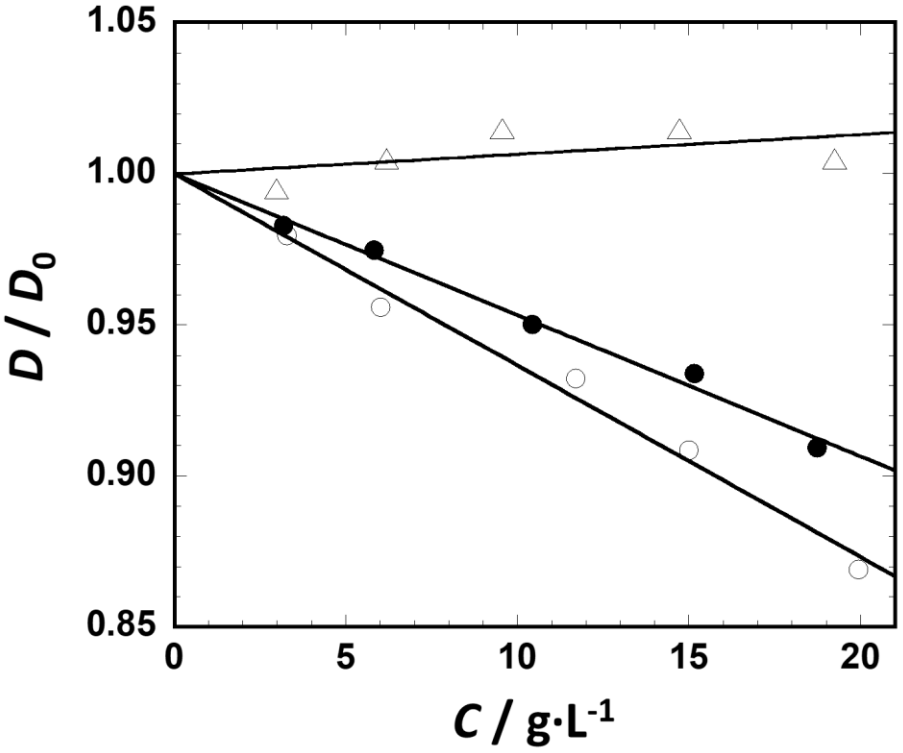

Figure 9.6 Protein diffusion coefficient ratio, D/D_0, as a function of its concentration, C_P, at 25 °C for lysozyme-HEPES (solid circles, η_r = 1.090, R_h =1.84 ± 0.01 nm, k = -6.5 ± 0.4), reference system (open circles, η_r = 1.019, R_h = 1.90 ± 0.01 nm, k = -8.9 ± 0.6) and lysozyme in HEPES 0.40 M (open triangles, η_r =1.317, R_h = 1.85 ± 0.01 nm, k = 0.9 ± 0.9). In parenthesis, η_r is the relative viscosity of the protein-free aqueous mixtures (values measured in this work). Lines are linear fits through the data based on Eq. 9.1. The protein tracer-diffusion coefficient, D_0, was converted into the corresponding hydrodynamic radius, R_h, using the Stokes-Einstein equation and the measured values of η_r.

0.40 M HEPES mixtures does not occur by cooling within the accessible temperature range and protein concentrations as high as C_P = 250 g·L^{-1}. This analysis further demonstrates that HEPES reduces protein-protein attractive interactions.

9.6 Preferential Binding Analysis

A reduction of protein-protein attractive interactions may be related to preferential binding of HEPES to lysozyme in aqueous solution. According to preferential-interaction theory,[233] an accumulation of additive molecules near protein surface (preferential binding) is predicted to enhance protein solubility. If this is the case, then HEPES is expected to accumulate near lysozyme surface. This effect may result in a corresponding accumulation of HEPES in a protein-rich phase. To examine this hypothesis, we quenched lysozyme-HEPES samples with C_P = 200 g·L^{-1} at -10 °C and characterized HEPES concentration in the supernatant after several incubation times. We

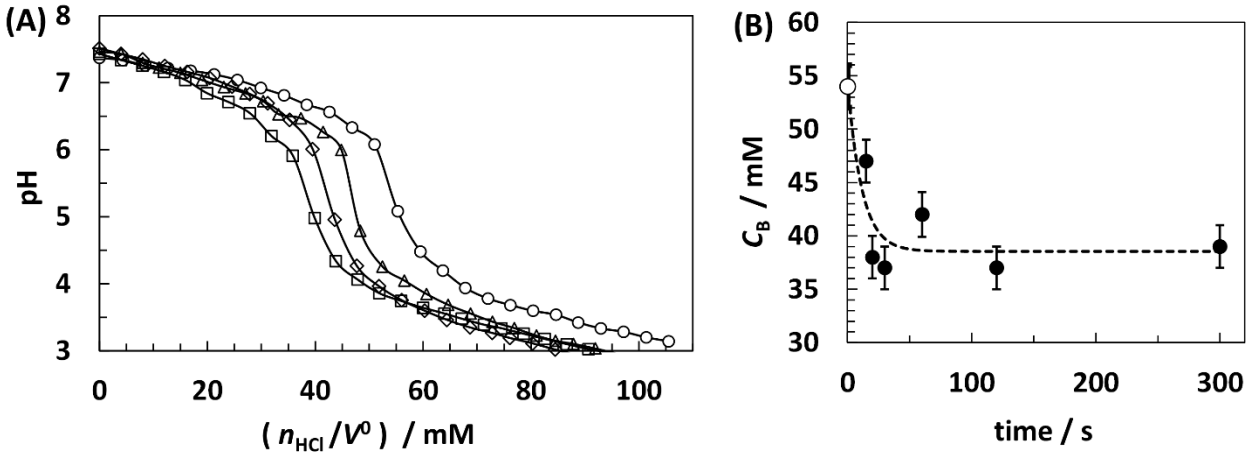

Figure 9.7 (A) Representative hydrogen-ion titrations of HEPES basic form: pH as a function n_{HCl}/V^0, where n_{HCl} is the number of HCl added moles (titrant) and V^0=250 μL is the initial volume of titrand. The reference titrand is a 0.10 M HEPES solution at pH 7.4 with NaCl 0.15 M (circles). The other titrands are supernatant solutions extracted after quenching lysozyme-HEPES mixtures at -10 °C with C_P = 200 g·L^{-1}, followed by an incubation time of 15 s (triangles), 60 s (diamonds) and 300 s (squares) and lysozyme removal by ultrafiltration. (B) Concentration of HEPES basic form, C_B, determined from the inflection point of titration plots. Values extracted for the reference titrand (open circle) and as a function of incubation time (solid circles). The dashed curve is an exponential fit through the data describing a 29±6% decrease in the value of C_B. Error bars are uncertainties on the titration inflection points based on the spacing between adjacent titration data points.

specifically performed hydrogen-ion titrations (similar to those shown in Chapter 6) to determine the concentration of HEPES basic form (after protein removal by ultrafiltration). In all cases, the pH of the supernatant is found to be 7.4. This implies that the ratio between HEPES acidic and basic forms remains the same. Our results are illustrated in Fig. 9.7. We find that the concentration of HEPES is about 30% lower with respect to that of our initial HEPES buffer. We therefore conclude that HEPES accumulates in the protein-rich phase.

9.7 Isothermal Titration Calorimetry Analysis

To further characterize lysozyme-HEPES interactions, isothermal titration calorimetry (ITC) was employed at 25 °C.[208, 234] Specifically, we added a HEPES solution (0.18 M, titrant) to a HEPES-free lysozyme solution (titrand). In these experiments, the titrand was prepared by ultrafiltration at pH 5.4 and NaCl 0.20 M. The corresponding filtrate, in which neutral HEPES was then added, is employed as "solvent" for the titrant in order to minimize changes in interstitial composition. To disregard calorimetric effects related to protein-protein interaction, lysozyme concentration was set to be 0.50 mM (C_P = 7.15 g·L^{-1}). At this low concentration, filtrate additions to titrand produce negligible heat of mixing. In this experiment, we chose pH 5.4 to ensure that the neutral acidic form of HEPES dominates and contribution of proton donation from positively charged lysozyme to the negative basic form of HEPES is negligible in ITC diagrams. It is important to note that our turbidity experiments showed that opacification behavior of lysozyme-HEPES is not qualitatively altered by this pH change.

Our ITC results are shown in Fig. 9.8. In Fig. 9.8A, we can see that additions of HEPES titrant to lysozyme-free filtrate produce a significant endothermic heat of dilution. This contribution was therefore subtracted from the heat values of the lysozyme-HEPES titration also shown in Fig. 9.8A. The difference between the two sets of data, which is shown in Fig. 9.8B,

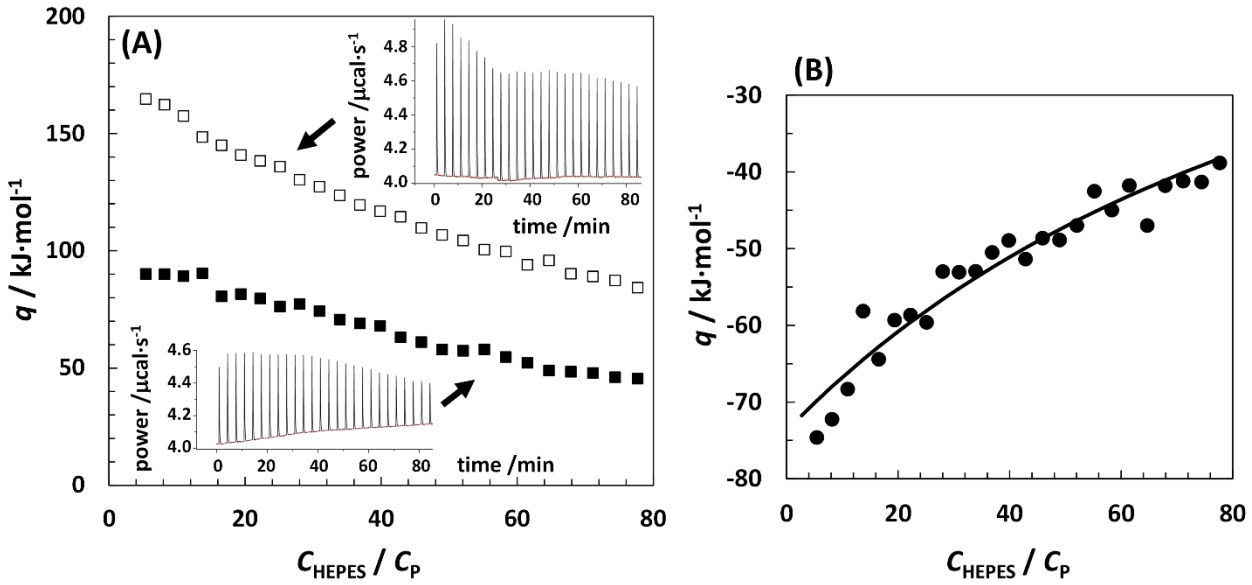

Figure 9.8 (A) Differential heat per mole of HEPES, *q*, associated with consecutive injections of titrant solution (HEPES, 180 mM; NaCl, 0.20 M; pH 5.4) into titrand solution (lysozyme, 0.50 mM; NaCl, 0.20 M; pH 5.4) as a function of the HEPES-to-lysozyme molar concentration ratio after injection, C_{HEPES}/C_P, at 25 °C (solid squares). Values of differential heat associated with injections of titrant solution into lysozyme-free filtrate (NaCl, 0.20 M; pH 5.4) are also included (open squares). The two insets show the corresponding plots of power as a function of time for these titrations. (B) Values of *q* calculated after subtracting HEPES heat of dilution from the heat values associated with titrant addition to lysozyme titrand. The solid curve is a fit through the data based on the ligand-binding model with identical and independent sites.

reveals lysozyme-HEPES exothermic interactions. Note that ITC data in Fig. 9.8B lack of the inflection point characteristic of significant host-guest binding.[208, 211] This is indicative of a weak physical attractive interaction. Nonetheless, we can still apply the ligand-binding model[211] with identical and independent sites to our data. Our analysis yields a large value of equilibrium dissociation constant (≈0.2 M), as expected for weak attractive interactions. Due to lack of inflection point, the corresponding value of the binding enthalpy, ΔH, could not be unambiguously determined because it strongly correlates with the number of binding sites, *n*, with $n \cdot \Delta H \approx -30$ kJ·mol^{-1}.

9.8 Concluding Remarks

The results presented in this chapter show that LLPS acts as a template for the formation of globular compact protein microparticles with crystalline properties. These are thermodynamically more stable than relatively large rod-shaped orthorhombic crystals at temperatures lower than ≈ 40 °C. We also found that LLPS temperature increases in the presence of HEPES, the slope of lysozyme $D(C_P)$ increases with HEPES concentration, HEPES concentration is depleted in the supernatant and lysozyme-HEPES interactions are exothermic. These results demonstrate that lysozyme-HEPES interactions are weakly attractive. Thus, the accumulation of additives near protein surface, driven by weakly attractive forces, appears to have a large impact on the kinetic evolution of the metastable protein-rich liquid phase. These results suggests that, under LLPS conditions, additives exhibiting weak ligand properties represent an important tool for controlling the fate of protein-rich liquid micro-droplets. Thus, this strategy may be exploited for the preparation of protein-based materials and even the production of a large number of protein microcrystals with potential applications to femtosecond crystallography. Finally, many small biological molecules inside cytoplasm may play a similar role in the formation protein-driven micro-compartments inside living cells. In Chapter 10, we shall extend these LLPS studies to lysozyme aqueous mixtures in the presence of several additives sharing similar chemical structure with HEPES. This allows us to explore the molecular basis responsible for the phase behavior of lysozyme aqueous mixtures observed in the presence of HEPES.

Chapter 10

Effect of Other Additives on the Phase Behavior of Lysozyme Aqueous Mixtures

10.1 Introduction

In this chapter, the role of HEPES chemical structure in determining the observed complex phase behavior of lysozyme-HEPES systems is investigated. The chemical structure of HEPES protonated (acidic) and deprotonated (basic) forms are shown in Fig. 10.1.[235] The pK_a of HEPES is 7.5[236] and moderate changes of pH make its one form dominant as compared to the other. For example, it mainly (≈ 90%) exists as a protonated species (acidic) at pH 6.6, approximately an equal mixture of both protonated (≈ 55%) and deprotonated (≈ 45%) species (buffer) at the physiological pH of 7.4, and mainly (≈ 90%) as a deprotonated species (basic) at pH 8.4.

The first question that needs to be addressed is whether only one of the two HEPES forms is responsible for the observed phase behavior. For example, the acidic species of HEPES might act as an electrostatic crosslinker due to their zwitterionic nature thereby stabilizing protein

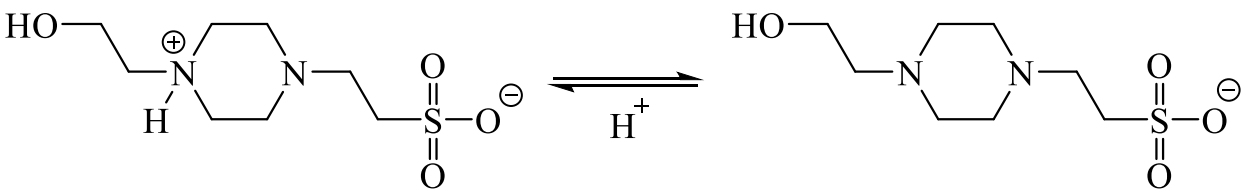

Figure 10.1 Protonated and deprotonated species of HEPES buffer (pK_a = 7.5).

clusters. On the other hand, since the basic form is negatively charged, it might more strongly bind to positively charged lysozyme. To examine the effect of HEPES protonation state on lysozyme phase behavior, we performed LLPS studies at pH 6.8 (acidic species dominant) and 8.4 (basic species dominant). The obtained results will be compared with the studies at pH 7.4 discussed in Chapter 9. If the HEPES protonation state is important then, LLPS studies should show a significant change in the LLPS behavior. For example, one of the two chosen pH cases may show the normal LLPS behavior that is observed in the lysozyme reference system.

To understand the chemical basis responsible for lysozyme-HEPES phase behavior, we investigated other additives which share chemical similarities with HEPES. These additives were selected based on the HEPES chemical structure. Figure 10.2 identifies various chemical blocks constituting HEPES along with their names mentioned in this chapter. Specifically, HEPES is characterized by a central piperazine core attached to a hydroxyl-terminated alkyl chain (left) and a sulfonate-terminated alkyl chain. It may be hypothesized that the sulfonate group may interact electrostatically with positively charged residues on the protein surface while the positively charged piperazine ring (see the acidic form in Fig 10.1) may interact with the carboxylate group on the surface of another protein. Similar effects may be also expected from the hydroxyl group or any combination of these building blocks.

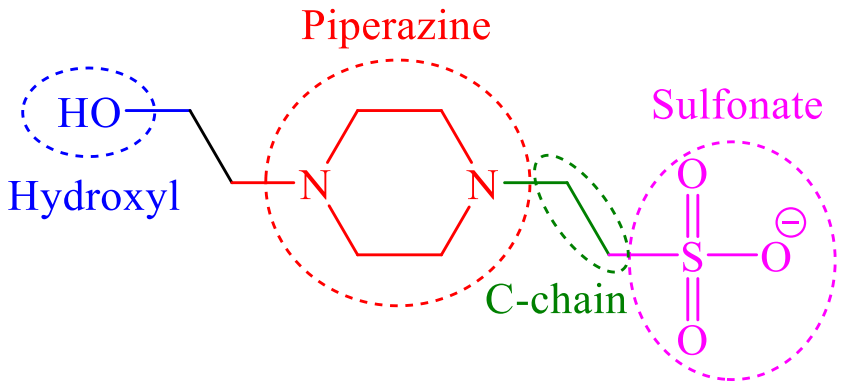

Figure 10.2 Names of different building blocks of HEPES used in this chapter.

We identified several commercially-available compounds with a chemical structure similar to HEPES or specifically containing the HEPES building blocks illustrated in Fig. 10.2. We then experimentally characterized the LLPS behavior of lysozyme aqueous mixtures in the presence of these additives at pH 7.4 and the same ionic strength of 0.20 M.

The main experimental method employed in this investigation is the turbidity method. This has allowed us to 1) determine the LLPS boundary through sample cooling and 2) assess clarification properties through sample heating after phase separation. Light microscopy was also employed to characterize the size and morphology of protein condensates. These methods were discussed in Chapter 8.

10.2 The Role of HEPES Protonation State

To characterize the effect of HEPES protonation states on LLPS of lysozyme-HEPES system, we performed turbidity studies at pH 6.6 and 8.4. These results were compared with turbidity studies at pH 7.4. In all cases, the total concentration of HEPES was set to be 0.10 M. To ensure that electrostatic effects coming from ions is the same in all three cases, these systems share the same ionic strength of 0.20 M. This required to use slightly different concentrations of NaCl, 0.19M, 0.15M, and 0.11M in the mixtures having pH 6.6, 7.4, and 8.4, respectively.

Due to pH variation, it is important to also examine lysozyme electrostatic properties as a function of pH. Lysozyme has a different protonation state (ν_H, see Chapter 1) at these pHs. According to Kuehner *et. al.*,[101] we have $\nu_H = 8.0$ at pH 6.6, $\nu_H = 7.5$ at pH 7.4, and $\nu_H = 6.8$ at pH 8.4. If we neglect ion binding, these parameters can be taken as the protein charge. Since protein charge decreases as pH increases toward lysozyme isoelectric point (pI = 11.35)[97], we expect that protein-protein electrostatic repulsion decreases as pH increases. This implies that protein-protein

van-der-Waals attractive interactions become relatively more important as pH increases (see the DLVO model in Chapter 7). This allows us to predict, based on the DLVO model, that the LLPS temperature of lysozyme aqueous mixtures should increase as pH increases at constant ionic strength (and protein concentration).

Figure 10.3 shows the representative turbidity profiles of lysozyme-HEPES mixtures obtained using two representative concentrations of lysozyme, namely 250 g/L and 120g/L at these investigated pHs. We can see that all turbidity profiles obtained for lysozyme-HEPES at pH 6.6 and 8.4 show the same behavior as that obtained at pH 7.4 and already discussed in Chapter 9. In all three cases, LLPS leads to the formation of a large number of protein microparticles which remain stable at room temperature. This indicates that the HEPES protonation state does not qualitatively alter the behavior of turbidity profiles discussed in Chapter 9.

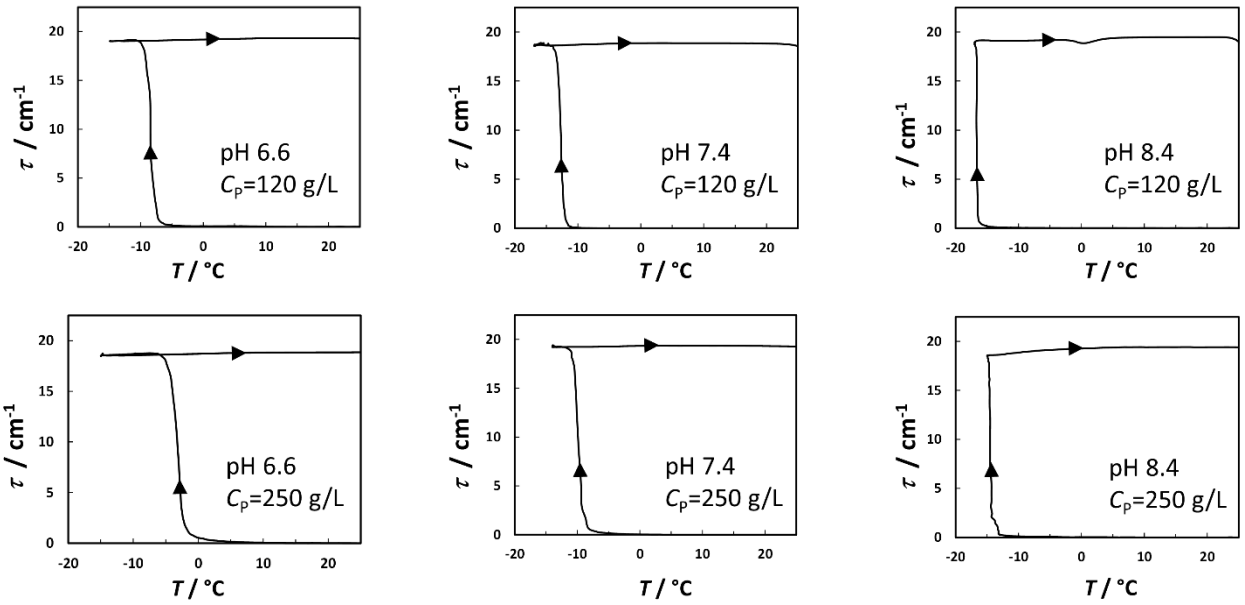

Figure 10.3 Representative temperature (*T*)-turbidity (τ) profiles for Lysozyme-HEPES systems (HEPES 0.10 M; Ionic Strength 0.20 M) at C_P = 120 (top row) and 250 g/L (bottom row) and three different pH 6.6 (left column), 7.4 (middle column) and 8.4 (right column). Qualitatively, the turbidity profiles remain unaltered with a change in pH.

While the turbidity profiles exhibit the same pattern independent of investigated pH, the LLPS temperature values determined from the turbidity profiles (see Chapter 8) depend on pH. Figure 10.4 shows the LLPS boundaries of the lysozyme-HEPES system obtained at the three studied pHs. Here we can see that the LLPS boundary shifts toward lower temperatures as pH increases. This behavior is in disagreement with the DLVO model (see Chapter 7), which predicts that the LLPS boundary should shift toward higher temperatures as the protein charge decreases at constant ionic strength. To explain our findings, we observe that NaCl concentration decreases from 0.19 M to 0.11 M as pH increases from 6.6 to 8.4. Thus, the observed LLPS shift toward lower temperatures can be related to a corresponding decrease in NaCl concentration. This implies that NaCl not only plays the role of ionic strength adjustor but it also behaves as a salting-out agent. In other words, both lysozyme and NaCl preferentially interact with water. This leads to

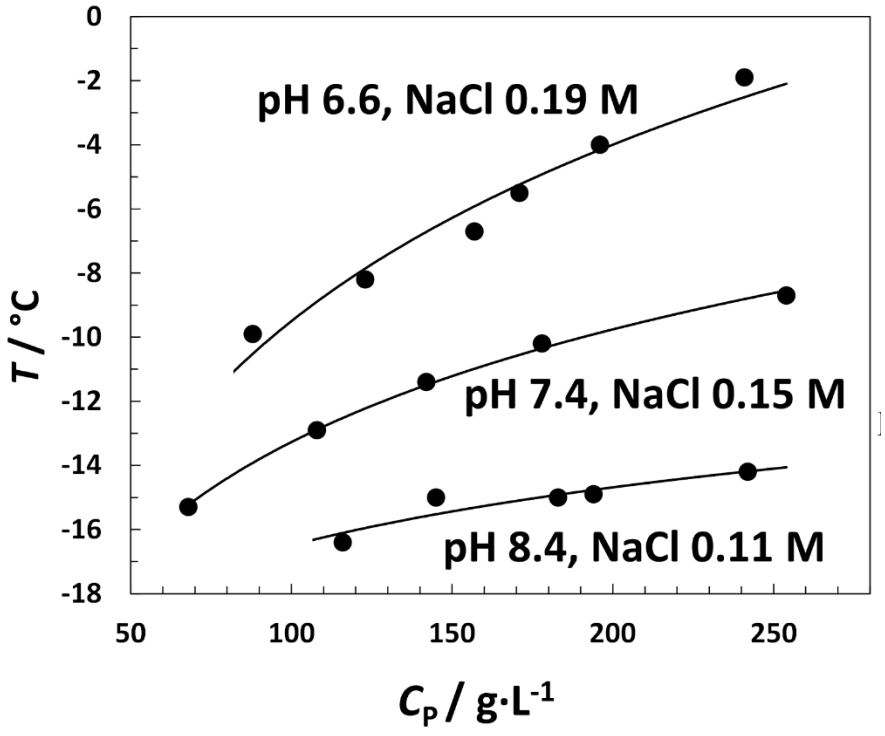

Figure 10.4 Temperature (T)-concentration (C_P) LLPS boundaries of the Lysozyme-HEPES systems (HEPES 0.10 M; Ionic Strength 0.20 M) at pH 6.6, 7.4, and 8.4. An increase in pH lowers the phase separation temperature.

lysozyme-NaCl net repulsive interactions favoring protein phase separation even at these relatively low NaCl concentrations (< 0.20 M). Our results underline some limitations of the DLVO model.

Figure 10.5 shows the microscopic images of the sample after phase-separation at different pHs. The particles have nearly similar morphologies at pH 6.6 and 7.4. However, the micro-crystalline particles observed at pH 8.4 are slightly larger and with a more evident tetragonal morphology,[229] as can be seen in the image.

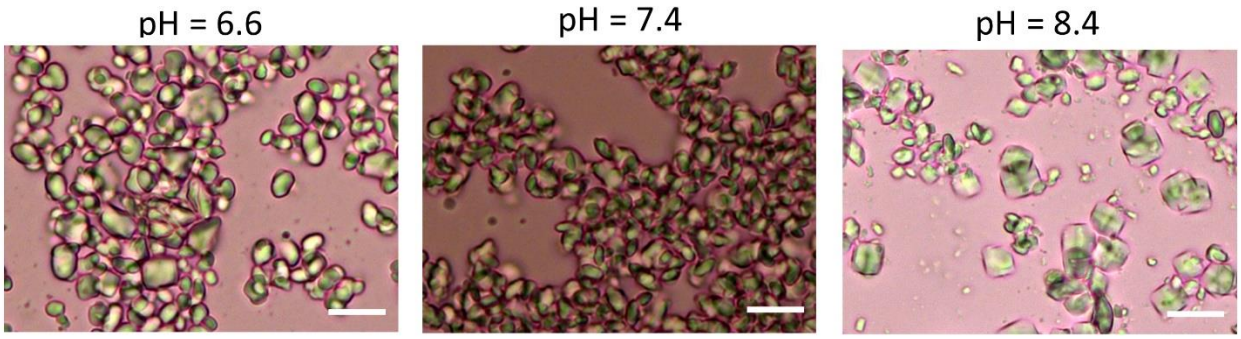

Figure 10.5 Direct-field light microscopy images taken at room temperature showing the effect of pH on Lysozyme-HEPES systems (HEPES 0.10 M; Ionic Strength 0.20 M) using C_P = 120 g/L. Particles have nearly similar morphologies at pH 6.6 and 7.4. However, particles at pH 8.4 appear large provided lower LLPS temperature at this working pH. The horizontal bar is 10μm in all cases.

In summary, our results show that the protonation state of HEPES has a marginal effect on the phase behavior of lysozyme aqueous mixtures.

10.3 The Lysozyme-HEPPS System

To explore the molecular basis responsible for lysozyme-HEPES phase behavior we consider an additive that has a chemical structure just slightly different HEPES. We specifically consider the molecule: 4-(2-Hydroxyethyl)-1-piperazinepropanesulfonic acid (HEPPS) which is also a known Good's buffer containing just one extra methylene group on the C-chain shown in Fig 10.2. This small increase in the alkyl chain leads to an increase in the pK_a value (pK_a = 8.1).[236] Figure 10.6 illustrates the structure of protonated and deprotonated species of HEPPS.[235] In terms of additive

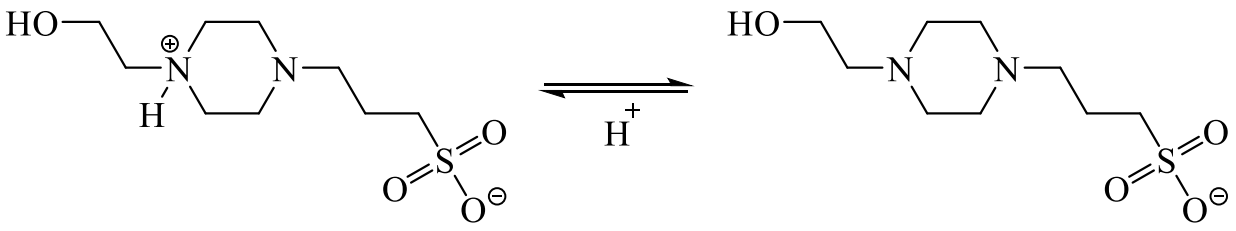

Figure 10.6 Protonated and deprotonated species of HEPPS buffer (pK_a = 8.1).

protonation state, the lysozyme-HEPPS system at pH 7.4 resembles the lysozyme-HEPES system at pH 6.6. Correspondingly, they also share nearly the same concentration of NaCl (0.19 M in HEPES *vs* 0.18 M in HEPPS) at the constant ionic strength of 0.2 M.

Figure 10.7 shows the representative turbidity profiles of lysozyme-HEPPS mixtures at the two representative concentrations of lysozyme, 250 g/L, and 120g/L at pH 7.4. We can see that the turbidity cooling profiles of the lysozyme-HEPPS systems show clouding induced by lowering temperature due to LLPS. The corresponding heating profiles show that turbidity remains high at temperatures 5-10 °C above the LLPS temperature followed by a significant increase in sample clarification. This turbidity behavior characterizes the formation of a relatively small amount of

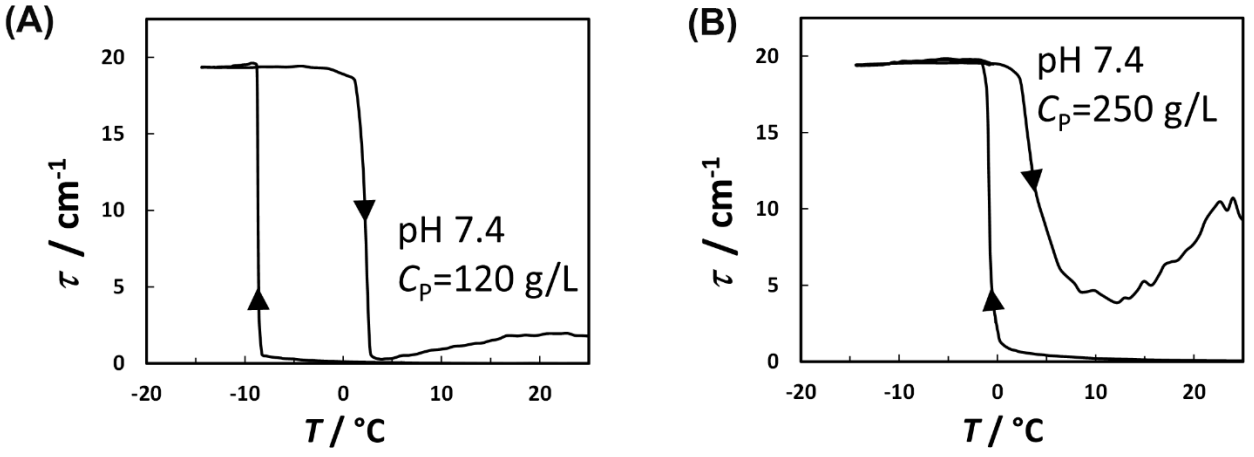

Figure 10.7 Representative temperature (*T*)-turbidity (τ) profiles for Lysozyme-HEPPS systems (HEPPS 0.10 M; pH 7.4, Ionic Strength 0.20 M; NaCl 0.18 M), lysozyme concentration (C_P) (A) 120 and (B) 250 g/L. Qualitatively, these systems also exhibits unusual LLPS behaviour following the pattern of HEPES system.

protein particles compared to the lysozyme-HEPES system. Visual inspections of these lysozyme-HEPPS samples at room temperature reveal the presence of just a small amount of protein precipitates near the bottom of the test tubes. On the other hand, it is important to remember that lysozyme-HEPES samples appear to be completely opaque under the same experimental conditions.

The protein precipitates generated from the lysozyme-HEPPS system were inspected by light microscopy. Figure 10.8 shows the precipitates taken from a sample at C_P = 120 g/L. We can see that the size of these particles (about 15 μm) is significantly larger than that observed in the HEPES case (see Fig. 10.5). Furthermore, these particles exhibit clear crystalline traits and a square-like morphology characteristic of lysozyme tetragonal crystals.

Figure 10.9 compares the LLPS boundary of the lysozyme-HEPPS system with that of the reference system (see Chapter 9), the lysozyme-HEPES system at pH 7.4 (same pH). We can see

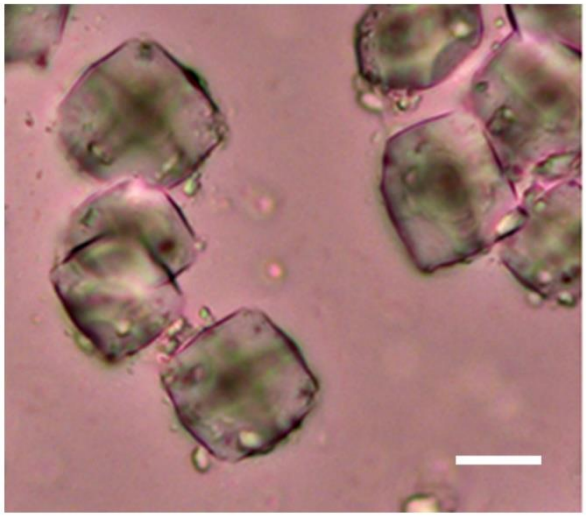

Figure 10.8 Direct-field light microscopy images of phase-separated particles of Lysozyme-HEPPS system (HEPPS 0.10 M; pH 7.4, Ionic Strength 0.20 M; NaCl 0.18 M), taken at room temperature using lysozyme concentration C_P = 120 g/L. The horizontal bar is 10 μm.

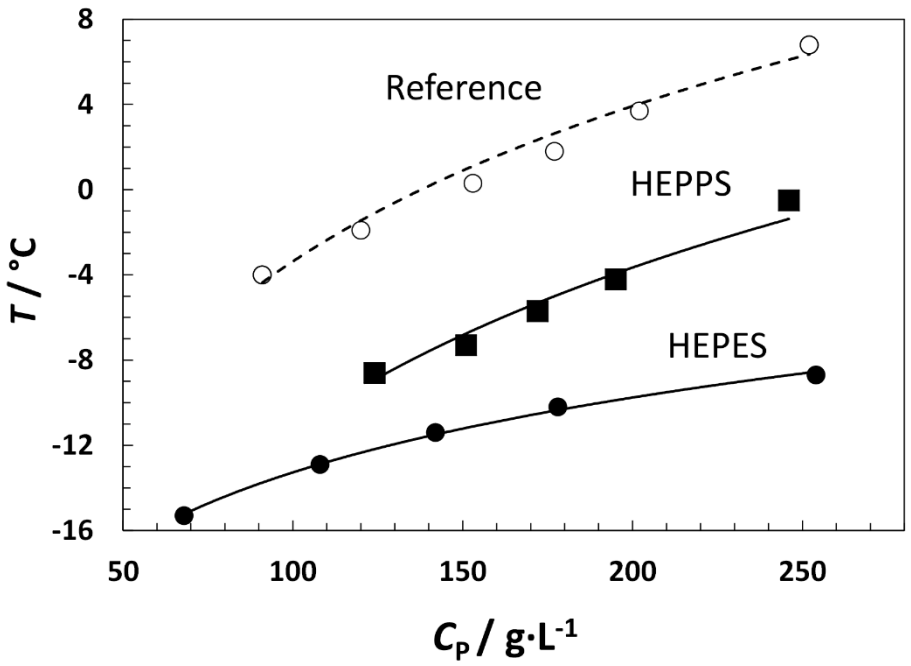

Figure 10.9 Temperature (T)-concentration (C_P) LLPS boundaries of the Lysozyme reference system, Lysozyme-HEPES system (HEPES 0.10 M; pH 7.4, Ionic Strength 0.20 M, NaCl 0.15 M) and Lysozyme-HEPPS system (HEPPS 0.10 M; pH 7.4, Ionic Strength 0.20 M; NaCl 0.18 M).

that the lysozyme-HEPPS LLPS boundary is located at intermediate temperatures. This can be again explained by considering the corresponding NaCl concentration: 0.15 M for lysozyme-HEPES, and 0.18 M for lysozyme-HEPPS systems. Furthermore, a comparison of Fig. 10.9 with Fig. 10.4 shows that the lysozyme-HEPPS LLPS phase boundary is located at temperatures that are virtually the same as those obtained for the lysozyme-HEPES at pH 6.6 and NaCl 0.19 M. This result not only again correlates with NaCl concentration but also with the protonation state of HEPPS at pH 7.4 being the same as the protonation state of HEPES at pH 6.6.

This analysis allows us to conclude that the thermodynamic effect of HEPES and HEPPS on lysozyme are virtually the same. This is expected considering the large similarities between these two molecules. However, it is important to remark that the substitution of HEPES with HEPPS does have a significant effect on the kinetic evolution of LLPS. The observation of

significantly fewer and relatively larger protein micro-crystals in the case of HEPPS suggests that protein-rich droplets behave as a relatively weaker nucleation platform for protein microcrystals compared to the HEPES cases. In other words, fewer protein crystals nucleate. It is then possible that they may slowly grow larger in the presence of concomitant droplet growth and coagulation.

10.4 Role of Sulfonate-terminated Alkyl Chain

To examine the role of the sulfonate-terminated alkyl chain in the HEPES chemical structure (see Fig. 10.2), we investigated the phase behavior of lysozyme aqueous mixtures in the presence of two different additives. The first additive is 2-aminoethanesulfonic acid (taurine). At pH 7.4, taurine (pK_a = 9.0[237]) is a zwitterion as illustrated in Fig 10.10. Taurine was chosen as it is closely related to the sulfonate-terminated alkyl chain.

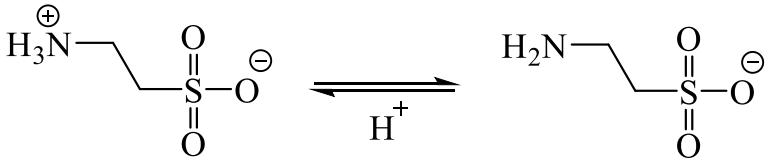

Figure 10.10 Protonated and deprotonated species of taurine (pK_a = 9.0).

The second investigated additive is the commercially-available 1,4-Piperazinediethanesulfonic acid (PIPES) (Fig. 10.11), another member of the Good's buffer family. PIPES was chosen because it not only contains the same sulfonate-terminated alkyl chain as HEPES but it also replaces the hydroxyl-terminated chain of HEPES with a second, identical

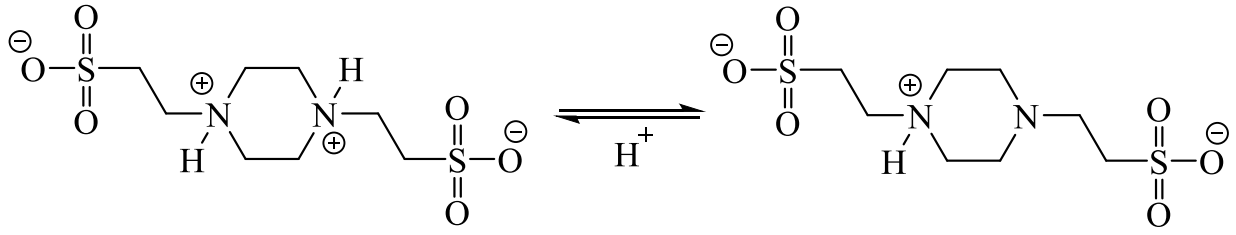

Figure 10.11 Protonated and deprotonated species of PIPES (pK_a = 6.8).

sulfonate-terminated alkyl chain. At pH 7.4, PIPES (pK_a = 6.8[236]) is negatively charged as illustrated in Fig 10.11. Both additives lack a hydroxyl-terminated alkyl chain. As in the previous cases, phase behavior studies were carried out at pH 7.4 and the ionic strength of 0.20 M. Since taurine lacks of buffer capacity at pH 7.4, 0.02M tris buffer was added in this case. To ensure an ionic strength of 0.20 M, NaCl was added with a concentration of 0.19M and 0.12M in the taurine and PIPES cases, respectively.

Figure 10.12 shows the representative turbidity profiles of lysozyme-Taurine and lysozyme-PIPES mixtures at the two representative concentrations of lysozyme, 250 g/L, and

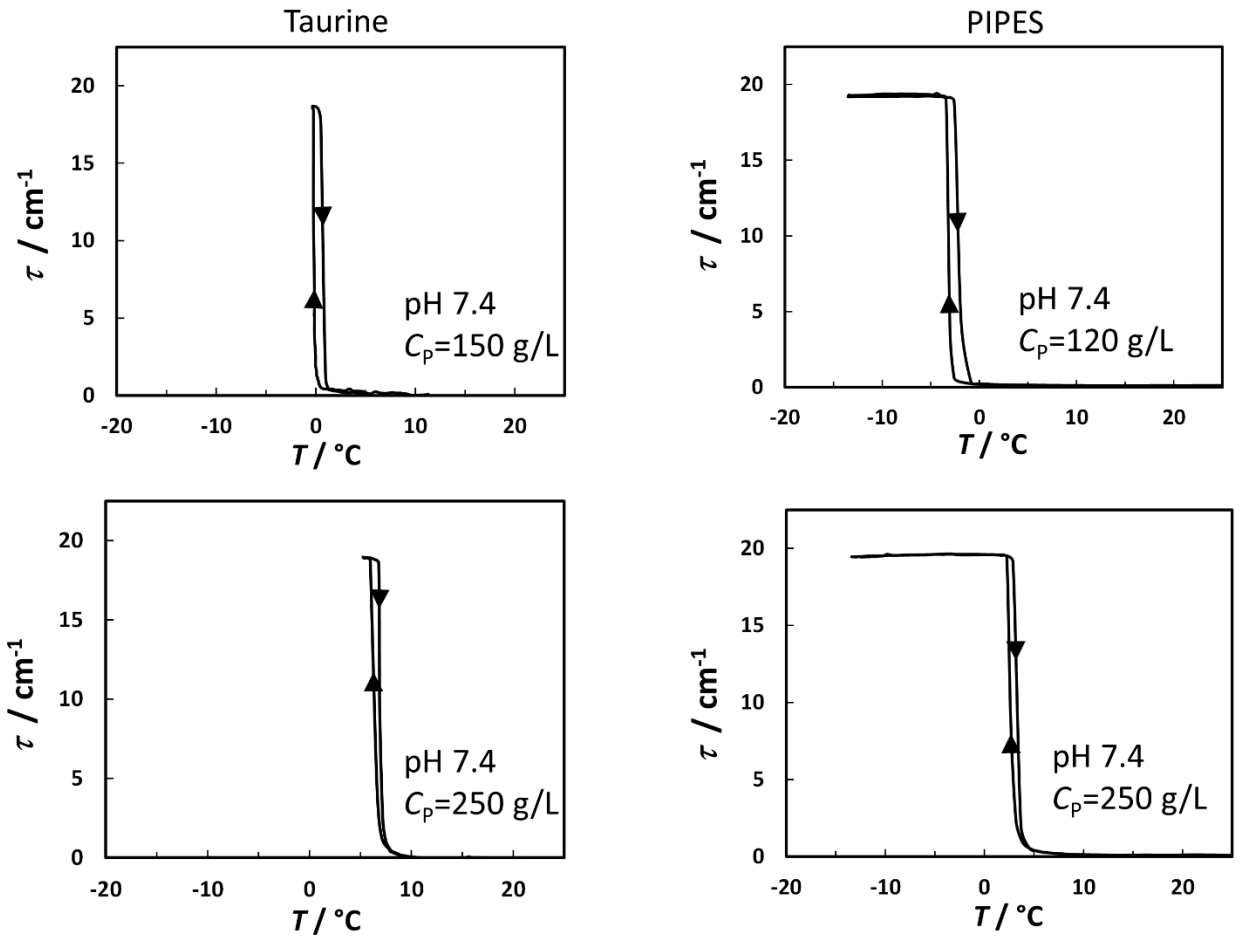

Figure 10.12 Representative temperature (T)-turbidity (τ) profiles for (Left column) Lysozyme-Taurine systems (Taurine 0.10 M; pH 7.4, Ionic Strength 0.20 M; NaCl 0.19 M; Tris 0.02 M) and (Right column) Lysozyme-PIPES systems (PIPES 0.10 M; pH 7.4, Ionic Strength 0.20 M; NaCl 0.12 M), (Top row) C_P = 120 g/L and (Bottom row) C_P = 250 g/L. Qualitatively, these systems also exhibits a typical normal LLPS behavior indicating negligible contribution of sulfate groups.

120g/L at pH 7.4. In all cases, LLPS is induced by cooling. Furthermore, the turbidity profiles were found to be highly reversible as in the case of the lysozyme reference system (see Chapter 9) This type of profile is characteristic of a normal LLPS behavior. The observed turbidity profiles indicate that the sulfonate component of HEPES does not play a central role in the complex phase behavior observed in the HEPES case.

Our turbidity profiles were then used to determine the corresponding LLPS temperatures. In Fig. 10.13, the LLPS boundaries for the lysozyme-Taurine and lysozyme-PIPES systems are shown. For comparison, the LLPS boundaries for the lysozyme-HEPES and the lysozyme reference system were also included. As it can be seen in Fig. 10.13, the LLPS boundary for the taurine case nearly overlaps with that for the reference case. Since these two systems also share

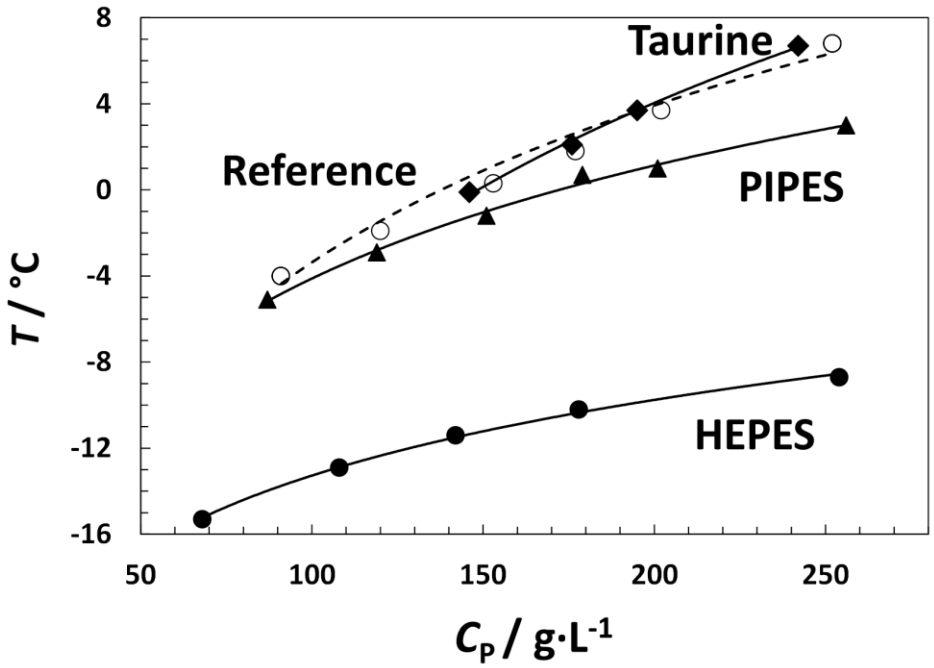

Figure 10.13 Temperature (T)-concentration (C_P) LLPS boundaries of the Lysozyme reference system, Lysozyme-Taurine systems (Taurine 0.10 M; pH 7.4, Ionic Strength 0.20 M; NaCl 0.19 M; Tris 0.02 M), Lysozyme-PIPES systems (PIPES 0.10 M; pH 7.4, Ionic Strength 0.20 M; NaCl 0.12 M) and Lysozyme-HEPES system (HEPES 0.10 M; pH 7.4, Ionic Strength 0.20 M; NaCl 0.15 M). The systems which lacks hydroxyl group and contains only the sulfate group are close to the reference system indicating minimal effects of the sulfonate groups.

nearly the same NaCl concentration, we conclude that taurine has no appreciable thermodynamic effect on lysozyme. The LLPS boundary for the PIPES case is located at slightly lower temperatures. This is consistent with a corresponding decrease in NaCl concentration and salting-out strength (0.12 M *vs* 0.19 M). In other words, also PIPES have no appreciable thermodynamic effect on lysozyme. On the other hand, it is important to remark that the LLPS boundary for the HEPES case is located at significantly lower temperatures even if its NaCl concentration (0.15 M) is higher than that associated with the lysozyme-PIPES system. This analysis further corroborates that the thermodynamic salting-in effect of HEPES plays an important role in the observed complex phase behavior and allows us to conclude that the sulfonate group plays a marginal role in the phase behavior observed in the Lysozyme-HEPES system.

10.5 Role of Hydroxyl-terminated Alkyl Chain and Piperazine Core

To examine the role of the hydroxyl-terminated alkyl chain and piperazine core of HEPES (see Fig. 10.2), we investigated the phase behavior of lysozyme aqueous mixtures in the presence of two other additives. The first additive is ethanolamine (or monoethanolamine, MEA). At pH 7.4, MEA (pK_a = 9.5[238]) is a cation as illustrated in Fig 10.14. MEA was chosen as it is closely related to the hydroxyl-terminated alkyl chain. The second investigated additive is 1-(2-hydroxyethyl)piperazine (HEP). Commercially-available HEP was chosen because it not only has the same hydroxyl-terminated alkyl chain as HEPES but it also contains the piperazine central

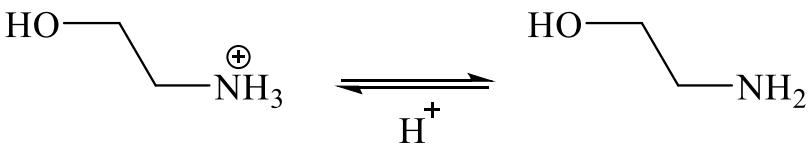

Figure 10.14 Protonated and deprotonated species of ethanolamine (MEA) (pK_a = 9.5).

core. At pH 7.4, HEP (pK_a = 9.1[239]) is also a cation as illustrated in Fig 10.15. Both additives lack a sulfonate-terminated alkyl chain.

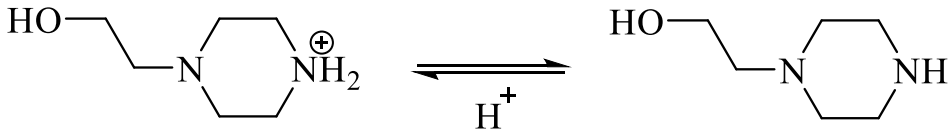

Figure 10.15 Protonated and deprotonated species of 1-(2-hydroxyethyl)piperazine (HEP) (pK_a = 9.1).

As in the previous cases, phase behavior studies were carried out at pH 7.4 and the ionic strength of 0.20 M. Since MEA and HEP lack buffer capacity at pH 7.4, 0.02 M tris buffer was added in both cases. To ensure an ionic strength of 0.20 M, NaCl with a concentration of 0.08 M was added in these two lysozyme systems containing already ionic additives.

Figure 10.16 shows the representative turbidity profiles of lysozyme-MEA and lysozyme-HEP mixtures at the two representative concentrations of lysozyme, 250 g/L, and 120g/L at pH 7.4. We can see that the turbidity cooling profiles for both systems show clouding induced by lowering temperature due to LLPS. The corresponding heating profiles show that a small residual turbidity persists at relatively high temperatures. This residual turbidity is small compared to that observed for the lysozyme-HEPPS system (see Fig. 10.7). It is also important to note that the high-concentration turbidity cooling profiles of MEA (Fig. 10.16) show turbidity fluctuations associable with crystal formation. This was not observed in the HEP case.

Visual inspections of these samples at room temperature reveal the presence of small amounts of protein precipitates near the bottom of the test tubes. The protein precipitates generated from the lysozyme-MEA and lysozyme-HEP systems were inspected by light microscopy. Figure 10.17 shows the precipitates taken from samples at C_P = 120 g/L.

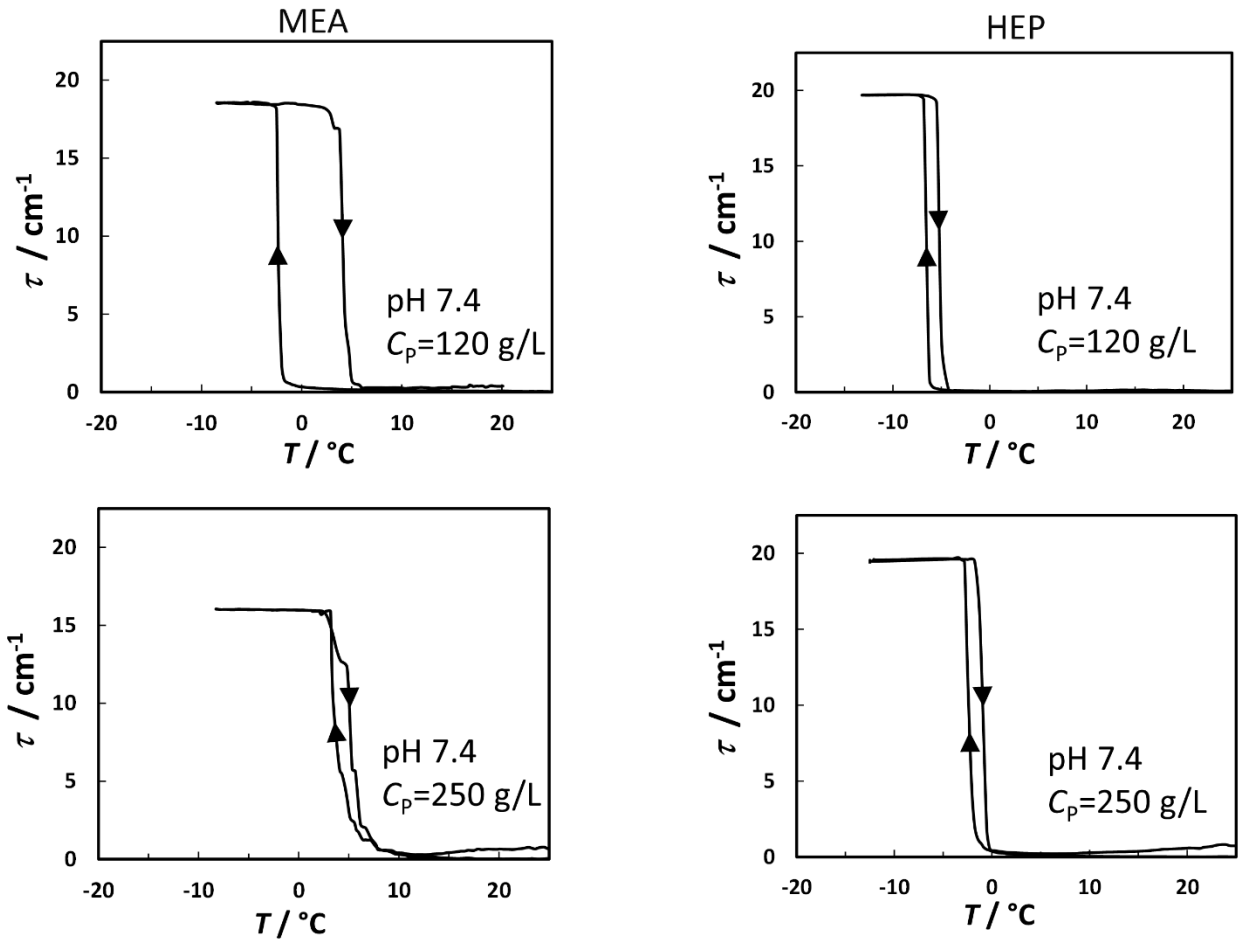

Figure 10.16 Representative temperature (*T*)-turbidity (τ) profiles for (Left column) Lysozyme-MEA systems (MEA 0.10 M; pH 7.4, Ionic Strength 0.20 M; NaCl 0.08 M; Tris 0.02 M) and (Right column) Lysozyme-HEP systems (HEP 0.10 M; pH 7.4, Ionic Strength 0.20 M; NaCl 0.08 M; Tris 0.02 M), (Top row) C_P = 120 g/L and (Bottom row) C_P = 250 g/L. Qualitatively, these systems demonstrate a normal LLPS behavior indicating negligible contribution of hydroxyl group.

In the MEA case, we observe prismatic microcrystals also characteristic of a tetragonal morphology. For comparison, we included lysozyme crystals generated from the reference system. As we can see from the figure, crystal shapes are the same. It is likely that lysozyme crystals are generated before LLPS consistent with the turbidity cooling profiles obtained in the case of this additive. On the other hand, in the HEP case, we observe small microparticles with crystalline traits similar to those obtained in the HEPES and HEPPS cases. Nonetheless, the number of

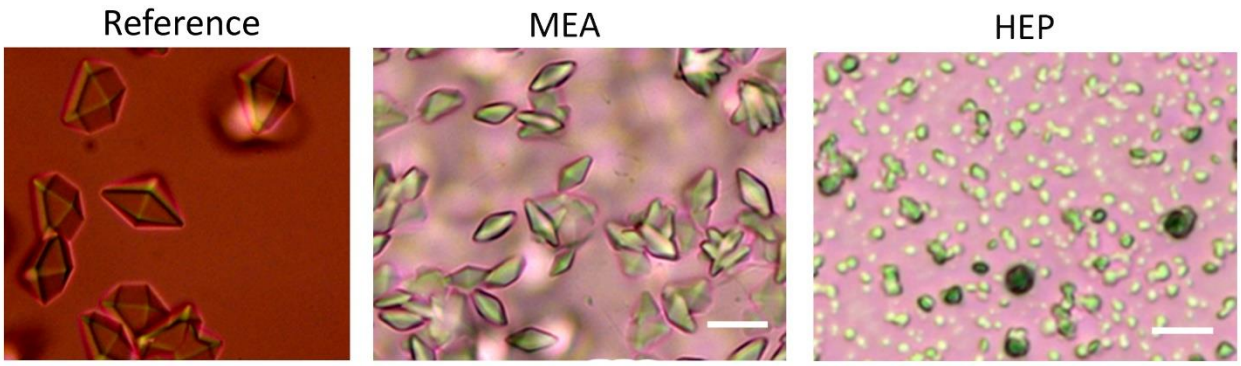

Figure 10.17 Direct-field light microscopy images of the sample after phase-separation, taken at 20 °C using lysozyme concentration C_P = 120 g/L at pH 7.4. The particles formed in Lysozyme-MEA system (Middle) resemble the particles formed in the reference system indicating that both systems have similar thermodynamic properties.

microparticles generated in the HEP case remains small compared to that generated in the HEPPS case and almost negligible compared to the HEPES case.

Turbidity profiles were then used to determine the corresponding LLPS temperatures. In Fig. 10.18, the LLPS boundaries for the lysozyme-MEA and lysozyme-HEP systems are shown. For comparison, the LLPS boundaries for the lysozyme-HEPES and the lysozyme reference system were also included. As it can be seen in Fig. 10.18, the LLPS boundary for the MEA case is located at slightly lower temperatures compared to the reference case. As in the PIPES case, this difference can be attributed to a corresponding difference in NaCl concentration and salting-out strength (0.08 M *vs* 0.19M). We, therefore, conclude that also the thermodynamic effect of MEA on lysozyme is marginal.

In Fig. 10.18, we can see that the LLPS boundary associated with the HEP case is located at relatively lower temperatures compared to that of the MEA case. Since both MEA and HEP share the same NaCl concentration, we deduce that HEP is a stronger salting-in agent compared to MEA. Nonetheless, the LLPS boundary for the HEPES case is still positioned at significantly

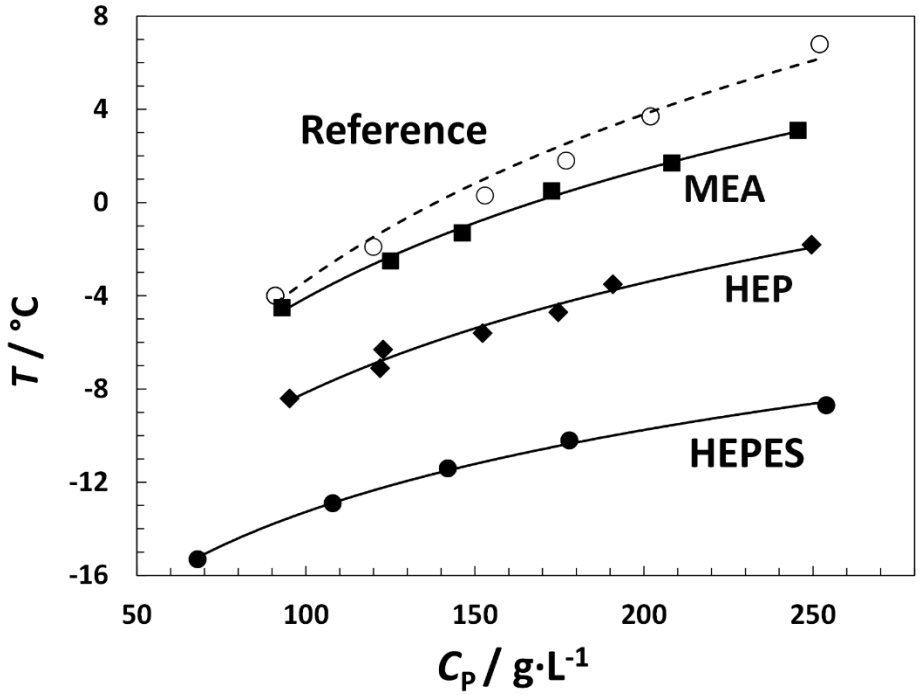

Figure 10.18 Temperature (T)-concentration (C_P) LLPS boundaries of Lysozyme reference system, Lysozyme-MEA systems (MEA 0.10 M; pH 7.4, Ionic Strength 0.20 M; NaCl 0.08 M; Tris 0.02 M), Lysozyme-HEP systems (HEP 0.10 M; pH 7.4, Ionic Strength 0.20 M; NaCl 0.08 M; Tris 0.02 M), and Lysozyme-HEPES system (HEPES 0.10 M; pH 7.4, Ionic Strength 0.20 M; NaCl 0.15 M). MEA shows the LLPS boundary close to the reference system indicating the similar thermodynamic effects.

lower temperatures even if its NaCl concentration is higher than that associated with the lysozyme-HEP system.

10.6 Summary and Conclusions

In summary, our experimental investigation shows that additions of HEPES leads to the production of a large number of protein microcrystals through LLPS. This complex phase behavior was observed to occur independently of HEPES protonation state near physiological pH. The small chemical variation achieved by replacing HEPES with HEPPS, while not producing appreciable changes in thermodynamic interactions, resulted in a major decrease in microparticle generation. The removal of the sulfonate-terminated alkyl group, achieved in the HEP case, is accompanied

by a reduction of salting-in interactions and a further decrease in microparticle generation with respect to the HEPES case. Our corresponding studies on sulfonated additives (Taurine and PIPES) and hydroxylated additive (MEA) show that the sulfonate-terminated alkyl group has negligible thermodynamic effects on lysozyme. Correspondingly these additives were unable to generate microparticles through LLPS. These studies allow us to deduce that significant salting-in interactions are necessary for the phase behavior observed in the LLPS case. It appears that all three chemical components in HEPES: Hydroxyl-terminated alkyl group, piperazine core, and sulfonate-terminated alkyl group are important as demonstrated by the comparison between HEPES and HEPPS. Our HEP studies suggest that the piperazine core plays a relatively more important role in lysozyme-HEPES interactions. However, since HEP is positively charged, HEP preferential binding to positively charged lysozyme may be hindered by electrostatic repulsive interactions. Based on this hypothesis, the role of the negatively-charged sulfonate group may be to enhance preferential binding by reducing electrostatic repulsion.

10.7 Future Directions

Due to the increased applications of lysozyme in materials such as bio-mineralization and nanotechnology (see Chapter 1), future work should be aimed to further investigate the effects of experimental conditions on controlling the sizes of lysozyme microcrystal by varying chemical nature of additives and LLPS temperature. For example, the role of other additives, e.g, those obtained by substitution of sulfonate group of HEPES with carboxylate or nitrate group, *etc*., should also be evaluated. Substitution of hydroxyl group with halogen atoms will further help to systematically quantify the role of electronegativity in the possible complex LLPS of lysozyme.

These studies may be also extended to more complex systems in which the LLPS-induced formation of lysozyme microparticles occurs in the presence of other colloidal particles or

macromolecules such as metal nanoparticles, other proteins or nucleic acids (e.g. RNA[240]). In these cases, a negative charge on the colloidal particles or macromolecule will favor electrostatic attractive interactions with positively charged lysozyme. This would lead to lysozyme droplets that are also enriched of the negatively charged colloidal particles or macromolecule, thereby leading to the formation of complex lysozyme-based materials with potential applications in medicine and materials science. These future directions are supported by previous studies on the encapsulation of metal nanoparticles in the lysozyme crystals and by literature reports which have established binding of lysozyme with RNA,[241] and DNA[240, 242]. The therapeutic applications of Lysozyme-RNA associations have been explored recently with a potential role in cell-repair or injury response pathways.[243] These LLPS studies can also be extended to those systems where lysozyme exhibits binding with the negatively charged residues of other proteins, such as ovomucin.[244, 245] It has been reported that the interactions between lysozyme and ovomucin are electrostatic in nature and strongly depend on ionic strength and pH of the medium[244, 245] making it an ideal case where LLPS studies under different experimental conditions will provide detailed insight into the binding. LLPS of lysozyme solutions may be investigated in the presence of negatively charged dendrimers due to their host-guest properties. Polyamidoamine (PAMAM) dendrimers, such as succinamic acid terminated PAMAM-SA dendrimer may be considered. Although lysozyme interactions with dendrimers have been studied using thermal[246] and spectroscopic-methods,[247] LLPS investigations of these systems have not been reported yet. Lysozyme-dendrimer aggregates with host-guest properties may be helpful in many biomedical applications, including drug and gene delivery, and imaging.[248]

These studies should also be extended to other commercially available proteins to explore generalizability. Especially to those proteins which do not exhibit LLPS in the experimentally

accessible temperature range. If a protein aqueous mixture does not show LLPS then crowding agents[249] such as polyethylene glycol[203, 221] can be used to induce this phase transition.

References

1. Haimovich, A. D.; Muir, P.; Isaacs, F. J., Genomes by design. *Nat. Rev. Genet.* **2015,** *16*, 501.
2. Jia, B.; Jeon, C. O., High-throughput recombinant protein expression in Escherichia coli: current status and future perspectives. *Open Biol.* **2016,** *6*, 160196.
3. Rodgers, K. R.; Chou, R. C., Therapeutic monoclonal antibodies and derivatives: Historical perspectives and future directions. *Biotechnol. Adv.* **2016,** *34*, 1149-1158.
4. Porter, J. L.; Rusli, R. A.; Ollis, D. L., Directed evolution of enzymes for industrial biocatalysis. *ChemBioChem* **2016,** *17*, 197-203.
5. Lin, C.-Y.; Liu, J. C., Modular protein domains: an engineering approach toward functional biomaterials. *Curr. Opin. Biotechnol.* **2016,** *40*, 56-63.
6. Roberts, D.; Keeling, R.; Tracka, M.; van der Walle, C. F.; Uddin, S.; Warwicker, J.; Curtis, R., The role of electrostatics in protein–protein interactions of a monoclonal antibody. *Mol. Pharm.* **2014,** *11*, 2475-2489.
7. Sorret, Lea L.; DeWinter, Madison A.; Schwartz, Daniel K.; Randolph, Theodore W., Challenges in predicting protein-protein interactions from measurements of molecular diffusivity. *Biophys. J.* **2016,** *111*, 1831-1842.
8. Sarkar, S.; Gulati, K.; Mishra, A.; Poluri, K. M., Protein nanocomposites: Special inferences to lysozyme based nanomaterials. *Int. J. Biol. Macromol.* **2020,** *151*, 467-482.
9. Baksi, A.; Xavier, P. L.; Chaudhari, K.; Goswami, N.; Pal, S. K.; Pradeep, T., Protein-encapsulated gold cluster aggregates: The case of lysozyme. *Nanoscale* **2013,** *5*, 2009-2016.
10. Das, S.; Pabba, M.; Dhushyandhun, M. E.; Patra, C. R., Theranostic applications of lysozyme-based nanoparticles. In *Nanoparticles in Medicine*, Shukla, A. K., Ed. Springer Singapore: Singapore, 2020; pp 1-23.
11. Kato, A.; Tanimoto, S.; Muraki, Y.; Kobayashi, K.; Kumagai, I., Structural and functional properties of hen egg-white lysozyme deamidated by protein engineering. *Biosci., Biotechnol., Biochem.* **1992,** *56*, 1424-1428.
12. Jollès, P., Lysozymes: A Chapter of molecular biology. *Angew. Chem. Int. Ed.* **1969,** *8*, 227-239.
13. Bekdemir, A.; Stellacci, F., A centrifugation-based physicochemical characterization method for the interaction between proteins and nanoparticles. *Nat. Commun.* **2016,** *7*, 13121.
14. Keurentjes, J. T. F.; Janssen, A. E. M.; Broek, A. P.; Van der Padt, A.; Wesselingh, J. A.; Van 'T Riet, K., Multicomponent diffusion in dialysis membranes. *Chem. Eng. Sci.* **1992,** *47*, 1963-1971.
15. Chayen, N. E.; Saridakis, E., Protein crystallization: from purified protein to diffraction-quality crystal. *Nat. Methods* **2008,** *5*, 147.
16. Zhang, J.; Wang, Y.; Wong, T. I.; Liu, X.; Zhou, X.; Liedberg, B., Electrofocusing-enhanced localized surface plasmon resonance biosensors. *Nanoscale* **2015,** *7*, 17244-17248.

17. Dey, K. K.; Das, S.; Poyton, M. F.; Sengupta, S.; Butler, P. J.; Cremer, P. S.; Sen, A., Chemotactic separation of enzymes. *ACS Nano* **2014,** *8*, 11941-11949.

18. Vagias, A.; Sergelen, K.; Koynov, K.; Košovan, P.; Dostalek, J.; Jonas, U.; Knoll, W.; Fytas, G., Diffusion and permeation of labeled IgG in grafted hydrogels. *Macromolecules* **2017,** *50*, 4770-4779.

19. Wesselingh, J. A., Controlling diffusion. *J. Control. Release* **1993,** *24*, 47-60.

20. Sochacki, K. A.; Shkel, I. A.; Record, M. T.; Weisshaar, J. C., Protein diffusion in the periplasm of E. coli under osmotic stress. *Biophys. J.* **2011,** *10*, 22-31.

21. Míguez, D. G.; Vanag, V. K.; Epstein, I. R., Fronts and pulses in an enzymatic reaction catalyzed by glucose oxidase. *Proc. Natl. Acad. Sci. U.S.A* **2007,** *104*, 6992-6997.

22. Semenov, S. N.; Markvoort, A. J.; de Greef, T. F. A.; Huck, W. T. S., Threshold sensing through a synthetic enzymatic reaction–diffusion network. *Angew. Chem. Int. Ed.* **2014,** *53*, 8066-8069.

23. Yang, K., Dynamic binary protein adsorption in ion-exchange media depicted with a parallel diffusion model derived from Maxwell–Stefan theory. *Chem. Eng. Sci.* **2016,** *139*, 163-172.

24. Tao, Y.; Chen, N.; Carta, G.; Ferreira, G.; Robbins, D., Modeling multicomponent adsorption of monoclonal antibody charge variants in cation exchange columns. *AlChE J.* **2012,** *58*, 2503-2511.

25. Castagnolo, D.; Vergara, A.; Paduano, L.; Sartorio, R.; Annunziata, O., Analysis of the influence of coupled diffusion on transport in protein crystal growth for different gravity levels. *Acta Crystallogr. Sect. D. Biol. Crystallogr.* **2002,** *58*, 1633-1637.

26. Wesselingh, J. A.; Krishna, R., *Mass transfer in multicomponent mixtures*. VSSD: 2006.

27. Cussler, E. L., *Diffusion: Mass transfer in fluid systems*. Cambridge University Press: Cambridge, 1997.

28. Crank, J., *The mathematics of diffusion*. Oxford University Press: Oxford, 1975.

29. Anderson, J. L., Colloid Transport by Interfacial Forces. *Annu. Rev. Fluid Mech.* **1989,** *21*, 61-99.

30. Mehrer, H., *Diffusion in solids: Fundamentals, methods, materials, diffusion-controlled processes*. Springer Berlin Heidelberg: 2007.

31. Cussler, E. L.; Cussler, E. L., *Diffusion: Mass transfer in fluid systems*. Cambridge University Press: 1997.

32. Crank, J.; Crank, E. P. J., *The mathematics of diffusion*. Clarendon Press: 1979.

33. Gitlin, I.; Carbeck, J. D.; Whitesides, G. M., Why are proteins charged? Networks of charge–charge interactions in proteins measured by charge ladders and capillary electrophoresis. *Angew. Chem. Int. Ed.* **2006,** *45*, 3022-3060.

34. Jungwirth, P.; Cremer, P. S., Beyond hofmeister. *Nat. Chem* **2014,** *6*, 261.

35. Leaist, D. G., The role of supporting electrolytes in protein diffusion. *J. Phys. Chem.* **1989,** *93*, 474-479.

36. Annunziata, O.; Buzatu, D.; Albright, J. G., Protein diffusiophoresis and salt osmotic diffusion in aqueous solutions. *J. Phys. Chem. B* **2012,** *116*, 12694-12705.

37. Tyrrell, H. J. V.; Harris, K. R., *Diffusion in liquids: A theoretical and experimental study*. Elsevier Science: 2013.

38. Prieve, D. C., Migration of a colloidal particle in a gradient of electrolyte concentration. *Adv. Colloid Interface Sci.* **1982,** *16*, 321-335.

39. Prieve, D. C.; Roman, R., Diffusiophoresis of a rigid sphere through a viscous electrolyte solution. *J. Chem. Soc., Faraday Trans.* **1987,** *83*, 1287-1306.

40. Shin, S.; Shardt, O.; Warren, P. B.; Stone, H. A., Membraneless water filtration using CO_2. *Nat. Commun.* **2017,** *8*, 15181.

41. McAfee, M. S.; Zhang, H.; Annunziata, O., Amplification of salt-induced polymer diffusiophoresis by increasing salting-out strength. *Langmuir* **2014,** *30*, 12210-12219.

42. Abécassis, B.; Cottin-Bizonne, C.; Ybert, C.; Ajdari, A.; Bocquet, L., Boosting migration of large particles by solute contrasts. *Nat. Mater* **2008,** *7*, 785.

43. Velegol, D.; Garg, A.; Guha, R.; Kar, A.; Kumar, M., Origins of concentration gradients for diffusiophoresis. *Soft Matter* **2016,** *12*, 4686-4703.

44. Altemose, A.; Sánchez-Farrán, M. A.; Duan, W.; Schulz, S.; Borhan, A.; Crespi, V. H.; Sen, A., Chemically controlled spatiotemporal oscillations of colloidal assemblies. *Angew. Chem. Int. Ed.* **2017,** *56*, 7817-7821.

45. Möller, F. M.; Kriegel, F.; Kieß, M.; Sojo, V.; Braun, D., Steep pH gradients and directed colloid transport in a microfluidic alkaline hydrothermal pore. *Angew. Chem. Int. Ed.* **2017,** *56*, 2340-2344.

46. Zwanikken, J. W., Steering colloidal particles over millimeter distances with soluto-inertial beacons. *Proc. Natl. Acad. Sci. U.S.A* **2016,** *113*, 8565-8567.

47. Shin, S.; Um, E.; Sabass, B.; Ault, J. T.; Rahimi, M.; Warren, P. B.; Stone, H. A., Size-dependent control of colloid transport via solute gradients in dead-end channels. *Proc. Natl. Acad. Sci. U.S.A* **2016,** *113*, 257-261.

48. McAfee, M. S.; Annunziata, O., Effect of particle size on salt-induced diffusiophoresis compared to brownian mobility. *Langmuir* **2014,** *30*, 4916-4923.

49. Gosting, L. J., Measurement and interpretation of diffusion coefficients of proteins. *Adv. Protein Chem.* **1956,** *11*, 429-554.

50. Robinson, R. A.; Stokes, R. H., *Electrolyte solutions: Second revised edition*. Dover Publications: 2002.

51. Annunziata, O.; Paduano, L.; Albright, J. G., The effect of salt stoichiometry on protein−salt interactions determined by ternary diffusion in aqueous solutions. *J. Phys. Chem. B* **2006,** *110*, 16139-16147.

52. Grigsby, J. J.; Blanch, H. W.; Prausnitz, J. M., Diffusivities of lysozyme in aqueous $MgCl_2$ solutions from dynamic light-scattering data: Effect of protein and salt concentrations. *J. Phys. Chem. B* **2000,** *104*, 3645-3650.

53. Arakawa, T.; Bhat, R.; Timasheff, S. N., Preferential interactions determine protein solubility in three-component solutions: the magnesium chloride system. *Biochemistry* **1990,** *29*, 1914-1923.

54. Lobo, V. M. M.; Quaresma, J. L., *Handbook of electrolyte solutions. B.* 1989; Vol. 41.

55. Miller, D. G., Application of irreversible thermodynamics to electrolyte solutions. I. Determination of ionic transport coefficients lij for isothermal vector transport processes in binary electrolyte systems. *J. Phys. Chem.* **1966,** *70*, 2639-2659.

56. Miller, D. G.; Rard, J. A.; Eppstein, L. B.; Albright, J. G., Mutual diffusion coefficients and ionic transport coefficients lij of magnesium chloride-water at 25.degree.C. *J. Phys. Chem.* **1984,** *88*, 5739-5748.

57. Shin, Y.; Brangwynne, C. P., Liquid phase condensation in cell physiology and disease. *Science* **2017,** *357*, eaaf4382.

58. Monterroso, B.; Zorrilla, S.; Sobrinos-Sanguino, M.; Keating, C. D.; Rivas, G., Microenvironments created by liquid-liquid phase transition control the dynamic distribution of bacterial division FtsZ protein. *Sci. Rep.* **2016,** *6*, 35140.

59. Ambadipudi, S.; Biernat, J.; Riedel, D.; Mandelkow, E.; Zweckstetter, M., Liquid–liquid phase separation of the microtubule-binding repeats of the Alzheimer-related protein Tau. *Nat. Commun.* **2017,** *8*, 275.

60. Annunziata, O.; Ogun, O.; Benedek, G. B., Observation of liquid–liquid phase separation for eye lens γS-crystallin. *Proc. Natl. Acad. Sci. U.S.A* **2003,** *100*, 970-974.

61. Wang, Y.; Lomakin, A.; Latypov, R. F.; Laubach, J. P.; Hideshima, T.; Richardson, P. G.; Munshi, N. C.; Anderson, K. C.; Benedek, G. B., Phase transitions in human IgG solutions. *J. Chem. Phys.* **2013,** *139*, 121904.

62. Raut, A. S.; Kalonia, D. S., Pharmaceutical perspective on opalescence and liquid–liquid phase separation in protein solutions. *Mol. Pharm.* **2016,** *13*, 1431-1444.

63. Sheldon, R. A.; van Pelt, S., Enzyme immobilisation in biocatalysis: Why, what and how. *Chem. Soc. Rev.* **2013,** *42*, 6223-6235.

64. Annunziata, O.; Pande, A.; Pande, J.; Ogun, O.; Lubsen, N. H.; Benedek, G. B., Oligomerization and phase transitions in aqueous solutions of native and truncated human βB1-crystallin. *Biochemistry* **2005,** *44*, 1316-1328.

65. Galkin, O.; Vekilov, P. G., Control of protein crystal nucleation around the metastable liquid–liquid phase boundary. *Proc. Natl. Acad. Sci. U.S.A* **2000,** *97*, 6277-6281.

66. Taratuta, V. G.; Holschbach, A.; Thurston, G. M.; Blankschtein, D.; Benedek, G. B., Liquid-liquid phase separation of aqueous lysozyme solutions: Effects of pH and salt identity. *J. Phys. Chem.* **1990,** *94*, 2140-2144.

67. Boeynaems, S.; Alberti, S.; Fawzi, N. L.; Mittag, T.; Polymenidou, M.; Rousseau, F.; Schymkowitz, J.; Shorter, J.; Wolozin, B.; Van Den Bosch, L.; Tompa, P.; Fuxreiter, M., Protein phase separation: A new phase in cell biology. *Trends Cell Biol.* **2018,** *28*, 420-435.

68. Hyman, A. A.; Weber, C. A.; Jülicher, F., Liquid-liquid phase separation in biology. *Annu. Rev. Cell Dev. Biol.* **2014,** *30*, 39-58.

69. Mitrea, D. M.; Kriwacki, R. W., Phase separation in biology; functional organization of a higher order. *Cell Commun. Signal.* **2016,** *14*, 1.

70. Alberti, S., Phase separation in biology. *Curr. Biol.* **2017,** *27*, 1097-1102.

71. Tang, L., Liquid phase separation. *Nat. Methods* **2019,** *16*, 18-18.

72. Cable, J.; Brangwynne, C.; Seydoux, G.; Cowburn, D.; Pappu, R. V.; Castañeda, C. A.; Berchowitz, L. E.; Chen, Z.; Jonikas, M.; Dernburg, A.; Mittag, T.; Fawzi, N. L., Phase separation in biology and disease—a symposium report. *Ann. N.Y. Acad. Sci.* **2019,** *1452*, 3-11.

73. Larson, A. G.; Elnatan, D.; Keenen, M. M.; Trnka, M. J.; Johnston, J. B.; Burlingame, A. L.; Agard, D. A.; Redding, S.; Narlikar, G. J., Liquid droplet formation by HP1α suggests a role for phase separation in heterochromatin. *Nature* **2017,** *547*, 236.

74. Strom, A. R.; Emelyanov, A. V.; Mir, M.; Fyodorov, D. V.; Darzacq, X.; Karpen, G. H., Phase separation drives heterochromatin domain formation. *Nature* **2017,** *547*, 241.

75. Wang, Y.; Annunziata, O., Liquid−liquid phase transition of protein aqueous solutions isothermally induced by protein cross-linking. *Langmuir* **2008,** *24*, 2799-2807.

76. Allen, J. P., *Biophysical Chemistry*. Wiley: 2009.

77. Steinhardt, J.; Reynolds, J. A.; Horecker, B.; Kaplan, N. O.; Marmur, J., *Multiple Equilibria in Proteins*. Elsevier Science: 2014.

78. Callewaert, L.; Michiels, C. W., Lysozymes in the animal kingdom. *J. Biosci.* **2010,** *35*, 127-160.

79. Manchenko, G. P., *Handbook of detection of enzymes on electrophoretic gels*. CRC Press: 2002.

80. Ragland, S. A.; Criss, A. K., From bacterial killing to immune modulation: Recent insights into the functions of lysozyme. *PLoS Pathog* **2017,** *13*, e1006512.

81. Singh, R. S.; Singh, T.; Singh, A. K., Enzymes as diagnostic tools. In *Advances in enzyme technology*, Singh, R. S.; Singhania, R. R.; Pandey, A.; Larroche, C., Eds. Elsevier: 2019; pp 225-271.

82. Kuhara, S.; Ezaki, E.; Fukamizo, T.; Hayashi, K., Estimation of the free energy change of substrate binding in lysozyme-catalyzed reactions 1. *J. Biochem.* **1982,** *92*, 121-127.

83. Fukamizo, T.; Minematsu, T.; Yanase, Y.; Hayashi, K.; Goto, S., Substrate size dependence of lysozyme-catalyzed reaction. *Arch. Biochem. Biophys.* **1986,** *250*, 312-321.

84. Muschol, M.; Rosenberger, F., Liquid–liquid phase separation in supersaturated lysozyme solutions and associated precipitate formation/crystallization. *J. Chem. Phys.* **1997,** *107*, 1953-1962.

85. Tanaka, S.; Ataka, M.; Ito, K., Pattern formation and coarsening during metastable phase separation in lysozyme solutions. *Phys. Rev. E* **2002,** *65*, 051804.

86. Lu, J.; Carpenter, K.; Li, R.-J.; Wang, X.-J.; Ching, C.-B., Cloud-point temperature and liquid–liquid phase separation of supersaturated lysozyme solution. *Biophys. Chem.* **2004,** *109*, 105-112.

87. Albright, J. G.; Annunziata, O.; Miller, D. G.; Paduano, L.; Pearlstein, A. J., Precision measurements of binary and multicomponent diffusion coefficients in protein solutions relevant to crystal growth: Lysozyme chloride in water and aqueous NaCl at pH 4.5 and 25 °C. *J. Am. Chem. Soc.* **1999,** *121*, 3256-3266.

88. Zhang, Y.; Cremer, P. S., The inverse and direct Hofmeister series for lysozyme. *Proc. Natl. Acad. Sci. U.S.A* **2009,** *106*, 15249-15253.

89. Chandirasekar, S.; You, J.-G.; Xue, J.-H.; Tseng, W.-L., Synthesis of gold nanocluster-loaded lysozyme nanoparticles for label-free ratiometric fluorescent pH sensing: Applications to enzyme–substrate systems and cellular imaging. *J. Mater. Chem. B* **2019,** *7*, 3876-3883.

90. Wei, H.; Wang, Z.; Zhang, J.; House, S.; Gao, Y.-G.; Yang, L.; Robinson, H.; Tan, L. H.; Xing, H.; Hou, C.; Robertson, I. M.; Zuo, J.-M.; Lu, Y., Time-dependent, protein-directed growth of gold nanoparticles within a single crystal of lysozyme. *Nat. Nanotechnol.* **2011,** *6*, 93-97.

91. Vahdati, M.; Tohidi Moghadam, T., Synthesis and characterization of selenium nanoparticles-lysozyme nanohybrid system with synergistic antibacterial properties. *Sci. Rep.* **2020,** *10*, 510.

92. Cai, H.; Yao, P., In situ preparation of gold nanoparticle-loaded lysozyme–dextran nanogels and applications for cell imaging and drug delivery. *Nanoscale* **2013,** *5*, 2892-2900.

93. Kim, H. J.; Zhang, K.; Moore, L.; Ho, D., Diamond nanogel-embedded contact lenses mediate lysozyme-dependent therapeutic release. *ACS Nano* **2014,** *8*, 2998-3005.

94. Sonu, V. K.; Islam, M. M.; Rohman, M. A.; Mitra, S., Lysozyme binding ability toward psychoactive stimulant drugs: Modulatory effect of colloidal metal nanoparticles. *Colloids Surf. B* **2016,** *146*, 514-22.

95. Anfinsen, C. B.; Edsall, J. T.; Richards, F. M., *Advances in Protein Chemistry*. Academic Press: 1991.

96. Venkataramani, S.; Truntzer, J.; Coleman, D. R., Thermal stability of high concentration lysozyme across varying pH: A Fourier Transform Infrared study. *J Pharm Bioallied Sci* **2013,** *5*, 148-153.

97. Wetter, L. R.; Cohn, M.; Deutsch, H. F., Immunological studies of egg white proteins. *J. Immunol.* **1952,** *69*, 109.

98. Wang, J.; Dauter, M.; Alkire, R.; Joachimiak, A.; Dauter, Z., Triclinic lysozyme at 0.65 A resolution. *Acta Crystallogr. Sect. D. Biol. Crystallogr.* **2007,** *63*, 1254-1268.

99. Wetzel, R.; Perry, L. J.; Baase, W. A.; Becktel, W. J., Disulfide bonds and thermal stability in T4 lysozyme. *Proc. Natl. Acad. Sci. U.S.A* **1988,** *85*, 401-405.

100. Kabsch, W.; Sander, C., Dictionary of protein secondary structure: Pattern recognition of hydrogen-bonded and geometrical features. *Biopolymers* **1983,** *22*, 2577-2637.

101. Kuehner, D. E.; Engmann, J.; Fergg, F.; Wernick, M.; Blanch, H. W.; Prausnitz, J. M., Lysozyme net charge and ion binding in concentrated aqueous electrolyte solutions. *J. Phys. Chem. B* **1999,** *103*, 1368-1374.

102. Kuramitsu, S.; Hamaguchi, K., Analysis of the acid-base titration curve of hen lysozyme. *J. Biochem.* **1980,** *87*, 1215-1219.

103. Tanford, C.; Wagner, M. L., Hydrogen ion equilibria of lysozyme. *J. Am. Chem. Soc.* **1954,** *76*, 3331-3336.

104. Tanford, C.; Roxby, R., Interpretation of protein titration curves. Application to lysozyme. *Biochemistry* **1972,** *11*, 2192-2198.

105. Tanford, C., Multiple equlibria. In *Physical chemistry of macromolecules*, John Wiley & Sons: 1961; pp 526-587.

106. Tanford, C., The interpretation of hydrogen ion titration curves of proteins. *Adv. Protein Chem.* **1963,** *17*, 69-165.

107. Shih, Y.-C.; Prausnitz, J. M.; Blanch, H. W., Some characteristics of protein precipitation by salts. *Biotechnol. Bioeng.* **1992,** *40*, 1155-1164.

108. Arakawa, T.; Timasheff, S. N., The stabilization of proteins by osmolytes. *Biophys. J.* **1985,** *47*, 411-414.

109. Hare, P. D.; Cress, W. A.; Van Staden, J., Dissecting the roles of osmolyte accumulation during stress. *Plant Cell Environ.* **1998,** *21*, 535-553.

110. Taha, M.; Lee, M.-J., Interactions of TRIS [tris(hydroxymethyl)aminomethane] and related buffers with peptide backbone: Thermodynamic characterization. *Phys. Chem. Chem. Phys.* **2010,** *12*, 12840-12850.

111. Han, Q.; Li, J.; Li, J., pH dependence, substrate specificity and inhibition of human kynurenine aminotransferase. *Eur. J. Biochem.* **2004,** *271*, 4804-4814.

112. Pavlič, M., The inhibitory effect of tris on the activity of cholinesterases. *Biochimica et Biophysica Acta (BBA) - Enzymology* **1967,** *139*, 133-137.

113. Desmarais, W. T.; Bienvenue, D. L.; Bzymek, K. P.; Holz, R. C.; Petsko, G. A.; Ringe, D., The 1.20 A resolution crystal structure of the aminopeptidase from aeromonas proteolytica complexed with Tris: A tale of buffer inhibition. *Structure* **2002,** *10*, 1063-1072.

114. Bansal, M. P., *Molecular biology and biotechnology: Basic experimental protocols*. Energy and Resources Institute: 2013.

115. Freifelder, D., *Physical biochemistry: Applications to biochemistry and molecular biology*. W. H. Freeman: 1982.

116. Good, N. E.; Izawa, S., [3] Hydrogen ion buffers. *Methods Enzymol.* **1972,** *24*, 53-68.

117. Taha, M.; e Silva, F. A.; Quental, M. V.; Ventura, S. P. M.; Freire, M. G.; Coutinho, J. A. P., Good's buffers as a basis for developing self-buffering and biocompatible ionic liquids for biological research. *Green Chem.* **2014,** *16*, 3149-3159.

118. Kärger, J.; Ruthven, D. M.; Theodorou, D. N., *Diffusion in nanoporous materials*. Wiley: 2012.

119. Dill, K.; Bromberg, S., *Molecular driving forces: Statistical thermodynamics in biology, chemistry, physics, and nanoscience*. CRC Press: 2012.

120. Krishna, R.; Wesselingh, J. A., The Maxwell-Stefan approach to mass transfer. *Chem. Eng. Sci.* **1997,** *52*, 861-911.

121. Einstein, A., On the movement of small particles suspended in stationary liquids required by the molecularkinetic theory of heat. *Ann. d. Phys* **1905,** *17*, 1.

122. Stokes, G. G., On the effect of the internal friction of fluids on the motion of pendulums. *Trans. Cambridge Philos. Soc.* **1851,** *9*, 8.

123. Stokes, G. G., On the effect of the internal friction of fluids on the motion of pendulums. *Trans. Cambridge Philos. Soc.* **1850,** *9*, 8.

124. Fick, A., Ueber diffusion. *Ann. Phys. (Berl.)* **1855,** *170*, 59-86.

125. Kirkwood, J. G.; Baldwin, R. L.; Dunlop, P. J.; Gosting, L. J.; Kegeles, G., Flow equations and frames of reference for isothermal diffusion in liquids. *J. Chem. Phys.* **1960,** *33*, 1505-1513.

126. Dufrêche, J.-F.; Jardat, M.; Olynyk, T.; Bernard, O.; Turq, P., Mutual diffusion coefficient of charged particles in the solvent-fixed frame of reference from Brownian dynamics simulation. *J. Chem. Phys.* **2002,** *117*, 3804-3810.

127. Zhang, H.; Annunziata, O., Macromolecular hydration compared with preferential hydration and their role on macromolecule-osmolyte coupled diffusion. *Phys. Chem. Chem. Phys.* **2009,** *11*, 8923-8932.

128. Dunlop, P. J.; Gosting, L. J., Use of diffusion and thermodynamic data to test the Onsager reciprocal relation for isothermal diffusion in the system NaCl–KCl–H_2O at 25°. *J. Phys. Chem.* **1959,** *63*, 86-93.

129. Miller, D. G., Some comments on multicomponent diffusion: negative main term diffusion coefficients, second law constraints, solvent choices, and reference frame transformations. *J. Phys. Chem.* **1986,** *90*, 1509-1519.

130. Miller, D. G., Application of irreversible thermodynamics to electiolyte solutions. II. Ionic coefficients for isothermal vector transport processes in ternary systems. *J. Phys. Chem.* **1967,** *71*, 616-632.

131. Kops-Werkhoven, M. M.; Vrij, A.; Lekkerkerker, H. N. W., On the relation between diffusion, sedimentation, and friction. *J. Chem. Phys.* **1983,** *78*, 2760-2763.

132. Yoshida, N., Remarks on the mutual diffusion coefficient of Brownian particles. *J. Chem. Phys.* **1985,** *83*, 1307-1310.

133. Assael, M. J.; Vesovic, V.; Goodwin, A. R. H.; Wakeham, W. A., *Advances in transport properties of fluids*. Royal Society of Chemistry: 2014.

134. Soto, R., *Kinetic theory and transport phenomena*. Oxford University Press: 2016.

135. Fahim, A.; Annunziata, O., Amplification of salt-induced protein diffusiophoresis by varying salt from potassium to sodium to magnesium chloride in water. *Langmuir* **2020,** *36*, 2635-2643.

136. Lechlitner, L. R.; Annunziata, O., Macromolecule diffusiophoresis induced by concentration gradients of aqueous osmolytes. *Langmuir* **2018,** *34*, 9525-9531.

137. Annunziata, O.; Buzatu, D.; Albright, J. G., Protein diffusion coefficients determined by macroscopic-gradient Rayleigh interferometry and dynamic light scattering. *Langmuir* **2005,** *21*, 12085-12089.

138. Sophianopoulos, A. J.; Rhodes, C. K.; Holcomb, D. N.; Van Holde, K. E., Physical studies of lysozyme: I. Characterization. *J. Biol. Chem.* **1962,** *237*, 1107-1112.

139. Rechberger, A.; Amsüss, R.; Rossegger, S.; Breidler, R.; Steiner, G., High precision vibration-type densitometers based on pulsed excitation measurements. *Sensors (Basel)* **2019,** *19*, 1627.

140. Wenger, A. P., Vibrating fluid densimeters: A solution to the viscosity problem. *IEEE Trans. Ind. Electron.* **1980,** *IECI-27*, 247-253.

141. Pitzer, K. S., *Activity coefficients in electrolyte solutions*. 2nd ed.; CRC-Press: 1991.

142. Annunziata, O.; Paduano, L.; Pearlstein, A. J.; Miller, D. G.; Albright, J. G., The effect of salt on protein chemical potential determined by ternary diffusion in aqueous solutions. *J. Phys. Chem. B* **2006,** *110*, 1405-1415.

143. Zhang; Han, Viscosity and density of water + sodium chloride + potassium chloride solutions at 298.15 K. *J. Chem. Eng. Data* **1996,** *41*, 516-520.

144. Isono, T., Density, viscosity, and electrolytic conductivity of concentrated aqueous electrolyte solutions at several temperatures. Alkaline-earth chlorides, lanthanum chloride, sodium chloride, sodium nitrate, sodium bromide, potassium nitrate, potassium bromide, and cadmium nitrate. *J. Chem. Eng. Data* **1984,** *29*, 45-52.

145. Cremer, P.; Jungwirth, P., Beyond Hofmeister. *Nat. Chem* **2014,** *6*, 261-263.

146. Robinson, R. A.; Stokes, R. H., *Electrolyte solutions*. Courier Corporation: 2002.

147. Sengupta, S.; Ibele, M. E.; Sen, A., Fantastic voyage: designing self-powered nanorobots. *Angew. Chem. Int. Ed.* **2012,** *51*, 8434-8445.

148. Ries-Kautt, M.; Ducruix, A. F., Relative effectiveness of various ions on the solubility and crystal growth of lysozyme. *J. Biol. Chem.* **1989,** *264*, 745-748.

149. Sengupta, S.; Ibele, M. E.; Sen, A., Fantastic voyage: Designing self-powered nanorobots. *Angew. Chem. Int. Ed.* **2012,** *51*, 8434-8445.

150. Cussler, E. L.; Cussler, E. L., *Diffusion: Mass transfer in fluid systems*. Cambridge University Press: 2009.

151. Russel, W. B.; Saville, D. A.; Schowalter, W. R., *Colloidal dispersions*. Cambridge University Press: Cambridge, 1989.

152. Henry, D. C.; Lapworth, A., The cataphoresis of suspended particles. Part I. The equation of cataphoresis. *P. Roy. Soc. A - Math Phy.* **1931,** *133*, 106-129.

153. Keh, H. J.; Wei, Y. K., Diffusiophoretic mobility of spherical particles at low potential and arbitrary double-layer thickness. *Langmuir* **2000,** *16*, 5289-5294.

154. Lee, E., *Theory of electrophoresis and diffusiophoresis of highly charged colloidal particles*. Elsevier Science: 2018.

155. Crowe, C. D.; Keating, C. D., Liquid-liquid phase separation in artificial cells. *Interface Focus* **2018,** *8*, 20180032.

156. Mason, B. D.; Zhang-van Enk, J.; Zhang, L.; Remmele, R. L., Jr.; Zhang, J., Liquid-liquid phase separation of a monoclonal antibody and nonmonotonic influence of Hofmeister anions. *Biophys. J.* **2010,** *99*, 3792-3800.

157. Anderson, V. J.; Lekkerkerker, H. N. W., Insights into phase transition kinetics from colloid science. *Nature* **2002,** *416*, 811-815.

158. Cinar, H.; Fetahaj, Z.; Cinar, S.; Vernon, R. M.; Chan, H. S.; Winter, R. H. A., Temperature, hydrostatic pressure, and osmolyte effects on liquid–liquid phase separation in protein condensates: physical chemistry and biological implications. *Chem. Eur. J.* **2019,** *25*, 13049-13069.

159. Anderson, V. J.; Lekkerkerker, H. N., Insights into phase transition kinetics from colloid science. *Nature* **2002,** *416*, 811-815.

160. Falahati, H.; Haji-Akbari, A., Thermodynamically driven assemblies and liquid–liquid phase separations in biology. *Soft Matter* **2019,** *15*, 1135-1154.

161. Astier, J.-P.; Veesler, S., Using temperature to crystallize proteins: A mini-review. *Cryst. Growth Des.* **2008,** *8*, 4215-4219.

162. Kashchiev, D.; Vekilov, P. G.; Kolomeisky, A. B., Kinetics of two-step nucleation of crystals. *J. Chem. Phys.* **2005,** *122*, 244706.

163. Wolde, P. R. t.; Frenkel, D., Enhancement of protein crystal nucleation by critical density fluctuations. *Science* **1997,** *277*, 1975-1978.

164. Talanquer, V.; Oxtoby, D. W., Crystal nucleation in the presence of a metastable critical point. *J. Chem. Phys.* **1998,** *109*, 223-227.

165. Nicolis, G.; Nicolis, C., Enhancement of the nucleation of protein crystals by the presence of an intermediate phase: a kinetic model. *Physica A* **2003,** *323*, 139-154.

166. Lutsko, J. F., Communication: A dynamical theory of homogeneous nucleation for colloids and macromolecules. *J. Chem. Phys.* **2011,** *135*, 161101.

167. Pan, W.; Kolomeisky, A. B.; Vekilov, P. G., Nucleation of ordered solid phases of proteins via a disordered high-density state: phenomenological approach. *J. Chem. Phys.* **2005,** *122*, 174905.

168. Galkin, O.; Chen, K.; Nagel, R. L.; Hirsch, R. E.; Vekilov, P. G., Liquid–liquid separation in solutions of normal and sickle cell hemoglobin. *Proc. Natl. Acad. Sci. U.S.A* **2002,** *99*, 8479-8483.

169. Kalikmanov, V. I., *Nucleation theory*. Springer Netherland, 2012.

170. Karthika, S.; Radhakrishnan, T. K.; Kalaichelvi, P., A review of classical and nonclassical nucleation theories. *Cryst. Growth Des.* **2016,** *16*, 6663-6681.

171. Sear, R. P., Nucleation: theory and applications to protein solutions and colloidal suspensions. *J. Phys.: Condens. Matter* **2007,** *19*, 033101.

172. Gunton, J. D.; Shiryayev, A.; Pagan, D. L., *Protein condensation: Kinetic pathways to crystallization and disease*. Cambridge University Press: 2007.

173. Annunziata, O., On the role of solute solvation and excluded-volume interactions in coupled diffusion. *J. Phys. Chem. B* **2008,** *112*, 11968-11975.

174. Zhou, H.-X.; Nguemaha, V.; Mazarakos, K.; Qin, S., Why do disordered and structured proteins behave differently in phase separation? *Trends Biochem. Sci.* **2018,** *43*, 499-516.

175. Levine, I., *Physical chemistry*. McGraw-Hill Higher Education: 2008.

176. Lomakin, A.; Asherie, N.; Benedek, G. B., Monte Carlo study of phase separation in aqueous protein solutions. *J. Chem. Phys.* **1996,** *104*, 1646-1656.

177. Guin, D.; Gruebele, M., Weak chemical interactions that drive protein evolution: Crowding, sticking, and quinary structure in folding and function. *Chem. Rev.* **2019,** *119*, 10691-10717.

178. Roth, R.; Evans, R.; Louis, A. A., Theory of asymmetric nonadditive binary hard-sphere mixtures. *Phys. Rev. E* **2001,** *64*, 051202.

179. Dijkstra, M.; van Roij, R.; Evans, R., Phase diagram of highly asymmetric binary hard-sphere mixtures. *Phys. Rev. E* **1999,** *59*, 5744-5771.

180. Banani, S. F.; Lee, H. O.; Hyman, A. A.; Rosen, M. K., Biomolecular condensates: organizers of cellular biochemistry. *Nat. Rev. Mol.* **2017,** *18*, 285-298.

181. Gögelein, C., *Phase behaviour of proteins and colloid polymer mixtures*. Forschungszentrum, Zentralbibliothek: 2008.

182. Wolf, M.; Roosen-Runge, F.; Zhang, F.; Roth, R.; Skoda, M. W. A.; Jacobs, R. M. J.; Sztucki, M.; Schreiber, F., Effective interactions in protein–salt solutions approaching liquid–liquid phase separation. *J. Mol. Liq.* **2014,** *200*, 20-27.

183. Wills, P. R.; Winzor, D. J., van der Waals phase transition in protein solutions. *Acta Crystallogr. Sect. D. Biol. Crystallogr.* **2005,** *61*, 832-836.

184. Mason, E. A.; Spurling, T. H., *The Virial equation of state*. Elsevier Science & Technology: 1969.

185. Wei, M.-T.; Elbaum-Garfinkle, S.; Holehouse, A. S.; Chen, C. C.-H.; Feric, M.; Arnold, C. B.; Priestley, R. D.; Pappu, R. V.; Brangwynne, C. P., Phase behaviour of disordered proteins underlying low density and high permeability of liquid organelles. *Nat. Chem* **2017,** *9*, 1118-1125.

186. Neal, B. L.; Lenhoff, A. M., Excluded volume contribution to the osmotic second virial coefficient for proteins. *AlChE J.* **1995,** *41*, 1010-1014.

187. Wentzel, N.; Gunton, J. D., Liquid−liquid coexistence surface for lysozyme: Role of salt type and salt concentration. *J. Phys. Chem. B* **2007,** *111*, 1478-1481.

188. Asherie, N.; Lomakin, A.; Benedek, G. B., Phase diagram of colloidal solutions. *Phys. Rev. Lett.* **1996,** *77*, 4832-4835.

189. Vliegenthart, G. A.; Lekkerkerker, H. N. W., Predicting the gas–liquid critical point from the second virial coefficient. *J. Chem. Phys.* **2000,** *112*, 5364-5369.

190. Petsev, D. N.; Wu, X.; Galkin, O.; Vekilov, P. G., Thermodynamic functions of concentrated protein solutions from phase equilibria. *J. Phys. Chem. B* **2003,** *107*, 3921-3926.

191. Berry, J.; Brangwynne, C. P.; Haataja, M., Physical principles of intracellular organization via active and passive phase transitions. *Rep. Prog. Phys.* **2018,** *81*, 046601.

192. Nakashima, K. K.; Vibhute, M. A.; Spruijt, E., Biomolecular chemistry in liquid phase separated compartments. *Front. Mol. Biosci.* **2019,** *6*, 21.

193. Rubinstein, M.; Colby, R. H., *Polymer physics*. Oxford University Press: Oxfords, 2003.

194. Prinsen, P.; Odijk, T., Optimized Baxter model of protein solutions: Electrostatics versus adhesion. *J. Chem. Phys.* **2004,** *121*, 6525-6537.

195. Platten, F.; Hansen, J.; Wagner, D.; Egelhaaf, S. U., Second Virial coefficient As determined from protein phase behavior. *J. Phys. Chem. Lett.* **2016,** *7*, 4008-4014.

196. Muschol, M.; Rosenberger, F., Interactions in undersaturated and supersaturated lysozyme solutions: Static and dynamic light scattering results. *J. Chem. Phys.* **1995,** *103*, 10424-10432.

197. Gögelein, C.; Wagner, D.; Cardinaux, F.; Nägele, G.; Egelhaaf, S. U., Effect of glycerol and dimethyl sulfoxide on the phase behavior of lysozyme: Theory and experiments. *J. Chem. Phys.* **2012,** *136*, 015102.

198. Platten, F.; Valadez-Pérez, N. E.; Castañeda-Priego, R.; Egelhaaf, S. U., Extended law of corresponding states for protein solutions. *J. Chem. Phys.* **2015,** *142*, 174905.

199. Leckband, D.; Israelachvili, J., Intermolecular forces in biology. *Q. Rev. Biophys* **2001,** *34*, 105-267.

200. Lima, E. R. A.; Biscaia Jr., E. C.; Boström, M.; Tavares, F. W., Ion-specific thermodynamical properties of aqueous proteins. *An. Acad. Bras. Ciênc.* **2010,** *82*, 109-126.

201. Poon, W. C. K.; Egelhaaf, S. U.; Beales, P. A.; Salonen, A.; Sawyer, L., Protein crystallization: scaling of charge and salt concentration in lysozyme solutions. *J. Phys.: Condens. Matter* **2000,** *12*, L569-L574.

202. Sedgwick, H.; Cameron, J. E.; Poon, W. C. K.; Egelhaaf, S. U., Protein phase behavior and crystallization: Effect of glycerol. *J. Chem. Phys.* **2007,** *127*, 125102.

203. Wang, Y.; Annunziata, O., Comparison between protein−polyethylene glycol (PEG) interactions and the effect of PEG on protein−protein interactions using the liquid−liquid phase transition. *J. Phys. Chem. B* **2007,** *111*, 1222-1230.

204. Berne, B. J.; Pecora, R., *Dynamic light scattering: With applications to chemistry, biology, and physics*. Dover Publications: 2013.

205. Pecora, R., *Dynamic light scattering: Applications of photon correlation spectroscopy*. Springer US: 2013.

206. Stetefeld, J.; McKenna, S. A.; Patel, T. R., Dynamic light scattering: a practical guide and applications in biomedical sciences. *Biophys Rev* **2016,** *8*, 409-427.

207. Subramanian, M.; Sheshadri, B. S.; Venkatappa, M. P., Interaction of lysozyme with Dyes. II. Binding of Bromophenol blue. *J Biochem* **1984,** *96*, 245-52.

208. da Costa, V. C. P.; Hwang, B. J.; Eggen, S. E.; Wallace, M. J.; Annunziata, O., Formation and thermodynamic stability of (polymer+porphyrin) supramolecular structures in aqueous solutions. *J. Chem. Thermodyn.* **2014,** *75*, 119-127.

209. Zaccai, N. R.; Serdyuk, I. N.; Zaccai, J., *Methods in molecular biophysics: Structure, dynamics, function for biology and medicine*. Cambridge University Press: 2017.

210. Ladbury, J. E.; Doyle, M. L., *Biocalorimetry 2: Applications of calorimetry in the biological sciences*. Wiley: 2005.

211. Holde, K. E. v., *Physical biochemistry*. 2nd ed.; Prentice-Hall: Englewood Cliffs, NJ, 1985.

212. Scatchard, G., The attractions of proteins for mmall molecules and ions. *Ann. N.Y. Acad. Sci.* **1949,** *51*, 660-672.

213. Freire, E.; Mayorga, O. L.; Straume, M., Isothermal titration calorimetry. *Anal. Chem.* **1990,** *62*, 950A-959A.

214. Lee, D. B.; Kim, J.-M.; Seok, J. H.; Lee, J.-H.; Jo, J. D.; Mun, J. Y.; Conrad, C.; Coe, J.; Nelson, G.; Hogue, B.; White, T. A.; Zatsepin, N.; Weierstall, U.; Barty, A.; Chapman, H.; Fromme, P.; Spence, J.; Chung, M. S.; Oh, C.-H.; Kim, K. H., Supersaturation-controlled microcrystallization and visualization analysis for serial femtosecond crystallography. *Sci. Rep.* **2018,** *8*, 2541.

215. Schuster, B. S.; Reed, E. H.; Parthasarathy, R.; Jahnke, C. N.; Caldwell, R. M.; Bermudez, J. G.; Ramage, H.; Good, M. C.; Hammer, D. A., Controllable protein phase separation and modular recruitment to form responsive membraneless organelles. *Nat. Commun.* **2018,** *9*, 2985.

216. Kanaan, N. M.; Hamel, C.; Grabinski, T.; Combs, B., Liquid-liquid phase separation induces pathogenic tau conformations in vitro. *Nat. Commun.* **2020,** *11*, 2809.

217. Pande, A.; Mokhor, N.; Pande, J., Deamidation of human γS-crystallin increases attractive protein interactions: Implications for cataract. *Biochemistry* **2015,** *54*, 4890-4899.

218. Kastelic, M.; Kalyuzhnyi, Y. V.; Hribar-Lee, B.; Dill, K. A.; Vlachy, V., Protein aggregation in salt solutions. *Proc. Natl. Acad. Sci. U.S.A* **2015,** *112*, 6766-6770.

219. Chen, X.; Yang, T.; Kataoka, S.; Cremer, P. S., Specific ion effects on interfacial water structure near macromolecules. *J. Am. Chem. Soc.* **2007,** *129*, 12272-12279.

220. Guilloteau, J.-P.; Rie`s-Kautt, M. M.; Ducruix, A. F., Variation of lysozyme solubility as a function of temperature in the presence of organic and inorganic salts. *J. Cryst. Growth* **1992,** *122*, 223-230.

221. Annunziata, O.; Asherie, N.; Lomakin, A.; Pande, J.; Ogun, O.; Benedek, G. B., Effect of polyethylene glycol on the liquid–liquid phase transition in aqueous protein solutions. *Proc. Natl. Acad. Sci. U.S.A* **2002,** *99*, 14165-14170.

222. Bloustine, J.; Virmani, T.; Thurston, G. M.; Fraden, S., Light scattering and phase behavior of lysozyme-poly(ethylene glycol) mixtures. *Phys. Rev. Lett.* **2006,** *96*, 087803.

223. Knubovets, T.; Osterhout, J. J.; Connolly, P. J.; Klibanov, A. M., Structure, thermostability, and conformational flexibility of hen egg-white lysozyme dissolved in glycerol. *Proc. Natl. Acad. Sci. U.S.A* **1999,** *96*, 1262-1267.

224. Asherie, N., Protein crystallization and phase diagrams. *Methods* **2004,** *34*, 266-72.

225. Yamazaki, T.; Kimura, Y.; Vekilov, P. G.; Furukawa, E.; Shirai, M.; Matsumoto, H.; Van Driessche, A. E. S.; Tsukamoto, K., Two types of amorphous protein particles facilitate crystal nucleation. *Proc. Natl. Acad. Sci. U.S.A* **2017,** *114*, 2154-2159.

226. Aldabaibeh, N.; Jones, M. J.; Myerson, A. S.; Ulrich, J., The solubility of orthorhombic lysozyme crystals obtained at high pH. *Cryst. Growth Des.* **2009,** *9*, 3313-3317.

227. Yu, X.; Ulrich, J.; Wang, J., Crystallization and stability of different protein crystal modifications: A case study of lysozyme. *Cryst. Res. Technol.* **2015,** *50*, 179-187.

228. Ewing, F.; Forsythe, E.; Pusey, M., Orthorhombic lysozyme solubility. *Acta Crystallogr. Sect. D. Biol. Crystallogr.* **1994,** *50*, 424-428.

229. Monaco, L. A.; Rosenberger, F., Growth and etching kinetics of tetragonal lysozyme. *J. Cryst. Growth* **1993,** *129*, 465-484.

230. McPherson, A., *Crystallization of biological macromolecules*. Cold Spring Harbor Laboratory Press: 1999.

231. Vekilov, P. G., Phase diagrams and kinetics of phase transitions in protein solutions. *J. Phys.: Condens. Matter* **2012,** *24*, 193101.

232. Fine, B. M.; Lomakin, A.; Ogun, O. O.; Benedek, G. B., Static structure factor and collective diffusion of globular proteins in concentrated aqueous solution. *J. Chem. Phys.* **1996,** *104*, 326-335.

233. Arakawa, T.; Timasheff, S. N., Preferential interactions of proteins with salts in concentrated solutions. *Biochemistry* **1982,** *21*, 6545-6552.

234. Baranauskiene, L.; Kuo, T. C.; Chen, W. Y.; Matulis, D., Isothermal titration calorimetry for characterization of recombinant proteins. *Curr. Opin. Biotechnol.* **2019,** *55*, 9-15.

235. Bettelheim, F. A.; Brown, W. H.; Campbell, M. K.; Farrell, S. O., *Introduction to general, organic and biochemistry*. Cengage Learning: 2009.

236. Stoll, V. S.; Blanchard, J. S., [4] Buffers: Principles and practice. *Methods Enzymol.* **1990,** *182*, 24-38.

237. Hansen, S. H.; Andersen, M. L.; Cornett, C.; Gradinaru, R.; Grunnet, N., A role for taurine in mitochondrial function. *J. Biomed. Sci.* **2010,** *17*, S23.

238. Caster, K. C., Ethanolamine. In *Encyclopedia of reagents for organic synthesis*, Caster, K. C., Ed. John Wiley & Sons: 2001.

239. Khalili, F.; Henni, A.; East, A. L. L., p*K*a values of some piperazines at (298, 303, 313, and 323) K. *J. Chem. Eng. Data* **2009,** *54*, 2914-2917.

240. Ghosh, S.; Pandey, N. K.; Sen, S.; Tripathy, D. R.; Dasgupta, S., Binding of hen egg white lysozyme fibrils with nucleic acids. *J. Photochem. Photobiol. B, Biol.* **2013,** *127*, 52-60.

241. Padlan, C. S.; Malashkevich, V. N.; Almo, S. C.; Levy, M.; Brenowitz, M.; Girvin, M. E., An RNA aptamer possessing a novel monovalent cation-mediated fold inhibits lysozyme catalysis by inhibiting the binding of long natural substrates. *RNA* **2014,** *20*, 447-461.

242. Lin, K. C.; Wey, M. T.; Kan, L. S.; Shiuan, D., Characterization of the interactions of lysozyme with DNA by surface plasmon resonance and circular dichroism spectroscopy. *Appl. Biochem. Biotechnol.* **2009,** *158*, 631-41.

243. Abey, S. K.; Yuana, Y.; Joseph, P. V.; Kenea, N. D.; Fourie, N. H.; Sherwin, L. B.; Gonye, G. E.; Smyser, P. A.; Stempinski, E. S.; Boulineaux, C. M.; Weaver, K. R.; Bleck, C. K. E.; Henderson, W. A., Lysozyme association with circulating RNA, extracellular vesicles, and chronic stress. *BBA Clinical* **2017,** *7*, 23-35.

244. De Boeck, S.; Stockx, J., Mode of interaction between lysozyme and the other proteins of the hen's egg vitelline membrane. *Int. J. Biochem.* **1986,** *18*, 623-8.

245. Kato, A.; Miyoshi, Y.; Suga, M.; Kobayashi, K., Separation and characterization of sulfated glycopeptides from ovomucin, chalazae and yolk membrane in chicken eggs. *Agr. Bio.l Chem.* **1982,** *46*, 1285-1290.

246. Ciolkowski, M.; Pałecz, B.; Appelhans, D.; Voit, B.; Klajnert, B.; Bryszewska, M., The influence of maltose modified poly(propylene imine) dendrimers on hen egg white lysozyme structure and thermal stability. *Colloids Surf. B* **2012,** *95*, 103-108.

247. Sekar, G.; Florance, I.; Sivakumar, A.; Mukherjee, A.; Chandrasekaran, N., Role of PAMAM-OH dendrimers against the fibrillation pathway of biomolecules. *Int. J. Biol. Macromol.* **2016,** *93*, 1007-1018.

248. Wang, B.; Sun, Y.; Davis, T. P.; Ke, P. C.; Wu, Y.; Ding, F., Understanding effects of PAMAM dendrimer size and surface chemistry on serum protein binding with discrete molecular dynamics simulations. *ACS Sustain. Chem. Eng.* **2018,** *6*, 11704-11715.

249. Ralston, G. B., Effects of "crowding" in protein solutions. *J. Chem. Educ.* **1990,** *67*, 857-860.

VITA

Personal Background	Aisha Fahim Bahawalpur, 63100, Punjab, Pakistan
Education	M.Sc. Chemistry The Islamia University of Bahawalpur, Pakistan, 2009 M.Phil. Physical Chemistry The Islamia University of Bahawalpur, Pakistan, 2011
Teaching Experience	Teaching Assistantship Texas Christian University, Fort Worth, 2016-2020 Lecturership Govt. Sadiq College Women University, Pakistan, 2015-2016 Lecturership The Islamia University of Bahawalpur, Pakistan, 2010-2011
Oral and Poster Presentations	Oral Presentation 51st ACS Meeting-in-miniature, April 21, 2018, Dallas, TX. Poster Presentation SRS, April 12, 2019, Texas Christian University, Fort Worth, TX. Poster Presentation SRS, April 20, 2018, Texas Christian University, Fort Worth, TX.
Selected Publications	Fahim, A.; Annunziata, O., *Int. J. Heat Mass Transfer* 2020, *163*, 120436. Fahim, A.; Annunziata, O., *Langmuir* 2020, *36* (10), 2635-2643. Mehmood, A.; Fahim, A.; Ahmed, M.; Noureen, S., *J. Mol. Struct* 2020, *1216* (4), 128483. Mehmood, A.; Bano, S.; Fahim, A.; Parveen, R.; Khurshid, S., *Korean J. Chem. Eng.* 2015, *32* (5), 882-895.

ABSTRACT

ROLE OF COSOLUTES ON LYSOZYME DIFFUSIOPHORESIS AND CONDENSATION IN AQUEOUS MIXTURES

by Aisha Fahim, Ph.D., 2020
Department of Chemistry & Biochemistry
Texas Christian University

Dissertation Advisor: Onofrio Annunziata, Professor of Chemistry

Lysozyme is a model protein in physicochemical studies. This dissertation investigates two properties of lysozyme aqueous mixtures: salt-induced protein diffusiophoresis and liquid-liquid phase separation (LLPS).

Diffusiophoresis is the migration of a particle induced by cosolute concentration gradients. This not-well-understood transport property is important for applications in separation science and microfluidics. In the dissertation first part, lysozyme diffusiophoresis induced by salt gradients was examined as a function of salt concentration at pH 4.5 and 25 °C for NaCl, KCl and $MgCl_2$. Diffusiophoresis coefficients were extracted from multicomponent-diffusion data by applying non-equilibrium thermodynamics. A selected mass-transfer process was theoretically examined to show that $MgCl_2$ concentration gradients produce significant lysozyme diffusiophoresis. Diffusiophoresis dependence on salt nature was theoretically examined and linked to protein charge. The effect of salt type on hydrogen-ion titration curves was characterized to understand role of salt on protein charge. Our findings indicate that $MgCl_2$-induced protein diffusiophoresis can be exploited in protein separation science and adsorption-based biosensing.

LLPS of protein aqueous mixtures is the reversible formation of protein-rich micro-droplets occurring below a well-defined temperature. This phase transition is metastable with respect to protein crystallization and aggregation. LLPS is important for protein crystallization and development of protein-based materials. It is also believed to be implicated in cell compartmentalization and protein-aggregation diseases. Lysozyme aqueous solutions reversibly undergo LLPS around 0 °C in the presence of additives such as NaCl near physiological composition. In the dissertation second part, it is shown that insertion of 4-(2-hydroxyethyl)-1-piperazineethanesulfonate (HEPES) as a second additive to lysozyme-NaCl-water mixtures reproducibly triggers conversion of protein-rich droplets into protein microparticles displaying crystalline nature. LLPS studies were extended to other additives sharing chemical similarities with HEPES. In these cases, droplets conversion into microparticles was either absent or drastically reduced. The phase diagram of the lysozyme-HEPES system was characterized. Measurements of lysozyme diffusion, HEPES supernatant concentration and heat of mixing show that lysozyme-HEPES interactions are weakly attractive and exothermic. Our findings indicate that additives with weak protein-ligand properties represent an important tool for controlling the fate of metastable protein-rich micro-droplets. This may be exploited in the preparation of protein-based materials and femtosecond crystallography.